Fakultät für Luft- und Raumfahrttechnik

Characterization of a turbulent separating/ reattaching flow using optical pressure and velocity measurements

Dipl.-Ing. Martin B i t t e r

Vollständiger Abdruck der von der Fakultät für Luft- und Raumfahrttechnik der Universität der Bundeswehr München zur Erlangung des akademischen Grades eines

Doktor-Ingenieur (Dr.-Ing.)

genehmigte Dissertation.

Vorsitzender: Prof. Dr.-Ing. Reinhard Niehuis

1. Gutachter: Prof. Dr. rer. nat. habil. Christian J. Kähler

2. Gutachter: Prof. Keisuke Asai (PhD)

Die Dissertation wurde am 11.04.2013 bei der Universität der Bundeswehr München eingereicht und durch die Fakultät für Luft- und Raumfahrttechnik am 17.04.2013 angenommen. Die mündliche Prüfung fand am 26.09.2013 statt.

Acknowledgment

First of all, my special thanks go to Prof. Christian Kähler who accompanied my personal development since 2005. I'd like to thank him for taking over the guidance and mentoring of all the different projects during my time at the department and for being the host of this dissertation. It has been great learning from your experience!

I'd also like to thank Prof. Reinhard Niehuis for taking over the chair of my graduation procedure and certainly Prof. Keisuke Asai as one of the world-wide leading experts on the Pressure-Sensitive Paint technique for the support from his department especially during the experimental Summer School 2012 and finally for taking over the job as one of the reviewers of my dissertation.

Furthermore, I'd like to thank the DFG - Deutsche Forschungsgemeinschaft - that funded the generic space-craft project within the framework of Transregio 40 and to the people from the PSP work-group of the DLR in Göttingen (Dr. Christian Klein et al.) who strongly supported the progress of the PSP technique at LRT7 with their long-lasting experience.

Additionally, I thank all the remaining scientific, technical and assisting members of LRT7 who always supported my work and kept all systems running.

My remarkable thanks go to my colleague Rainer Hain for intensive and enormously helpful discussions on various topics, methods and approaches until the late night and also to my colleague Sven Scharnowski for the cooperation within the DFG project and augmentative discussions on turbulent wakes.

Last but definitely not least, I want to thank for the support from my home front. My wife Jeica, my parents and my brother always showed interest and patience or had some words of encouragement not only during this thesis work, but especially in the partly difficult years before.

Dipl.-Ing. Martin Bitter

Neubiberg, January 2014

Kurzfassung

Die turbulente Nachlaufströmung hinter einem generischen Raketenmodell wurde bei Machzahlen $M_\infty = [0.3; 0.7]$ im trisonischen Windkanal München experimentell untersucht. Es sollten die Wechselwirkungen zwischen der Strömung und der Struktur im Heckbereich qualifiziert werden, welche unter realen Flugbedingungen in der Vergangenheit zeitweise zu sicherheitskritischen Interaktionen am realen Flugkörper gesorgt haben.
Die Charakterisierung des dynamischen Verhaltens von kohärenten Strömungsstrukturen erfolgte mit Hilfe zeitaufgelöster optischer und klassischer Messmethoden. Die Topologie des Geschwindigkeitsfeldes wurde mit der 2C2D-PIV untersucht. Das dynamische Verhalten der Druckschwankungen wurde mit der instationären PSP-Messtechnik eingehend analysiert. Aus den Ergebnissen konnten sowohl die Lage der Wiederanlegeposition als auch die örtliche Dynamik starker, groß-skaliger Strömungsstrukturen abgeleitet werden. Es ließen sich erwartete charakteristische Frequenzen von $f_{\text{shed}} \approx [400; 900]$ Hz nachweisen. Es konnte erstmals experimentell mit hoher örtlicher und zeitlicher Auflösung nachgewiesen werden, wie sich das charakteristische Verhalten der Strömung/Struktur-Wechelwirkung im Nachlauf entwickelt und wo die Position der stärksten Belastungen im Heckbereich auftreten.
Zur Durchführung der Experimente wurde ein PSP Messsystem etabliert. Hierfür wurden einzelne Komponenten (bspw. Kalibrierkammer, Beleuchtung, Softwarepaket zur Datenanalyse) entwickelt und die Performance des Gesamtsystems in verschiedenen Geschwindigkeitsbereichen validiert.

Abstract

The turbulent wake flow behind a generic spacecraft was investigated experimentally in the trisonic wind tunnel Munich at subsonic Mach numbers $M_\infty = [0.3; 0.7]$.
The flow/structure interaction which raised critical safety aspects on the real spacecraft in the past was studied. The characterization of the coherent flow structures was performed by means of transient optical and classical measurement techniques. The topology and dynamics of the wake flow and the pressure field were investigated with the 2C2D-PIV and the instationary PSP. The reattachment position as well as the local dynamic behavior of strong flow structures were successfully characterized and the presence of dominant vortex shedding at expected frequencies around $f_{\text{shed}} \approx [400; 900]$ Hz was confirmed. It was the first time that the fluid/structure interaction and the position of strongest stresses could be characterized experimentally with very high spatial and temporal resolution.
A PSP system had to be established in order to perform the desired experiments. Therefore, basic components (e.g. calibration chamber, excitation, evaluation tool) had to be developed and the performance of the entire system had to be validated.

Contents

1. Introduction

1.1. Motivation

The outer space fascinates mankind from the very beginning. The identification of the origin of all live on earth is still one of the driving forces why people are interested in the universe. Modern inventions continuously helped us reaching a high-technology state on earth and even in outer space. Satellites are one of the leading inventions which improved our daily lives. Their networks ensure the world-wide sharing of informations.
Reusable space transportation systems, such as the American Space Shuttle or the European Ariane, were and still are the ultimate vehicles that are able to place such technical equipment in the low-earth orbits. These transportation systems offer high demands on safety aspects and efficiency. After the discontinuation of the Space Shuttle program, the European Ariane family is required even more frequently. Figure 1.1 shows a schematic of an *Ariane V* space transportation system as it is produced by an European joint venture, ESA/CNES/Arianespace (2013). These spacecrafts are exposed to strong mechanical and thermal loads during their launch and their flight within the earth's atmosphere. The *Ariane V* spacecraft, for example, is

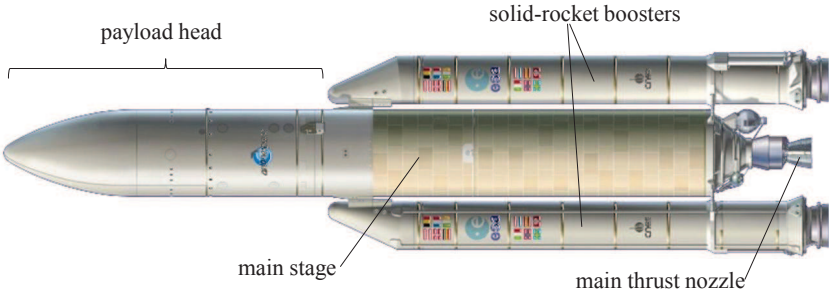

Fig. 1.1.: Overview of the European *Ariane V* space transportation system and its major components (figure provided by ESA/CNES/Arianespace (2013)).

accelerated from 0 to 2000 m/s by two auxiliary solid-rocket boosters and one main thrust nozzle within the first 2 minutes after take-off. A controlled and safe handling of all thermally abused structures, such as the cryogenic tanks where liquid nitrogen is stored or the exhaust and thrust nozzles, is mandatory for safe space missions. The extreme acceleration causes high structural stresses. They are mainly caused by vibrations and strong fluid-dynamic loads. All these operational demands require high precautions in terms of reliability and design of the spacecraft. A system failure usually has dramatic consequences because these vehicles are still often manned. A structural failure led to the discontinuation of the American Space Shuttle in 2003.
Some critical structural aspects that were investigated by Schrijer et al. (2011) came up during the major tests of the *Vulcain 2* main thrust nozzle of an *Ariane V*. Fluid/structure interactions induced vibrations and deformations into the mechanical structure of the nozzle. The strong unsteady fluctuations caused defects in the cooling system and enforced a structural re-design. These aspects resulted in a delayed operational launch of the main engine at that time. The fluid-dynamic loads on the structure are highest during take-off and while the space vehicle passes the sonic barrier (known as transonic conditions).
Two comprehensive research programs, such as the *Future European Space Transportation Investigations Program* (FESTIP), and its successor, the project of *Key Technologies for Reusable Space Systems* (RESPACE) were established in the past by the European spacecraft manufacturers in order to ensure a continuous improvement of their actual systems, see Pfeffer (1996) and Gülhan (2008). A large number of experiments with individual interests were performed within these two projects. Investigations by Henckels et al. (2007) examined the effect of the exhaust plume on the pressure and density of the flow field in the afterbody domain for supersonic Mach numbers up to 11.2. Experiments carried out by van Oudheusden and Scarano (2008) analyzed the velocity flow field separating from the base as well as the interactions of the free flow with the exhaust plume at flow Mach number 3 by means of the particle image velocimetry. Herrin and Dutton (1994) performed pressure and laser-doppler velocimetry measurements up to Mach = 2.5 in order to characterize the wake flow field and to evaluate the shear stresses which are produced by the unsteady wake vortices. David and Radulovic (2005) carried out wind tunnel and in-flight measurements in order to examine the loads on the nozzle and the afterbody caused by the pressure fluctuations in the unsteady shear layer.
All these experiments were performed in order to understand the flow physics during a spacecraft flight envelop and to identify potential fluid-dynamic problems. On the other hand, the data was used to validate numerical flow simulations. The progress of modern numerical methods significantly facilitated and accelerated the design process of recent spacecrafts within the last years. Reynolds-Averaged Navier-Stokes simulations (RANS) are well established to estimate the mean flow field and predict the average payload of spacecrafts, see Lüdeke et al. (2006). As unsteady effects play a dominant

role, more sophisticated methods like large-eddy simulations (LES) or detached-eddy simulations (DES) are increasingly applied to characterize the flow dynamics and provide detailed informations of the entire flow field, see Deck et al. (2007). The dynamic loads from transient simulations might help to optimize the structural weight, for example, in order to increase the payload weight. As a drawback, the simulations are only as precise as their models and assumptions. A reliable turbulence modeling is essential for the precise prediction of dynamic structural loads as a consequence from fluid/structure interactions. Various turbulence models were established for steady and unsteady simulations over the last decades. The flow conditions during a spacecraft flight envelope and the raising demands in terms of safety and efficiency require better turbulence models for more precise load predictions. These requirements in turn necessitate an increasing amount of high quality experimental data in order to validate the models and predictions.
Recent ongoing experimental and numerical research is extended in the framework of the project *Technological foundations for the design of thermally and mechanically highly loaded components of future space transportation systems* that is founded by the *Deutsche Forschungsgemeinschaft* (DFG), see SFB/TR 40 (2013). It specifically concentrates on prospective concepts for thermally and structurally highly loaded components, such as the combustion chamber, the nozzle cooling or the afterbody structure. The *Institute of Fluid Mechanics and Aerodynamics* of the *Bundeswehr University Munich* (UniBwM), as one of the project partners, is notably interested in the experimental characterization of the wake flow and its interactions with the afterbody structure under transonic test conditions by means of transient optical pressure and velocity field measurement techniques.

1.2. Scientific background

From the fluid-mechanical point of view it is essential to study the individual effects separately, not as a consequence of potential interactions from a fairly complex geometry. Hence, a generic model of an *Ariane V* main stage was derived from the original geometry as it is displayed in the lower part of Figure 1.2. The dimensions of the main stage afterbody were scaled by either $1:50$ or $1:100$ by the experimentalists. The length of the generic configuration was from minor interest. It mainly served for the generation of realistic boundary layer profiles. Under real-flight conditions, a turbulent boundary layer is present at this stage which had to generated by the cylindrical part of the configuration, too.
This generic spacecraft configuration represents the extensively studied axisymmetric backward-facing step (BFS). The topological characteristic of this test case is a flow separation from the shoulder of the step and the reattachment of the shear layer to the

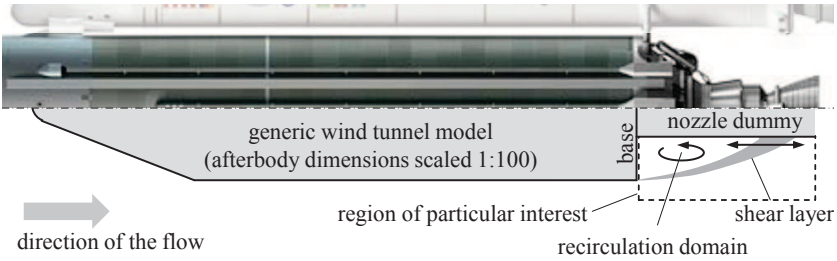

Fig. 1.2.: Close-up of an *Ariane V* mid- and afterbody (figure partially provided by ESA/CNES/Arianespace (2013)) compared with the derived generic wind tunnel model of the main stage. The dimensions of the afterbody were scaled 1 : 100. The particular region of interest for this thesis (*dashed box*) as well as the primary scientific goals are highlighted.

geometry as indicated in Fig. 1.2. A distinct recirculation vortex system establishes between the separation and the reattachment point. Coherent structures with a large dynamic range in size and strength organize in a shear layer between the outer and the recirculation flow. This shear layer is characterized by distinct properties, such as characteristic flapping frequencies or the position of the reattachment.
Eaton (1980) summarized the basic historical research on various two-dimensional and axisymmetric BFS configurations. The authors examined the strong dependence of the wake topology on properties like flow Reynolds number, free-stream turbulence, boundary-layer state or step height. These factors complicate the comparison of individual experimental and numerical BFS results. A careful differentiation and classification of the specific test case is necessary for a reliable comparison of individual data.
The authors in Lee and Sung (2001), Hudy et al. (2003) and Hudy et al. (2007) characterized the wake of a BFS at low-Reynolds number conditions by means of transient microphone and optical velocity field measurements. They applied the two-point signal correlation for the identification of coherent pattern convection rates and classified a characteristic distribution of the pressure fluctuation in the wake with a fairly good spatial resolution. The authors in Deprés et al. (2004) performed experimental investigations on a transonic axisymmetric separating/reattaching flow at Reynolds numbers around 1 million. They were interested primarily in the behavior of coherent pressure modes in the near-wake region. They used classic transient but point-wise pressure measurement techniques for the characterization of the shear layer dynamics. These data was compared to transient numerical simulations performed by Deck et al. (2007) and

Weiss et al. (2009). The numerical simulations resolved the flow topology with high spatial resolution. As a drawback, the duration of the transient simulation in terms of an adequate number of data sampling points was too short for an adequate analysis of characteristic dynamics in the flow. Hence, conclusions about significant characteristic flow frequencies were impeded by the brevity of the available time signal.

1.3. Scientific goal and methods

The fundamental scientific questions addressed in this thesis are:

1. How is the topology of the wake flow?
2. How is the dynamic and the strength of the coherent wake structures in the shear layer?
3. Are these structures characterized by a certain frequency?
4. Does the boundary layer/ wake interaction result in a coherent mode pattern on the base?
5. Is this mode pattern somehow time-dependent?

In addition, the generation of a high quality data base for the validation of numerical models was an essential concern. The quality of the data strongly depended on the applied measurement techniques as indicated by the experiments that were conducted in the past. Due to this reason, optical pressure and velocity measurement methods such as the pressure-sensitive paint (PSP) and the particle image velocimetry (PIV) measurement techniques were applied. The major advantage of these optical methods is the absence of measurement probes which potentially influence the flow and bias the quality of the experimental data. In addition, these techniques can offer a combination of high spatial and temporal resolutions that can be hardly reached by conventional methods, such as pressure transducers or hot-wire probes.
Since the PIV measurement technique is already established and extensively used all over the world, the pressure-sensitive paint measurement technique is only rarely applied. PIV systems are widely commercially available whereas PSP systems are seldom sold. However, the biggest advantage of optical pressure measurements with PSP is that a complex equipment of a wind tunnel model with pressure transducers can be renounced. On the other hand, the surface pressure can be measured with a spatial resolution comparable to CFD methods. This motivated the establishment of a PSP measurement system at the department of UniBwM in order to raise the community of users and increase the impact of this technique.

1.4. Structure of this thesis

The optical measurement techniques are presented in Chapter 2. The physical working principles as well as the basic theoretical background of the applied techniques are introduced. The PSP calibration system and the characteristics of the applied PSP coatings are described in detail within this chapter as well.
The PSP measurement technique yet suffers from the comparably low number of users and publications, in comparison to PIV. Comprehensive elementary research on parameters which potentially infect a PSP result is still required. Chapter 3 engages some of the dominant error sources that may effect a PSP result. Known parameters, like the temperature effect, an alternating (unstable) excitation, the self-illumination problem or potential paint contaminations were investigated because they are the most dominant error sources within the wind tunnel facilities from the department. The discussion of the individual parameters should help classifying the measurement uncertainty as a consequence of the specific error sources. Some procedures are presented which may help to reduce the individual effects.
A suitable image-processing routine for the evaluation of PSP data was developed in Chapter 4. The basic constraints for the implementation as well as a validation by means of synthetic images is presented within this chapter.
The validation of the entire PSP system under low- and high-speed conditions is discussed in Chapter 5. Two NACA airfoil test series are presented which reveal the performance of the PSP system under wind tunnel test conditions. A comprehensive assessment of the measurement uncertainty benchmarks the PSP system.
Finally, the results of transient PIV and PSP measurements are intensively discussed in Chapter 6 in order to answer the aroused scientific key questions. Two successive test series are discussed, starting with the characterization of the flow velocity field around the generic spacecraft followed by a detailed analysis of the pressure fluctuation loads in the recirculation domain. Comparisons with numerical simulations and the literature assessed the novelty of the fluid-mechanical results. Special care was taken in the separation of potential sources of individual effects. Ascertained characteristic flow phenomena are widely analyzed by means of redundant independent evaluation approaches.

2. Optical field measurement techniques

2.1. Pressure-sensitive paint (PSP)

2.1.1. History and state of the art

The pressure-sensitive paint measurement technique (PSP) is a luminescence application that was designed for the optical and contactless determination of surface pressure distributions. The measuring principle is based on the detection of luminescence intensities which are emitted by excited luminophors. These luminophors are O_2-sensitive and tend to transfer its excitation energy to surrounding oxygen molecules. If no oxygen molecule is present within a certain lifetime, the excitation energy is released as luminescence intensity. Further photo-chemical background is given in section 2.1.2.
This process was discovered in the early 1940s by Kautsky and Hirsch (1935) as a substitution of conventional methods for detecting lowest oxygen concentrations. Moon et al. (1965) were the first who detected small enthalpy changes by not using established methods but by using luminescence applications. By the early 1990s, American and Soviet scientists independently realized the potential of this method as a tool for experimental fluid mechanics, see Peterson and Fitzgerald (1980) and Pervushin and Nevsky (1981). Initially, this technique was only used for flow visualization. Since then, the development of suitable luminophors was enforced in order to determine surface pressures quantitatively. In the U.S., the University of Washington in cooperation with *Boeing* and the *National Aeronautics Space Administration* (NASA) played a leading role in developing appropriate O_2-sensitive molecules designed as optical pressure sensors, compare Kavandi et al. (1990). At the same time, Soviet laboratories (*Russian Central Aerohydrodynamic Institute* - TsAGI) explored the photo-chemical background of the early PSP measurement technique, see Ardasheva et al. (1982).
From now on, luminophors based on ruthenium, palladium, porphyrin or pyrene complexes were applied as O_2 sensors offering pressure sensitivities of about 70-90 %/ 100 kPa, as reported in Liu and Sullivan (2005) or Stich and Wolfbeis (2008). For their application in aerodynamic testing, the luminophors had to be anchored on the surface of a test body. One of the major demands was that the luminophors have to stick to the surface of the test body and not to being removed by strong shear forces as they occur under transonic test conditions. With the development of an O_2-permeable binder it was possible to apply the luminophors to the model in some kind of paint. This de-

fined the terminology pressure-sensitive “paint”. The early PSPs possessed an unwanted temperature dependence of up to 10 %/ K besides the desired pressure sensitivity, see Mosharov et al. (1997). Up to now, the temperature dependence was minimized down to some per mill per Kelvin by various approaches, as reported in Woodmansee and Dutton (1998); Khalil et al. (2004); Liu and Sullivan (2005).
During the last 20 years, the PSP measurement method became an established technique for aerodynamic testing at the majority of large aeronautical research facilities. In Europe, this technique is applied at the German aerospace center (DLR) since 1991 and at the French aerospace lab (ONERA) since 1997, compare Engler et al. (1991) or Le Sant et al. (1997). Similar to the U.S., a large number of Japanese research institutes worked on the optimization of PSPs. Japanese scientists were initially interested in the use of pressure-sensitive paints at extremely low temperatures and oxygen concentrations (cryo-PSP, Asai et al. (1997; 2001)). These flow conditions require a highly porous binder that allows the interaction of certainly low gas concentrations with the luminophors. From this PSP approach, the development of highly porous PSPs for transient measurements started, see Asai et al. (1997); Abe et al. (2004); Kameda et al. (2005) or Sakaue et al. (2006).
Except for the large research facilities and their partner universities, the potential of PSP in measuring surface pressure distributions is virtually unknown at the worldwide university departments. Nevertheless, the laboratories that have been working on PSP developed a powerful tool for experimental fluid mechanics. Nowadays, PSP can be used in nearly every area of experimental fluid mechanics. Numerous works reaching from μ-PSP applications with high optical magnification over classic low-speed experiments to tests conducted under trans- and supersonic conditions proved this method’s potential. Under design conditions (e.g. transonic flow) and by using advanced imaging systems, absolute accuracies of $\Delta c_p \leq 0.005$ can be achieved. An overview of the individual steps from history to an advanced measurement method and the variety of applications are described in detail in the standard works from Mosharov et al. (1997) and Liu and Sullivan (2005) as well as in review articles from Kavandi et al. (1990); Bell et al. (2001) or Gregory et al. (2008).

2.1.2. Photo-physical background

This section describes the basic physical processes for understanding the PSP measurement method. The derivation of the quantum mechanical background was dispensed at this point. The basics (involving sub-processes, models and boundary conditions) are described in more detail in Parker (1968) or in the PSP standard works. Figure 2.1 schematically reveals the essential mechanisms which help to understand PSP as a luminescence application. The single processes are discussed in more detail in the following. All discussed sub-processes are subject to a certain probability of their oc-

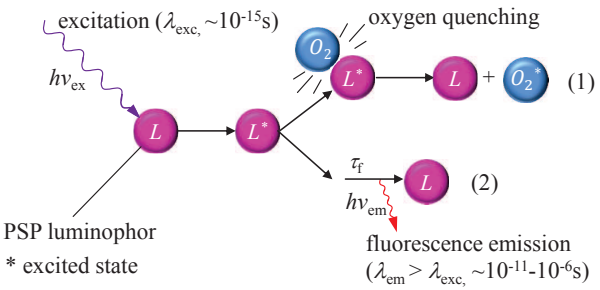

Fig. 2.1.: Basic photo-physical principles of PSP: excitation of a luminophor L by short-wave radiation and its two most probable relaxation methods; (1) relaxation by energy transfer from the luminophor to an oxygen molecule (quenching); (2) relaxation by photon emission.

currence. The individual processes are considered on the basis of a luminophor that definitely participates in the respective process.

Excitation by radiation absorption

The basis for this optical measurement technique is the absorption of electromagnetic waves ($h\nu_{ex}$) and the conversion of this absorbed energy. Luminophors can convert impacting energy coming from a photon. By this, luminophors might transfer to an excited energy state, the so-called singlet or triplet state. The decision whether an excited singlet or a triplet state is headed for is connected to the pair-wise spin orientation. For the singlet state, the spin orientation remains as it was in the ground state. For the triplet state, a reversal of the spin orientation is required. The energy transfer is described by

$$L_{S0} + h\nu_{ex} \xrightarrow{k_{ex}} L^*_{S1}. \tag{2.1.1}$$

L_{S0} and L^*_{S1} represent the excitation from the ground singlet state ($S0$) to an excited singlet state ($S1$ - first excited singlet state) caused by the energy $h\nu_{ex}$. The portion of this energy conversion is characterized by the specific rate k_{ex}. The absorption of light from a luminophor is depending on the intensity of the excitation and is described by the Beer-Lambert law, see Mosharov et al. (1997) or Bell et al. (2001). This process occurs very rapidly with typical absorption time constants of about 10^{-15} s. By excessive excitation (high impact of photons), a luminophor reaches the state of saturation. It can be disabled completely or partially for further chemical processes. This causes irreversible damage to the luminophor. This effect is known as photo-degradation in PSP applications.

Since the excited state is metastable, the luminophor does not rest in this state for a long time. There are several relaxation possibilities to return from the excited state back to the ground state. Originating from the molecular structure of each luminophor, there are preferred and difficult transitions between the different excited states and the ground state. Preferred transitions with high probability are called spin-allowed whereas difficult transitions with low probability are called spin-forbidden, see Flottmann et al. (2004).

Non-radiative relaxation

Non-radiative relaxations describe transitions from the excited to the ground state whereas no photons are emitted. In PSP applications, the luminophors are typically surrounded by a gas. In this gas the molecules of the various components can move freely.
One potential (spin-allowed) relaxation is the shock-induced exchange of energy from the excited luminophor with an appropriate collision partner. An O_2 molecule is the ideal collision partner for a PSP luminophor. The energy exchange between the two collision partners (denoted by the rate k_q) is known as oxygen quenching.

$$L^*_{S1} + O_2 \xrightarrow{k_q} L_{S0} + O^*_2 \tag{2.1.2}$$

The excited luminophor transfers all its excitation energy to the collision partner. The luminophor itself relapses back into its ground state and the collision partner gets excited by the induced energy exchange (path (1) in Fig. 2.1). Hence, all energy is transferred and no photons are emitted. The luminophor and its quenching partner remain physically and photo-chemically intact during this interaction. They may be re-excited.
Another non-radiative relaxation is the conversion from the excitation energy into thermal energy Δ. The energy of the excited luminophor is instantaneously converted during a temperature change. This process is known as thermal quenching. This highly likely relaxation is the reason why most PSP luminophors are highly sensitive to temperature changes beside their desired O_2 sensitivity. On the other hand, there exist many luminophors that have no oxygen but only a temperature sensitivity. These luminophors are practicably applied in the temperature-sensitive paint (TSP) measurement technique for the determination of surface temperature distributions, see Liu and Sullivan (2005).
It might happen that an excited electron changes its state of excitation while it remains excited. Therefore, a inversion of the spin orientation is required (spin-forbidden transition). The transition of the luminophor might occur from the excited singlet to the excited triplet state.

$$L^*_{S1} \xrightarrow{k_{isc}} L_{T1} + \Delta \tag{2.1.3}$$

This is known as energy system crossing (inter-system crossing). If the excitation energy was high enough, the luminophor might be excited from the ground state directly to the second excited singlet state. At this state, the excited energy level cannot be sustained for long and the energy reduces continuously until the electron relapses back to the first excited singlet state.

$$L^*_{S2} \xrightarrow{k_{ic}} L_{S1} + \Delta \tag{2.1.4}$$

This mechanism is called internal conversion. Both, the inter-system crossing and the internal conversion, also convert the excitation energy into heat Δ and do not generate any photons. All the non-radiative processes where heat conversion occurs are combined in the energy conversion rate k_{nr} for further discussions.

Radiative relaxation

If the luminophor has defended its excitation energy for a certain time, a radiative relaxation to the ground state is highly probable, as it is indicated by path (2) in Figure 2.1. These relaxations are commonly referred to as cold light or luminescence. A distinction is made between fluorescence and phosphorescence. Fluorescence is the most likely radiative relaxation.

$$L^*_{S1} \xrightarrow{k_f} L_{S0} + h\nu_{em,f} \tag{2.1.5}$$

The molecule spontaneously and quickly emits the excitation energy in form of photons $h\nu_{em,f}$. The rate k_f symbolizes the energetic portion of the fluorescence. Since the luminophor used some excitation energy for the transition to its excited state, the energy it releases during the relaxation is slightly lower. Hence, it emits radiation with less energy or longer wavelength ($\lambda_{em} > \lambda_{ex}$) according to the Stoke's shift. The time that the excited luminophors stays in its excited state before it relapses back into its ground state is called fluorescence lifetime τ_f. Typical fluorescence decay times are $(10^{-11}$-$12^{-6})$ s.
In the case of an inter combination or an inter-system crossing, the luminophor rests in the excited triplet state. From this state, it might also relapse into its ground state only by emitting photons.

$$L^*_{S1} \xrightarrow{k_{nr}} L_{T1} + \Delta \xrightarrow{k_p} L_{S0} + h\nu_{em,p} \tag{2.1.6}$$

This spin-forbidden process is called phosphorescence that is highly likely quenched by an oxygen molecule. This is because the transition between the excited triplet state of luminophor and the triplet ground state of the oxygen molecule is permitted (spin-allowed). Phosphorescence does not occur spontaneously and has typical decay rates of $(10^{-3}$-$12^{3})$ s. It depends on the luminophore whether fluorescence or phosphorescence is the dominant radiative relaxation. The rates for radiative relaxations are combined into one rate $k_r = k_f + k_p$ in the following.

2.1.3. Model for conventional PSP

A first order model for the rate of change of all excited luminophors was derived in Liu and Sullivan (2005). The combination of all individual energy change rates results in the following model:

$$\frac{d[L^*]}{dt} = I_{\mathrm{ex}} - (k_{\mathrm{r}} + k_{\mathrm{nr}} + k_{\mathrm{q}}[O_2])[L^*]. \tag{2.1.7}$$

The terms in square brackets describe a concentration either of the luminophors $[L^*]$ or the oxygen $[O_2]$. Further, a steady state is assumed where the luminophor concentration does not change ($d[L^*]/dt = 0$). A quantum yield Φ can be defined which relates the the output luminescence with input energy:

$$\Phi = \frac{\text{rate of luminescence}}{\text{rate of excitation}} \tag{2.1.8}$$

The ratio of the quantum yield in absence of a quencher (Φ_0) with respect to the quantum yield in presence of a quencher (Φ) leads to the well-known Stern-Volmer equation which is the basic equation for PSP applications, compare Stern and Volmer (1919):

$$\frac{\Phi_0}{\Phi} = \frac{I_0}{I} = 1 + \frac{k_{\mathrm{q}}}{k_{\mathrm{r}} + k_{\mathrm{nr}}}[O_2] = 1 + k_{\mathrm{q}}\tau_{\mathrm{f},0}[O_2] = \frac{\tau_{\mathrm{f},0}}{\tau_{\mathrm{f}}} \tag{2.1.9}$$

Here, $\tau_{\mathrm{f},0} = 1/(k_{\mathrm{r}} + k_{\mathrm{nr}})$ is the luminescence lifetime in the absence of the quencher and $\tau_{\mathrm{f}} = 1/(k_{\mathrm{r}} + k_{\mathrm{nr}} + k_{\mathrm{q}}[O_2])$ is the lifetime in the presence of a quencher. Thus, Equation 2.1.9 describes the rate of change of luminescence properties of a specific molecule with respect to a change in the concentration of a potential quencher. Some constraints are essential for the application of Equation 2.1.9 in the sense of PSP:

1. All designated energy conversion rates of oxygen-sensitive luminophors are somehow temperature dependent $k_{\mathrm{i}}(T, [O_2])$.
2. The luminophors are typically introduced into a binder for practicable reasons, as mentioned above. Hence, the individual luminophor-specific energy conversion rates $k_{\mathrm{i}}(T, [O_2])$ are further summarized in paint-specific coefficients ($A(T)$, $B(T, [O_2])$, ...) .
3. Since PSP is applied in wind tunnel facilities, a reference state without any quencher (I_0) is impracticable. Thus, a state with no flow is used as a reference state for the formation of the ratio of quantum yields. This state will be denoted as wind-off state in the following. Here, the static pressure is assumed to be constant and precisely known as p_{ref}.
4. The state where the unknown pressure distribution is from interest is further called wind-on state.

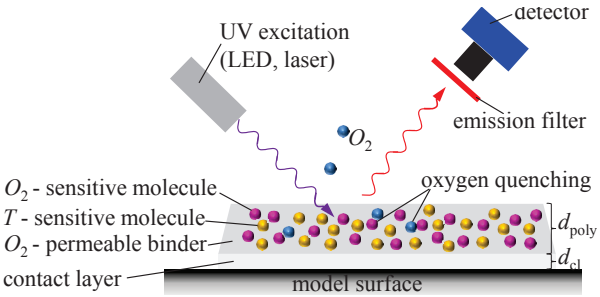

Fig. 2.2.: Schematic of a binary PSP with temperature-dependent reference probe for steady aerodynamic testing.

Up to this point, the introduced approach is still a method for detecting oxygen concentrations. The closure for the problem as an aerodynamic pressure measurement technique is given by Henry's law. It directly links the concentration of a gas in a fluid (here: $[O_2]$ in air) to the partial pressure and hence to the static pressure of the gas in the fluid (here: p_{O_2}) in the fluid:

$$[O_2] = k_H p_{O_2} \tag{2.1.10}$$

where k_H describes the solubility of the gas in the fluid (here: O_2 in air $[O_2] = 0.21\,k_H$). The combination of this closure approach from Equ. 2.1.10 together with the four constraints from above gives the basic equation for PSP applications:

$$\left(\frac{I_{ref}}{I}\right)(T,p) = \left(\frac{\tau_{f,ref}}{\tau_f}\right)(T,p) = A(T) + B(T)\left(\frac{p}{p_{ref}}\right) \tag{2.1.11}$$

This linear form of the Stern-Volmer equation describes the photo-physical behavior of some luminophors very well. However, a higher-order empirical approach, such as:

$$\left(\frac{I_{ref}}{I}\right)(T,p) = A(T) + B(T)\left(\frac{p}{p_{ref}}\right) + C(T)\left(\frac{p}{p_{ref}}\right)^2 \tag{2.1.12}$$

better approximates the intensity signal for a wider variaty of luminophors. The ratio between the wind-on and wind-off luminescence intensities is referred to as Stern-Volmer ratio or I_{ref}/I in the following. The sum of the binder- and luminophor-specific coefficients $A(T), B(T,p), C(T,p)$ is one at $T = T_{ref} = \text{const}$. They must be calibrated for each individual paint composition. The coefficients B can be interpreted as pressure sensitivity of the paint composition (in [%/ kPa]). By knowing the static reference pressure p_{ref} at the wind-off condition and by applying the luminophor-specific coefficients A, B, C to a given intensity ratio I_{ref}/I, the pressure distribution at the wind-on state can be

calculated. This finally requires the inversion of Equ. 2.1.12. Figure 2.2 schematically illustrates the practical implementation for the determination of steady-state pressure distributions. The luminophors are embedded in an oxygen-permeable binder polymer. They are commonly excited by ultraviolet light (e.g. LED, laser, flash lamp). The excited luminophors are exposed to an environment with a certain oxygen concentration that changes between wind-off and wind-on conditions. The excited luminophors which are not deactivated by quenching emit luminescence intensity at a longer wavelength. This intensity distribution is recorded by a detector (e.g. CCD, CMOS, PMT). In order to separate the excitation from the emission signal, optical filters are typically used in front of the detector.
A second luminophor that is pressure-invariant but sensitive to temperature- and excitation intensity was introduced in the binder polymer. It is commonly known as reference monitor. This luminophor compensates local temperature gradients. Additionally, it accounts for potential excitation fluctuations because it is usually excited at the same wavelength as the pressure-sensitive dye. Such PSPs are commonly referred to as binary PSPs because of their two luminophors. PSPs which only contain the pressure-sensitive dye are widely known as uni coatings. Binary paints might be useful for applications where strong surface temperature changes appear at the model (e.g. during transonic testing as a consequence of compressibility effects). The layer thickness of the active PSP layer (d_{poly}) typically varies between 10 and 50 μm in order to conserve the aerodynamic shape of the model and give a reasonable signal-to-noise ratio.
An additional coating was applied prior to the active PSP layer. It is known as contact or screen layer. This coating compensates surface inhomogeneities of the model, improves the adhesion of the active layer on the model and may increase the SNR at the same time. A bright paint with diffuse scattering is typically applied as screen layer because it reflects both, the excitation and the emission signal. The thickness of the contact layer (d_{cl}) should be as low as possible. Typically, 5-10 μm are realistic.
Some commercially available uni and binary coatings (*UF400, BF400*, ISS Inc. (2013)) have been used for the steady-state experiments presented within this thesis. Their emission spectra are shown in Figure 2.3. Porphyrin complexes (Pt(II)meso-tetra-(pentafluorophenyl)porphyrine - PtTFPP) are used as pressure-sensitive luminophors in both coatings. The paints are characterized by a strong model adhesion, a high surface smoothness and a good SNR. Further details on the composition of the binder (e.g. volume percentages) are subject to trade secret of the manufacturer and were not available. The difference between the two paints is clearly notable by the peak occurring at $\lambda \approx 556\,\mathrm{nm}$, reflecting the pressure-invariant reference dye. The peak from $\lambda \approx 650\,\mathrm{nm}$ is dedicated to the PtTFPP luminophors. Its intensity changes with pressure, temperature and excitation intensity. For an increase of the SNR, a screen layer was usually applied underneath all PSP coatings during the experiments. In the following terminology, a red camera acquires the pressure signal and a green camera records the reference signal, as a consequence from the spectral peaks in the emission band.

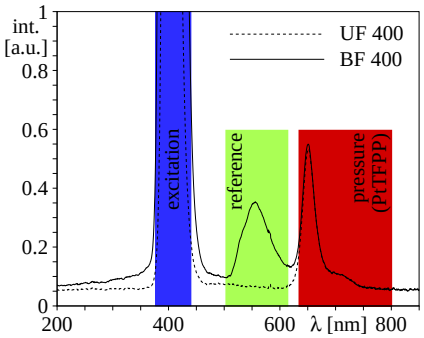

Fig. 2.3.: Emission spectra of PtTFPP based one-component (*dashed*) and two-component PSPs (*solid*), from ISS Inc. (2013).

PSP coatings as they were introduced up to here are known as conventional coatings. They can be used for steady-state measurements only because of the design of their binder polymer. The gas diffusion time, which is a measure for the temporal resolution, describes the time that a quencher molecule needs for its diffusion through the binder to the position of the luminophor:

$$\tau_{\text{diff}} \propto \frac{d_{\text{poly}}^2}{D_{\text{m}}} \tag{2.1.13}$$

It is significantly dependent on the thickness of the binder polymer (d_{poly}) and its gas permeability (D_{m}). Recent developments which enable the performance of PSP as a transient measurement technique are discussed in the following.

2.1.4. Model for unsteady PSP

Reflecting relation 2.1.13, it is obvious that the design and thickness of the binder polymer limits the response time of a PSP. For an increased response time, the layer thickness d_{poly} must be reduced and/or the porosity of the binder D_{m} has to be raised. Reducing the layer thickness usually involves a decrease of the SNR due to a lower luminophor concentration. To counter this effect, a variety of approaches established. The goal still is creating a highly porous structure with a large effective surface where the luminophors can be attached to. The transient PSP technique is referred to as instationary PSP (iPSP - in the following). Figure 2.4 schematically shows the approach of a highly porous iPSP with virtually no binder polymer and hence no diffusion time constant.

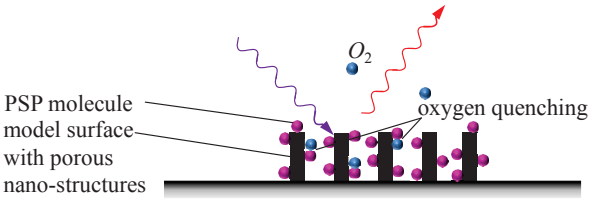

Fig. 2.4.: Schematic of highly porous iPSP surface for unsteady aerodynamic testing.

Baron et al. (1993) demonstrated that this procedure was applicable for increasing the temporal resolution. They produced an emulsion that crystallized during drying and finally had a highly porous structure in which the luminophors were anchored. However, the coating was very sensitive to shear forces and could be easily removed from the test body. Japanese scientists pursued a different iPSP approach that was intentionally designed for PSP measurements under cryogene conditions (cryo-PSP), see Asai et al. (1997; 1998; 2002). In cryogene wind tunnel flows, the fluid consists of nitrogen that is evaporated and cools the fluid down to very low temperatures. In contrast, the oxygen concentration within this fluid drops down to a few ppm (1 ppm = 1 part per million). For a distinct interaction with such small amounts of oxygen, the luminophors must be anchored directly at the surface of the test body in order to enable the quenching process. Their approach was an artificial surface roughening by means of an electrochemical catalytic process (anodization). Hence, this approach is known as AA-PSP (AA - anodized aluminum). Artificial nano-structures are constructed during the catalytic process, similar to the ones in Figure 2.4. These structures are highly hydrophobic and easily absorb liquids by dipping. This is also the major disadvantage because this technique can hardly be applied to test bodies which provide sensitive electronic equipment that might be destroyed through the dipping process. Nevertheless, this technique is widely used due to its good surface quality and its high temporal resolution, compare Mérienne et al. (2004); Kameda et al. (2005); Sakaue et al. (2006) or Singh et al. (2011). Recent results show that AA-PSP allows the resolution of characteristic flow frequencies in high Kilo- or even Megahertz regimes, see Gregory et al. (2007) or Fujii et al. (2013). At such high frequencies, a phase-locked acquisition and sample averaging is required for a sufficient SNR.

The test bodies which were used for the experiments that are presented within the scope of this work were partly equipped with sensitive electronic transducers. From this reason, the use of a highly porous polymer/ceramic binder (pc-PSP) was chosen for iPSP measurements, as it was first presented by Scroggin et al. (1999). The non-toxic binder can be applied to the model surface by a spray gun like a conventional painting. A water-based emulsion is produced from highly porous titanium dioxide particles (TiO_2)

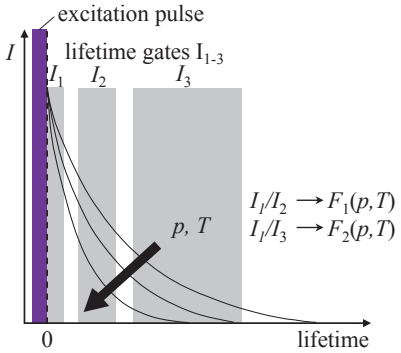

Fig. 2.5.: Fluorescence lifetimes as a function of pressure and temperature. Multiple lifetime gates are the basis for the lifetime PSP method.

which were held together by a stabilizer. The individual binder components crystallize while drying (about 12-24 h, depending on the temperature) and form a sponge-like structure that is resistant to shear forces. The luminophors are directly anchored within this structure. The composition of the binder, arising from Gregory et al. (2008), is as follows: for 1 g of distilled water, 1.72 g of TiO_2 (*DuPont* R-900 TiPure) and 12 mg of a dispersant (*Rohm & Haas* D-3021) were added. This solution was ball-milled for about 1 h. Then, 3.5 vol.% of a polymer emulsion (*Rohm & Haas* B-1000) were added to the ceramic slurry. A layer of about 5 μm was finally applied to the test body. The pressure-sensitive dye was prepared from 1 mg of the PtTFPP luminophors which were dissolved in 5 ml toluene. It was applied to the ceramic base layer by spray gun. The paint properties are discussed later in this chapter.

2.1.5. Radiometric and lifetime PSP

Two basic measurement principles can be derived from Equation 2.1.11. If the luminophors are exposed to short-wave radiation for a certain time ($t_{exp} \gg \tau_f$) the luminescence intensity can be integrated by a conventional imaging system (e.g. CCD, CMOS, s-CMOS) that is equipped with an appropriate optical filter, compare Figure 2.2. The ratio I_{ref}/I of the integrated luminescence intensity from the wind-off and the wind-on conditions is calculated. The integration times are typically ranged from a few milliseconds to some seconds. This principle is usually referred to as radiometric or intensity method. The method is widely used and it is also applied for the experiments presented in this work. The major advantages of the radiometric method is the simplicity of the measurement apparatus and the data reduction as well as a fairly good SNR

that allows the detection of small pressure changes. The averaging of a small number of samples can provide high-quality PSP results. The major disadvantage is that the results are strongly dependent on the stationarity of both, the excitation source as well as luminophor-specific properties (e.g. temperature, concentration, homogeneity).
The second measurement principle originates from the determination of the ratio of the luminescence lifetime τ_f. Therefore, this PSP application is known as lifetime method, compare Davis et al. (1995); Hradil et al. (2002) or Mitsuo et al. (2006). The luminescence lifetime, as a response on an instantaneous excitation pulse, is an exponential decay rate that is variant to pressure and temperature as it is schematically shown in Fig. 2.5. Typically, this exponential decay rate is sampled at two or more points (gates) by means of a fast scanning device, such as a photo-multiplier tube or a multi-gated camera, compare Ruyten (2004). The ratio of the lifetimes from the individual gates is a luminophor-specific measure that changes with pressure and temperature. More than one decay ratio is typically used in order to compensate the temperature effect. The major advantage of a multiple-ratio lifetime approach in comparison with the radiometric PSP method is that the lifetime ratio needs no wind-off reference state. The calculation of two lifetime ratios or more makes this method virtually invariant to temperature changes, to non-uniformities of the excitation intensity and to luminophor properties (e.g. concentration and aging). The major disadvantages are a complex recording system and a fairly low SNR.
Good results from both methods require a high-quality imaging system. The image sensor should have a low noise level, a high dynamic range (14 bit or better) and a high linearity in its response behavior. The imaging optics should have small aberrations and distortions. High efforts are required which ensure a temperature compensation, for example. A detailed analysis of some effects which influence the measurement accuracy of the radiometric method is presented later in Chapter 3. An even more comprehensive accuracy assessment can be found in Liu and Sullivan (2005).
The digital intensity images are analyzed with appropriate image processing tools. A data reduction tool for radiometric PSP images was developed at UniBwM. It will be discussed in more detail in Chapter 4.

2.1.6. Luminescence calibration

The luminescence calibration for the intensity method is closely linked to the terms of an in-situ and an a-priori calibration, according to Liu and Sullivan (2005). In an in-situ calibration, the paint coefficients (A, B, C) are determined directly at the surface of a coated wind tunnel model. This is done while the static pressure inside the test section is varied and the luminescence intensity of the excited coating is captured and directly linked with the pressure information. This procedure accounts for paint layer thickness and/or luminophor concentration inhomogeneity. By this approach, virtually

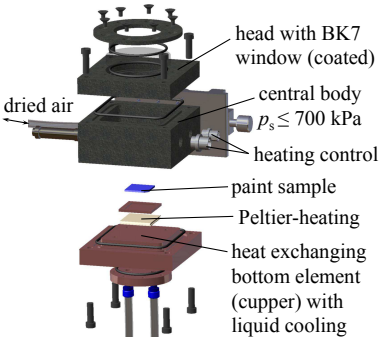

Fig. 2.6.: Component view of the static PSP/TSP calibration chamber.

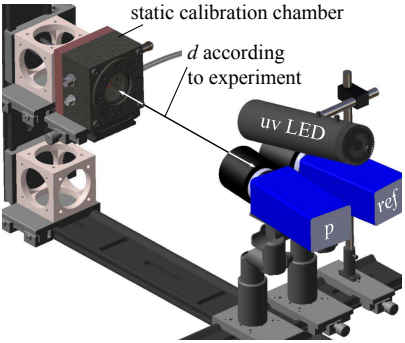

Fig. 2.7.: Static PSP/TSP calibration rig with 2 CCD cameras and uv illumination (LED).

every pixel of the imaging sensor can be calibrated individually. As a drawback, this procedure premises a wind tunnel facility whose test section can be pressurized under steady state conditions.

An a-priori calibration usually means that the paint coefficients are determined from a paint sample in a separate (laboratory) experiment. It is usually performed in a temperature-controlled chamber which can be pressurized and evacuated. The geometric dimensions of the real wind tunnel setup (distances: camera $\leftrightarrow$ PSP; illumination $\leftrightarrow$ PSP) are simulated at the calibration rig. The luminescence intensity is captured at precisely known pressure(s) and temperature(s). Finally a suitable calibration fit represents the coefficients in Equ. 2.1.12. The paint sample should have the same surface properties (material, roughness, ...) and experience the same paint treatment (no. of layers, heat curing, ...) as the model coating in order to avoid a sensitivity change that would cause a potential bias error.

From the fact that the minority of wind tunnel facilities can be pressurized, the term in-situ calibration is also used for a hybrid approach. The general paint properties are characterized in an a-priori calibration. This calibration delivers the raw PSP results which are finally cross-checked and corrected with the readings from static pressure ports within the model. For this, the luminescence intensity in the vicinity of the pressure ports is plotted against the actual static port pressures and a rule is derived which corrects a potential mismatch between both quantities. This approach also accounts for external influences during a wind tunnel experiment like paint contamination, aging or a potential temperature effect.

The a-priori calibration setup developed at UniBwM (Bitter et al. (2009)) is shown in Figs. 2.6 and 2.7. The chamber is made from aluminum and is designed to calibrate

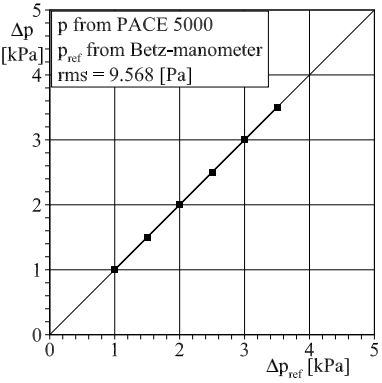

Fig. 2.8.: Accuracy assessment of the static calibration pressure. Actual pressure p measured with the *PACE 5000* pressure controller; reference pressure p_{ref} measured by a Betz-manometer.

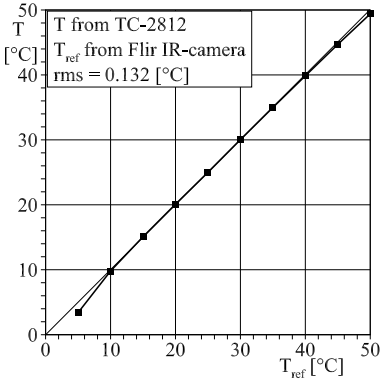

Fig. 2.9.: Accuracy assessment of the static calibration temperature. Actual temperature T measured with the *TC-2812* temperature controller; reference temperature T_{ref} measured by a *FLIR Titanium 560M* IR camera.

paints in the range from $[5 \leq p_{\mathrm{s}} \leq 700]$ kPa, especially to cover the static pressure range of the trisonic wind tunnel facility (TWM, see Section 5.1.1). The static air pressure inside the chamber is controlled by a *GE Pace 5000* pressure controller with extended precision (0.01 % *FS*, $FS = 700$ kPa). Evacuation down to $p_{\mathrm{abs}} \approx 5$ kPa is done by a membran vacuum pump. For the temperature adjustment in the calibration chamber, a *Quickcool HDPM* high-power thermoelectric device (Peltier heater) is used which has a design temperature difference of $\Delta T = 71$ K between the hot and the cooled side. This device is glued on the chamber's cupper base. The base bears a cooling ductwork that is rinsed with thermally conditioned water. The static temperature is sensed with a resistance thermometer device (RTD 100) controlled by a *Cooltronic TC-2812* temperature controller with 0.1 K control precision. A PSP/TSP paint sample is positioned and fixed on top of the heating device. The accuracy and reproducibility of the calibration setting values such as pressure and temperature was assessed in Figs. 2.8 and 2.9. The static chamber pressure set by the pressure controller was cross-checked with an independent measurement of the actual static chamber pressure measured with a Betz-manometer that had an effective range up to 4 kPa. The hysteresis between upward and downward measurements was negligible (about 10 Pa). The RMS uncertainty between the actual static pressure and its setting value was about 10 Pa within the tested range. Two in-

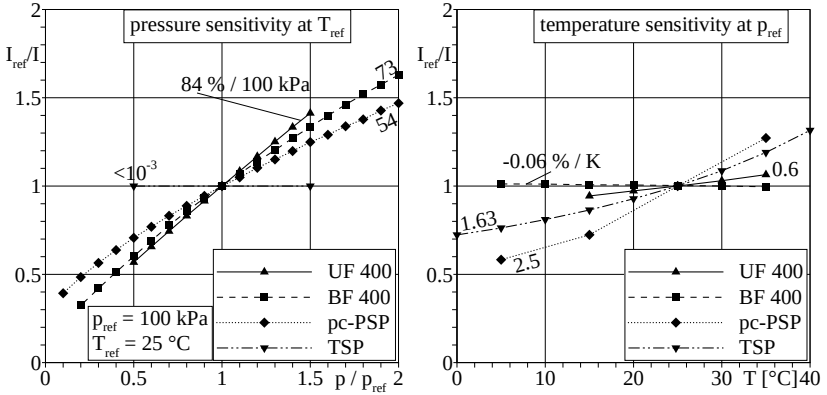

Fig. 2.10.: *Left:* Stern-Volmer calibration curves of the prominent pressure- and temperature-sensitive paints and their pressure sensitivities at reference temperature; *Right:* temperature sensitivities at reference pressure.

dependent measurements of the actual and the desired surface temperature of the paint sample were made while the desired temperature was set by the temperature controller of the setup and the actual temperature of a black paint sample was monitored by a *FLIR Titanium 560M* infrared camera. The results reveal a perfectly linear behavior within temperatures of $[10 \leq T \leq 40]\,^{\circ}\mathrm{C}$. The RMS deviation of $0.13\,^{\circ}\mathrm{C}$ was within the accuracy of the setting device.

After these benchmarks, 4 individual paint samples were prepared and calibrated. Each sample carried a different paint such as: uni-PSP (UF400), binary-PSP (BF400), transient polymer/ceramic PSP (pc-PSP) and temperature-sensitive paint (TSP). The paint excitation was performed by an *ISSI LM2X-DMHP* 405 nm high-power LED. The luminescence signal was captured with a 14-bit cooled interline CCD camera (*pco.2000*) equipped with appropriate filters according to the specific emission spectra. Hence, a band-pass filter with $\lambda = (550 \pm 50)\,\mathrm{nm}$ and a 640 nm long-pass filter with high optical density ($OD > 6$) were used for the reference and the pressure signals respectively. The TSP luminophor emission was separated using a 570 nm long-pass filter. The uni- and binary-PSP samples were initially covered with a screen layer. The TSP sample was covered with a $100\,\mu\mathrm{m}$ conventional white base coat (*Glasurit*) for thermal insulation. All samples were heat-cured in an oven for about 1 hour at $60\,^{\circ}\mathrm{C}$. During the fully automatic calibration procedure the chamber was allowed to balance for 2 minutes after significant pressure and temperature changes ($\Delta p > 10\,\mathrm{kPa}$ or $\Delta T > 5\,\mathrm{K}$). The LED only flashed during data acquisition in order to avoid photo-degradation. The calibra-

tion results for the different samples are displayed in Fig. 2.10, showing the individual Stern-Volmer calibration curves at reference conditions (*left*: pressure sensitivity; *right*: temperature-dependency). All plots were normalized with the reference intensity close to ambient conditions ($p_{\mathrm{ref}} = 100\,\mathrm{kPa}$, $T_{\mathrm{ref}} = 25\,^{\circ}\mathrm{C}$).
By having the same pressure-sensitive luminophor (PtTFPP), a potential difference in the paint composition and the additional reference probe affected the pressure sensitivity of the uni-paint in comparison with the binary-PSP by about 10 %. The temperature dependency was decreased from $0.6\,\%/\mathrm{K}$ down to $-0.06\,\%/\mathrm{K}$ by using the compensation of the reference dye.
The pressure sensitivity was about $p_{\mathrm{sens}} \approx 54\,\%/100\,\mathrm{kPa}$ for the transient pc-PSP. This paint also revealed a very high temperature dependency of $T_{\mathrm{sens}} \approx 2.5\,\%/\mathrm{K}$. This dependency is obviously even higher than the sensitivity of the actual temperature-sensitive paint. This is mainly caused by the composition of the polymer/ceramic binder. A careful knowledge of the surface temperature is essential for high-accuracy measurements with the transient pc-PSP. The first-order transfer function of pc-PSP was evaluated in a high-frequency acoustic tube within a frequency range of $0.1 \leq f \leq 10\,\mathrm{kHz}$ by Sugimoto et al. (2012). As reported, a widely constant amplitude ($\Delta A \leq -0.5\,\mathrm{dB}$) and phase angle ($\Delta\varphi \leq 10\,^{\circ}$) is present for pc-PSP up to sampling rates of $f \approx 4\,\mathrm{kHz}$. For transient measurements with sampling rates higher than 4 kHz, the amplitude dropped by approx. $\Delta A \approx -1\,\mathrm{dB/\,kHz}$ and the phase angle delayed by $\Delta\varphi \approx 8\,^{\circ}/\,\mathrm{kHz}$.
The TSP showed nearly no pressure dependency and had a temperature sensitivity of about $1.6\,\%/\mathrm{K}$. The individual results also reveal why a polynomial approach is typically more convenient for the approximation of the paint characteristics in comparison to the linear Stern-Volmer model.

2.2. Particle image velocimetry (PIV)

2.2.1. Basic principle

The particle image velocimetry (PIV) is an optical method for the contactless determination of the flow velocity field in a transparent fluid. The method was developed in the mid-1980s, see Adrian (1986). The principle of this optical measurement technique is based on the determination of displacements of tracer particles from digitally recorded images through correlation-based methods. For the determination of a velocity field, small light scattering particles (called: tracer particles or seeding) are injected into the flow. The particles are illuminated twice in a light-sheet at time steps t and $t + \Delta t$ by a short-pulse light source, such as a laser. The illuminated particles are imaged through optical lenses and their signal is digitally recorded in a PIV image at each time step using an image sensor (CCD, CMOS, ...). From the estimated displacement $\Delta\vec{s}$ of a particle image ensemble in two consecutive PIV images, from the knowledge of the time

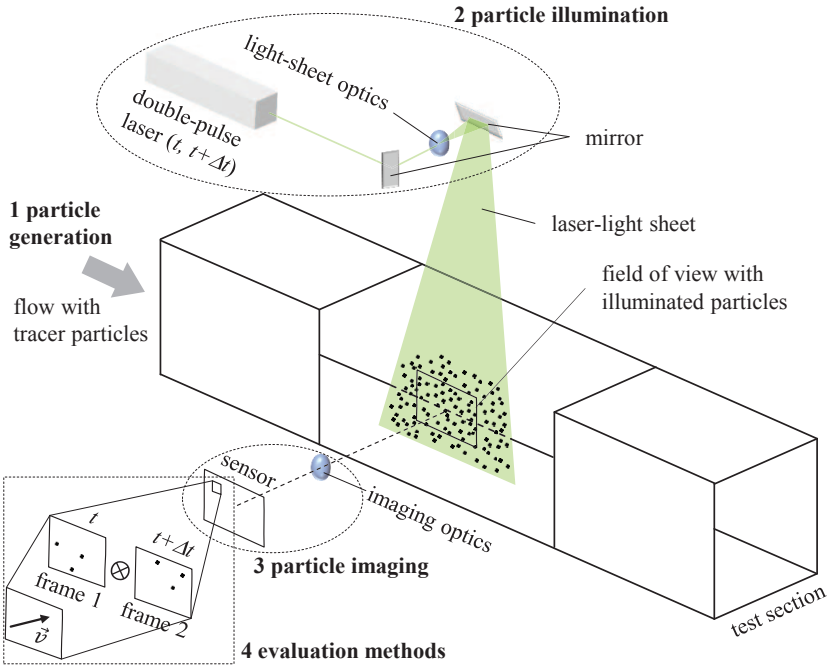

Fig. 2.11.: Principle arrangement of a planar particle image velocimetry (PIV) setup in a wind tunnel for the estimation of a 2C2D velocity field.

interval Δt and by knowing the magnification of the imaging optics M the local velocity vector can be calculated as:

$$\vec{v} = \frac{\Delta \vec{s}}{M \Delta t}. \tag{2.2.14}$$

Figure 2.11 schematically displays a classical PIV setup for the determination of two components of a velocity vector in a plane (2 components in 2D $\rightarrow$ 2C2D-PIV). There are more sophisticated extensions of the conventional 2C2D-PIV setup, like 3C2D- or 3C3D-PIV, that allow the determination of the full three-component velocity vector by the use of multiple cameras. These more sophisticated versions are not within the scope of this thesis and will not be discussed here. The subsystems that make up a 2C2D experimental setup as well as fundamentals of correlation-based evaluation techniques are explained below. More details on the individual components, on the generation of tracer particles or on the variety of evaluation approaches are discussed in detail in Raffel et al. (2007).

2.2.2. Particle generation

Strictly speaking, PIV does not measure the flow velocity but the convection of individual tracer particles. This necessarily requires a good follow-up performance of the seeding particles to the flow. Obviously, large and heavy particles appear too inert to resolve fluid flows with strong gradients. As reported in Raffel et al. (2007), the diameter of a single tracer particle and its density difference with respect to the fluid dominate the follow-up performance. For aerodynamic tests in wind tunnels, small droplets are often used which are produced from a highly viscous fluid within a seeding atomizer. Pressurized air is pushed through the nozzles of such an atomizer what produces the small droplets. The use of conventional salad oils or DEHS (di-ethyl hexa-sebacate) as seeding fluid has prevailed. DEHS was used for the experiments in this thesis. These fluids typically produce droplets with an average diameter of 0.5-5 μm, compare Kähler et al. (2002). As a compromise, such particles are able to follow the flow over a wide dynamic range (e.g. wake of a backward-facing step) and their scattering signal is well detectable on an image sensor. The seeding particles for aerodynamic testing should not be smaller than the dominant wavelength which illuminates them (green light $\lambda = 530\,\text{nm}$ = $0.53\,\mu$m). Otherwise, their scattering intensity appears intermittently at larger distances of observation. At the department, several seeding atomizers are available which produce tracer particles from DEHS in a suitable size and concentration.

2.2.3. Particle illumination

Solid-state lasers with twin-cavities established for double-pulse illumination in standard PIV applications. Special crystals (e.g. neodym-doped yttrium aluminum garnet - Nd:YAG) form the laser medium of such lasers in order to emit monochromatic light. Therefore, the laser medium has to be excited by an external energy source. The excitation in a solid-state laser is usually made by a flash lamp or a diode. From the photophysical view, the stimulated emission plays the essential role in a laser. A molecule of the laser medium that was excited can use the excitation energy of an impacting photon in a way that it produces a second photon of similar wavelength and propagation direction during its relaxation to the ground state. In order to force the stimulated emission, the laser medium is usually located between 2 mirrors (resonator). By reflecting the photons between the two mirrors, more and more photons are produced. The photons are reflected until one of the mirrors is opened and a package of photons may escape from the resonator. This is detectable as a short pulse of monochromatic light. The very precise and fast shuttering of the resonator mirror is done by a Q-switch which ensures an identical emitted radiation power for each laser pulse. The whole assembly from the laser medium, the resonator, the flash lamp and the Q-switch is known as laser cavity.
In a double-pulse laser, two laser cavities are embedded whose individual beams are

joined in special optics. The delay Δt between both laser pulses has to be adjusted carefully because it determines the shift of the imaged particle ensembles. For a reliable calculation of the local flow vector, the particle displacement within a PIV image $\vec{d}$ should be 8-10 px. Hence, the pulse delay is strongly dependent on the dynamic of the flow phenomena which are investigated as well as the optical magnification of the imaging system. For time-resolved or transient PIV measurements, high-repetition-rate solid-state lasers with typical pulse rates up to 10 kHz are available.
By using a conventional 2C2D-PIV setup, the tracer particles will be illuminated in a plane (laser-light sheet) of finite thickness that is formed from the laser beam and whose thickness is adapted to the flow properties. For the formation of the light sheet, the beam is passed through an array of lenses. The thickness of the light sheet should be minimal, since the detected signal of the scattering particles always represents an integration over the depth of the laser plane. In 3D-flows with strong gradients, the particles might be transported perpendicular to the light sheet. Thus, a thick light sheet might produce a potential uncertainty in the local flow vector by a strong out-of-plane motion of tracer particles. This motion cannot be detected by a conventional 2C2D-PIV setup but with a more sophisticated multiple-camera approach. In a thin light sheet, some particles might disappear between the two light pulses what would impede their digital evaluation.

2.2.4. Particle imaging

Digital CCD or CMOS cameras established for the recording of the signal from the illuminated tracer particles. They have a high quantum yield in the wavelength region of most PIV lasers. A high SNR and high dynamic ranges of up to 16 bit ensure that the particles can be imaged sufficiently even under low light conditions. Camera technologies with multiple-exposure option have been developed. They are able to capture the displacement of particles in a double-frame image at the time steps t and $t + \Delta t$. This acquisition technique is known as double frame/single exposure technology and is also applied within the scope of this thesis. Modern cameras offer large sensor resolutions up to 16 Mpx or allow the double exposure within a delay of $\Delta t \leq 750$ ns (e.g. interline- or frame-transfer cameras). High-speed CMOS cameras are available for the transient PIV measurements that provide a sensor resolution of 1 Mpx and a recording rate of 16 kHz at full resolution.
The particle image quality plays a crucial role for accurate PIV measurement. The particle image should be round without blurring. The measurement uncertainty additionally depends on the size of the particle image. The diameter of a particle image should be 2-3 px for the lowest measurement uncertainty, see Raffel et al. (2007). It is also recommended to adjust the optical setup carefully and use high quality optical components in order to reach high-quality particle images with reduced aberrations.

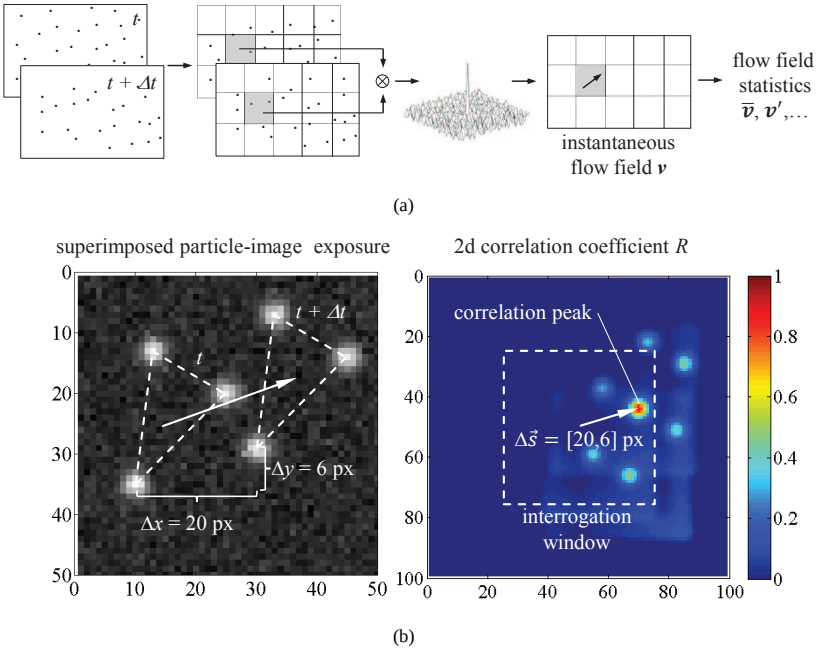

Fig. 2.12.: *(a)* Schematic of a standard cross-correlation PIV principle; *(b)* Vector determination from the correlation plane of an interrogation window; *Left:* Summation of a particle ensemble exposed at t and $t+\Delta t$. The ensembles displacement was $\Delta\vec{s} = [20;6]$ px; *Right:* Two-dimensional correlation coefficient plane between the first and second exposure.

2.2.5. Evaluation methods

Modern PIV data evaluation is widely based on window-correlation methods, compare Keane and Adrian (1992) or Raffel et al. (2007). A schematic of a classical PIV cross-correlation evaluation is sketched in Fig. 2.12 (a). The individual PIV double-frame images are sub-divided into squared interrogation windows. The interrogation window size typically ranges from 128 px × 128 px down to 8 px × 8 px whereas the interrogation windows may overlap by a certain amount in order to increase the resolution of the vector field result. (Note: squared interrogation regions are abbreviated by a shorter notation, e.g. 128^2 px^2, in the following context). The final size of the interrogation windows restricts the resolution of the vector field result. Each interrogation window

represents a local flow vector. If the size of the interrogation windows is chosen too small or the particle shift between both laser pulses is too large, the particle ensemble might have exceeded the corresponding interrogation windows and hence their evaluation is impeded. However, state-of-the-art evaluation algorithms (e.g. iterative window deformation schemes) can help to correlate the data from both interrogation windows. An average density of 6-8 particles should be present in all individual interrogation windows.
A particle image ensemble from three particle images inside an interrogation window of 50^2 px^2 was synthetically shifted by $\Delta\vec{s} = [20{,}6]$ px between the time steps t and $t+\Delta t$ as to be seen on the left in Fig. 2.12 (b) (Note: usually, there would be two individual PIV frames which were superimposed in the figure for the clarification of the evaluation procedure). The particle image ensembles were added up with 2 % Gaussian noise. The two-dimensional cross-correlation between the time steps t and $t+\Delta t$ is performed using the fast Fourier transform (FFT). At the point of greatest similarity between the two image signals a maximum forms in a correlation plane, as indicatd on the right in Figure 2.12 (b). The distance between this maximum and the center of the correlation plane is directly proportional to the shift of the particle ensemble. The position of the maximum $[x_0; y_0]$ can be estimated from three-point estimators with sub-pixel accuracy. Therefore, the peak can be fitted by various fit functions, see Raffel et al. (2007). For a Gaussian fitting, the peak locus is approximated by:

$$x_0 = i + \frac{\ln R_{(i-1,j)} - \ln R_{(i+1,j)}}{2\ln R_{(i-1,j)} - 4\ln R_{(i,j)} + 2\ln R_{(i+1,j)}} \tag{2.2.15}$$

$$y_0 = i + \frac{\ln R_{(i,j-1)} - \ln R_{(i,j-1)}}{2\ln R_{(i,j-1)} - 4\ln R_{(i,j)} + 2\ln R_{(i,j-1)}}$$

The shift of the particle image ensemble is finally estimated by calculating the difference between the peak locus and the center of the correlation plane. The complete evaluation of all interrogation windows in a PIV double-frame image leads to an instantaneous vector field result. A large number of samples ($200 < N < 20{,}000$) is typically recorded and evaluated in order to extract flow properties and reliable statistics (e.g. mean flow or fluctuations).
Meinhart et al. (2000) introduced an approach that increased the SNR and the spatial resolution by averaging the correlation planes of the individual interrogation windows, as schematically shown in Fig. 2.13. This approach, known as sum-of-correlation technique, was intentionally developed for micro-fluidics. The benefit of averaging the correlation planes is that the size of the interrogation windows can be reduced while the spatial resolution is increased. If the number of PIV double-frame recordings N is sufficiently high, there is a certain probability that a correlation peak establishes even if the size of the interrogation window is smaller than the average particle shift. The drawback

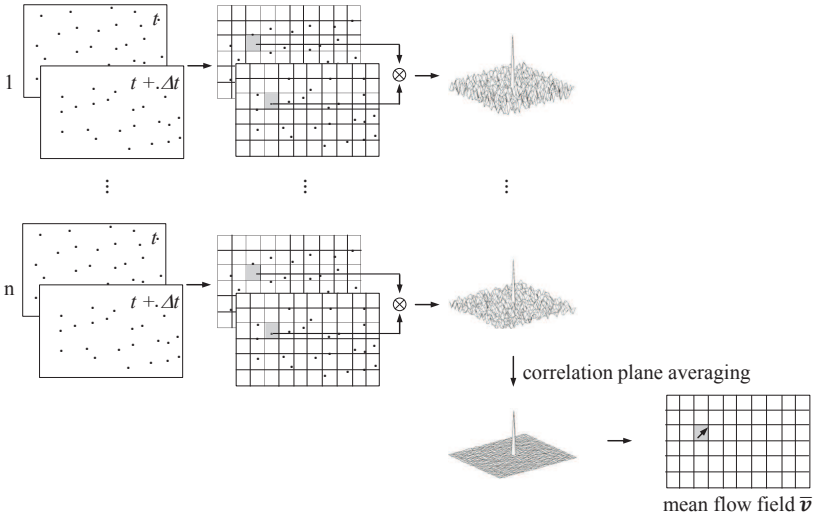

Fig. 2.13.: Schematic of a PIV evaluation based on the averaging of the correlation planes, as proposed by Meinhart et al. (2000).

of this technique was that all statistical information (e.g. Reynolds shear forces $-\overline{u'v'}$) vanished so that the final vector field only represents the mean flow field. However, modern methods allow the extraction of the turbulent flow properties from the shape and orientation of the correlation peak, as reported by Scharnowski et al. (2012). The minimum interrogation window size for sum-of-correlation evaluations should be not smaller than the size of the actual particle images as reported in Kähler et al. (2012a). Both, standard cross- and sum-of-correlation evaluation schemes were applied in order to derive the results from the PIV measurements within this thesis.

3. Relevant PSP error sources

The error sources discussed below does not address luminophor-specific bias effects (e.g. photo-degradation) because these are usually characterized by the paint developers and documented in the data-sheets (e.g. photo-degradation rate of PtTFPP $\approx 1\,\%/\,\mathrm{h}$, compare ISS Inc. (2013)). The study moreover encounters some effects that are specific under the constraints of the experimental setups in the wind tunnel facilities at UniBwM. The error sources are dominant for the mismatch between the raw PSP results and the readings from static reference pressure ports. As a consequence, the application of an in-situ correction to the raw PSP results becomes necessary. The individual effects as well as their order of magnitude are examined here. The knowledge of the magnitude of the individual error sources can be helpful to estimate the measurement uncertainty of the entire PSP system. Some correction techniques are introduced in order minimize the final measurement uncertainty. A more detailed analysis of all sensitivity parameters is presented in Liu and Sullivan (2005).

3.1. Temperature effect

The PSP calibration plots which were discussed earlier revealed that most PSP coatings somehow suffer from a certain temperature dependency. Model surfaces might be exposed to strong temperature changes of several Kelvin during transonic test conditions as a consequence of compressibility effects. Hence, the surface temperature must be known precisely in order to measure high-accuracy pressure distributions.
The application of a binary paint was already introduced for minimizing the temperature dependency. Nevertheless, theses paints also have a small temperature dependency. That's why surface temperature sensors are typically used on model surfaces. This combination of a binary PSP and a surface temperature sensor is particularly suitable for transonic applications. At low-speed conditions the usage of an uni-PSP in combination with a temperature sensor typically delivers sufficient results.
The usage of a TSP, either subsequently or in parallel to a PSP experiment, is the second option that is applied at the institute. The temperature information from the TSP is mapped on the PSP results for the compensation of the temperature effect.
A *FLIR Titanium 560M* infrared camera is partly used to determine the surface temperature. It offers a temperature resolution below 0.1 K. This application is restricted since

the test sections of the wind tunnels only have limited IR-aware glazing.
A fourth alternative is the static surface temperature from a numerical simulation. If the opportunity is missing to use one of the options discussed up to here, the surface temperature T_{aw} might be estimated by applying the adiabatic wall model:

$$T_{aw}/T_0 = [1 + r(\kappa - 1)M_\infty^2/2][1 + (\kappa - 1)M_\infty^2/2]^{-1} \tag{3.1.1}$$

whereas r is the recovery factor of the local boundary layer profile, T_0 is the total temperature, M_∞ is the flow Mach number and κ the specific heat. Hence, this error is strongly dependent on both, the temperature-dependency of the PSP coating and the accuracy of the temperature measurements.

3.2. Excitation non-uniformity

Since the intensity signal of a PSP is directly proportional to the intensity of the excitation, the measurement accuracy is also depending directly on the temporal and spatial uniformity or stability of the excitation. No matter, if the excitation source or the model moves, both effects introduce a potential measurement error into the final PSP results. This section examines the magnitude of such a relative motion.
In the past, mercury arc lamps were used for the excitation of PSPs because they produced a high intensity of (near-) ultraviolet light. The major disadvantage of these lamps was a strong fluctuation of the light intensity up to several percent because the light is produced by a random spark discharging process. Nowadays, LEDs are widely used for fluorescence applications because they combine several advantages: 1. They are commercially available in a variety of narrow-band emitting wavelengths; 2. High-power emitter (arrays) easily reach an optical output of 100 W or more; 3. The intensity distribution is smooth and continuous (no speckle); 4. The output intensity is very constant ($\Delta I < 0.1\,\%$/h). Thus, the temporal non-uniformity of a modern PSP excitation using LEDs is assumed to be negligible for further considerations. Hence, the spatial variation of the illumination pattern as a consequence of a lamp vibration or a model motion is assumed to be the dominant error source.
The intensity pattern of any light source has a characteristic profile (e.g. Gaussian or top-hat). This pattern might have a significant influence if the intensity ratio of two sub-sequent imaged pattern is considered. The magnitude of the effect is dominated by the potential shift between the sub-sequent pattern images and by the optical magnification M of the imaging system. Typical PSP experiments are conducted with optical magnification in the range of $0.1 \leq M \leq 0.001$ (large models are observed from a long imaging distance). A model motion or deformation of e.g. 0.5 mm as a consequence of aerodynamic forces between wind-on and wind-off conditions might not be noticeable on the imaging sensor because the actual shift is typically below 1 px. The image sensor cannot resolve this shift but it would increase the noise in the final intensity ratio. In

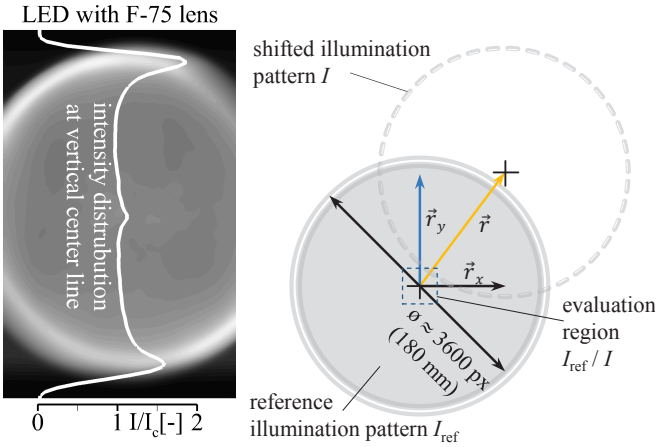

Fig. 3.1.: *Left:* Intensity field and center-line intensity distribution of a *Luminus CBT-120 uv* high-power LED with a $F = -75\,\text{mm}$ spherical front-lens; *Right:* not-to-scale schematic of the synthetic illumination pattern shift along the shift radius $\vec{r}$.

PSP experiments which are conducted at large magnifications ($M > 0.1$) (small models or model portions are observed from a short distance), the motion of 0.5 mm can cause a shift of several pixels in the intensity image. This would lead to an enormous increase in the noise level of the intensity ratio. This effect is intensified if the excitation source has a narrow-angled illumination pattern with a strong intensity gradient.
The spatial and temporal non-uniform behavior of a high-power LED as typically used for PSP excitation at UniBwM was simulated in the following. This non-uniformity can be interpreted as a vibration of the light source or a model motion between the resting wind-off condition and various sub-sequent wind-on PSP intensity images (e.g. transient PSP measurements).
The left-hand side of Figure 3.1 shows the LED intensity pattern as it was projected on a white diffused screen ($D \approx 180\,\text{mm} \approx 3{,}600\,\text{px}$; magnification $M \approx 0.15$) and imaged by an 11 MPx camera (*pco.4000*). The intensity pattern of the LED was synthetically shifted horizontally and vertically within a range of $[-400 \leq \vec{r} \leq 400]\,\text{px}$ with $\Delta\vec{r} = 0.5\,\text{px}$ as the step size. The ratio between the initial and the shifted intensity pattern can be interpreted as the intensity ratio I_{ref}/I. The LED was equipped with a spherical lens (diameter: $D = 100\,\text{mm}$, focal length: $F = -75\,\text{mm}$) that compensated the illumination characteristic and homogeneously maximized the intensity profile, as indicated by the white line profile in Fig. 3.2. The peak in the center of the profile is caused by

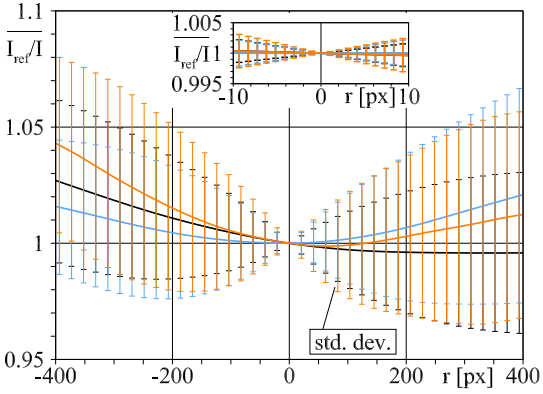

Fig. 3.2.: Error in the intensity ratio as a consequence of a synthetic shift along the vector $\vec{r}$. The solid lines represent the mean intensity ratio and the error bars reflect the standard deviation.

the LED emitter which is imaged by the lens. Optical aberrations are caused in the outer portions due to refractions on the edge of the lens as indicated by the two peaks. The intensity ratio between the shifted and the non-shifted reference pattern was calculated within a $7^2\,\mathrm{px}^2$ evaluation region in the center of the reference pattern (*dashed square*). The results are shown in Figure 3.2 for the horizontal (*black*), the vertical (*blue*) and the combined shifts (*orange*). The solid lines show the mean intensity ratio $\overline{I_{\mathrm{ref}}/I}$ within the evaluation region and the error bars represent the standard deviations σ. The slopes of the curves are slightly asymmetric due to the rectangular LED-emitter area and a slight misalignment of the optical axis between the emitter and the lens. The closeup shows the results between $[-10 \leq \vec{r} \leq 10]\,\mathrm{px}$. Within this range, the mean intensity ratio is affected by less than 0.03%. The standard deviation in this area is 0.3% at its maximum. A spatial filtering of the intensity ratio is mandatory in PSP applications in mostly any case. Hence, the average from the mean deviations $\overline{I_{\mathrm{ref}}/I}$ and the standard deviation is assumed to represent a conservative estimation of a potential measurement uncertainty. A shift of $\leq 10\,\mathrm{px}$ can cause an uncertainty of about 0.16% (or $\approx 200\,\mathrm{Pa}$) in the final pressure distribution if a PSP coating is applied that has an assumed pressure sensitivity of 76%/100 kPa (e.g. binary-PSP). This effect can be countered by a rigid experimental setup or an artificial reduction of the image resolution (e.g. de-focussing, pixel-binning).

3.3. Self-illumination

Self-illumination (SI) is a typical error source in fluorescence applications such as intensity-based measurement techniques. It occurs if the luminescence intensity superimposes on adjacent surfaces as it is the case for complex wind tunnel geometries (e.g. wing-body-tail configuration). During a PSP measurement, pressure and temperature-dependent superpositions of luminescence signals can occur at the geometry intersections (e.g. wing with body or tails with body). Within the following section, the SI-effect is introduced and the radiosity algorithm is presented and experimentally validated for its correction.

3.3.1. Reflection models

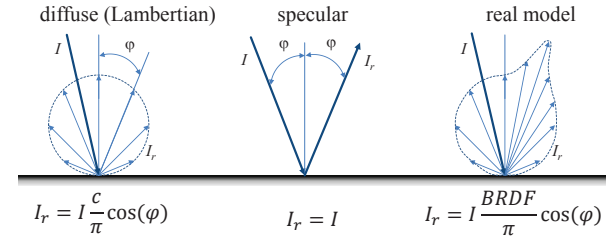

Fig. 3.3.: Reflection models that are widely used in computer graphics for the simulation of light scattering; *Left:* ideal diffuse (Lambertian) model; *Center:* ideal mirror reflection model; *Right:* real light model.

Three widely applied approaches for modeling light reflection properties in computer graphics are presented in Figure 3.3. The Lambertian model (*left*) describes the ideal diffuse reflection of light on a diffuse surface by means of:

$$I_\mathrm{r} = I\frac{c_\mathrm{r}}{\pi}cos\varphi \tag{3.3.2}$$

whereas the reflected intensity I_r has a fixed scattering characteristic by the term $cos(\varphi)$ and just depends on the intensity of the incident light I and the absorption coefficient c_r of the scattering surface. The absorption coefficient indicates how much light is absorbed or reflected on the surface. It is defined between 0 (black body) and 1 (white surface with ideal diffuse properties).
The second case, the specular model, which is shown in the middle of Fig. 3.3 represents the ideal reflection of the incident intensity I, such as $I_\mathrm{r} = I$ applies. The specular model is valid for mirroring screens with high optical quality and low surface roughness.

A reflection model that better expresses real light behavior combines the terms of a diffuse model with the direction-depending character of the specular model, comparable to the model presented on the right in Figure 3.3. Global illumination components (e.g. background light) and properties of the reflecting surface (non-/isotropy) moreover complete the real light model. These terms are typically combined in a direction-dependent model that is specifically dependent from the surface material. This model is known as bi-directional reflection distribution function (BRDF). Thus, the modeling of real-light scattering and propagation is much more complex. A widely used model for the simulation of real scattering properties is the Phong model, compare Phong (1975). Its BRDF sums up the individual diffuse k_d and specular components k_s, such as:

$$\mathrm{BRDF}_\mathrm{Phong}(\alpha) = k_\mathrm{d} + k_\mathrm{s}\frac{n+2}{2}cos^n(\varphi) \tag{3.3.3}$$

The angle φ describes the angle between the surface normal and the scattered light. The factor n is used to simulate the reflection properties of the surface.

3.3.2. The self-illumination effect

The SI-effect is illustrated on a 2D concave corner in Figure 3.4. The scene with two elements (not necessarily) having the same absorption coefficients c_r is illuminated with radiation of intensity I_e. The intensity I_r is reflected on the surface whereas $\lambda(I_\mathrm{r}) = \lambda(I_\mathrm{e})$ holds. The light scattering characteristics symbolize the ideal-diffuse (*dashed blue*) and the real-light scattering (*solid blue*). Considering element 2, it is evident that this element experiences I_e as well as the reflected intensity from the element 1 ($I_{\mathrm{r},1}$). Since both portions have the same wavelengths, their portions superimpose such as $B = I_\mathrm{e} + \sum I_\mathrm{r}$. This effect is trivially valid in reverse. It can be shown that the normalized total radiation power B is nearly doubled in the vicinity of the intersection of both surfaces at $l = 0$ as reported by Le Sant (2001). The first-order influence of this effect has theoretically decayed with increasing distance from the intersection at $l = h$. This SI-effect is primarily dependent on the geometry of the scene. Unless the excitation is stable in time and position, this self-illumination effect plays no role in PSP applications because it cancels out in the intensity ratio I_ref/I.
A secondary SI-effect is stimulated by the luminescence of a PSP. The same scene as before is reconsidered in Figure 3.5 experiencing the same excitation I_e. A PSP coating was applied to the surfaces. This PSP's luminescence I_l is both dependent on the excitation intensity as well as sensitive to pressure and/or temperature changes. Analogous to the sample discussed above, the luminescence will be scattered at the elements 1 and 2. The luminescence scattering characteristic of the PSP is sym-

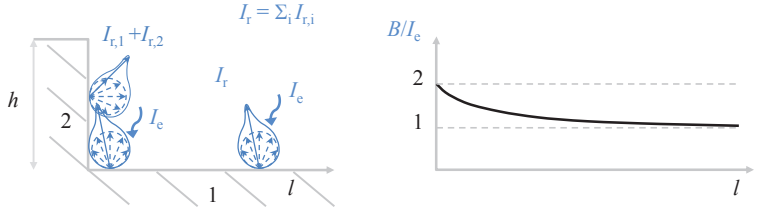

Fig. 3.4.: Superposition of excitation intensity at adjacent surfaces; *Left:* self-illumination at a rectangular corner due to the excitation I_e; The superposition of intensities cancels out in an intensity ratio if the excitation is stationary and the geometry remains unchanged; *Right:* relative increase of the total radiation power B on the horizontal element due to superimposed intensities.

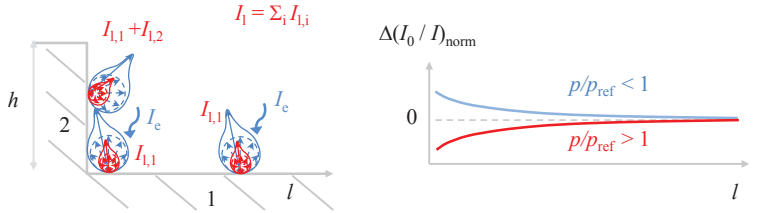

Fig. 3.5.: Cross effects between excitation and luminescence intensities at adjacent surfaces; *Left:* self-illumination at a rectangular corner due to the excitation I_e and luminescence intensity I_l; I_l changes with pressure, temperature and I_e and hence does not cancel out in the PSP intensity ratio; *Right:* relative intensity change with ambient pressure p on the horizontal element due to excitation I_e and luminescence intensity I_l.

bolized by the red distributions. A superposition of the excitation intensities in the vicinity of the intersection causes an increase in the luminescence intensity. If the scene is steady and stationary, this effect cancels out in the intensity ratio. Unlike the previous example, the SI-effect cannot be eliminated by forming the ratio of I_{ref}/I, as the pressure (and usually) the temperature changes in a PSP experiment. Thus, the luminescence power in the vicinity of the intersection is not constant but is changing between wind-off and wind-on conditions. This means, that a pressure (and temperature) dependent SI-effect occurs.

The self-illumination effect based on the superposition of luminescence intensities was experimentally examined in the static PSP calibration chamber on a perpendicular corner. The scattering properties of the intersecting surfaces were varied. Figure 3.6 shows the studied configurations. The base plate (*center*) had dimensions of $28^2\,\mathrm{mm}^2$. It was

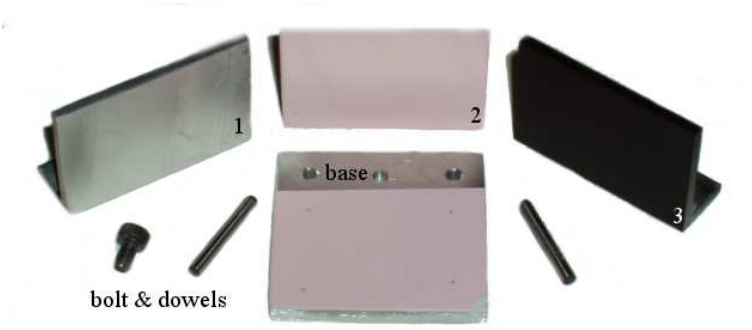

Fig. 3.6.: Samples for the experimental characterization of the SI-effect in the static PSP calibration chamber; base plate: binary-PSP; adjacent surfaces: 1. frosted aluminum, 2. binary-PSP and 3. diffuse black paint.

coated with the PSP coatings UF400, BF400 and pc-PSP. Three adjacent configurations were prepared for each base plate: 1. a frosted aluminum plate (*1* in Figure 3.6); a plate that carried the same PSP coating as the base plate (*2*) and a plate with a black absorber coating (*3*). The individual surfaces had a height of $2/3$ of the base plates length. They were attached to the base plate with dowels and a bolt. This ensured that the SI-effect occurred at the same spatial position for all configurations. The configuration with the binary-PSP (BF400) is discussed in the following. The results of the remaining PSPs can be found in Appendix A.
The samples were calibrated in the static calibration at a constant temperature $T = 25\,^{\circ}\mathrm{C}$ and static pressures in the range of $[20 \leq p_\mathrm{s} \leq 200]\,\mathrm{kPa}$ with $\Delta p = 20\,\mathrm{kPa}$. The PSP was excited with a 405 nm high-power LED from a distance of about $l = 400\,\mathrm{mm}$. The luminescence signal was recorded by two *pco.2000* CCD cameras equipped with appropriate signal filters.
Figure 3.7 shows the SI-effect for the three configurations (from left to right) at two static pressures $p/p_\mathrm{ref} = 1 \pm 80\,\%$. The reference pressure was $p_\mathrm{ref} = 100\,\mathrm{kPa}$. The view to the base plate is from the top and the adjacent surface points out of the image plane (*fat black line*). For the calculation of the relative effect in the intensity ratio $\Delta I/I_\mathrm{ref}$, the intensity ratio was normalized with a value at the lower edge. It was assumed that the first-order influence has already decayed at this position. Therefore, the relative change in the intensity ratio is always close to zero at the lower edge of the base plate. It is apparent that configuration 1 and 2 produce a clearly noticeable intensity change whereas the third configuration does not. Changing the pressure by 80 % results in an intensity-ratio change in the vicinity of the intersection by about $\pm 2\,\%$. Furthermore, configuration 1 and 2 show different SI-effect characterisitcs which are

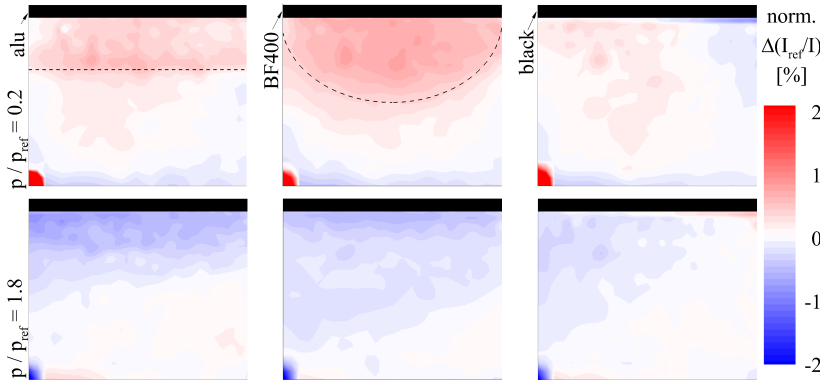

Fig. 3.7.: Experimentally determined self-illumination effect on a rectangular corner whose base plate was covered with binary PSP (BF400). Adjacent surfaces (from left to right): aluminum, PSP, black paint; *Top row:* SI-effect for $p/p_{\mathrm{ref}} = 0.2$; *Bottom row:* SI-effect for $p/p_{\mathrm{ref}} = 1.8$; $p_{\mathrm{ref}} = 100\,\mathrm{kPa}$.

highlighted by the dashed lines. Configuration 1 (frosted aluminum) shows the characteristic of an anisotropic surface which is dependent on the surface material and the viewing direction and that cannot be described by the simple Lambertian surface but by the real-light model, see Ruyten (1997). Configuration 2 (*PSP* $\leftrightarrow$ *PSP*) shows the characteristics of a Lambertian diffuse surface. Here, the SI-effect shows a maximum in the center of the base plate and it drops to the edges of the configuration, compare Ruyten (1997). The slightly asymmetrical intensity distribution can be explained by a suboptimal heat flow between the base plate and the Peltier heater placed underneath the sample for tempering.
The black plate in configuration 3 acted as an absorber. Hence, the SI-effect almost completely vanished for all calibrated pressures at this configuration. In general, it can be concluded from the results that the observed effect is substantially lower than it is expected from the literature, compare Ruyten (1997); Le Sant (2001). The authors reported intensity changes by 25 % and more as a consequence of the self-illumination. Compared with other PSP error sources (e.g. temperature sensitivity), the influence of the SI-effect with $\pm 2\,\%$ at enormous pressure differences of $\pm 80\,\%$ is rather low. Nevertheless, the implementation of the radiosity-algorithm is presented in the following which can be used to correct the SI-effect at complex geometries in order to get high-accuracy PSP results.

3.3.3. Radiosity - diffuse light modeling

The radiosity method models the propagation of radiation (light or heat) in a scene based on the diffuse Lambertian reflectance model, see Goral et al. (1984) or Cohen et al. (1986). In terms of PSP, only the scattering of light will be considered in the following. The propagation of light is computed for the entire scene and not only for the viewing direction of a potential observer like it is done by ray-tracing algorithms. A potential SI-effect might occur at surfaces which are invisible (hidden) for an observer but it might also affect other visible surfaces. From this reason, the complete illumination map of a scene is valuable for the correction of the SI-effect in PSP applications.
The radiosity algorithm is physically based on the conservation of energy. The total radiation in a scene is constant. The light that is not absorbed is reflected at the surface. Further simplifications and assumptions are given in Goral et al. (1984); Ashdown (1994) or Cohen and Wallace (1995). The total radiosity $B(x)$ of a surface element is defined as:

$$B(x) = E(x) + c_{\mathrm{r}}(x) \int_S B(x') \frac{1}{\pi d^2_{\mathrm{x,x'}}} cos\varphi_{\mathrm{x,x'}}\, cos\varphi_{\mathrm{x',x}} \cdot HID \cdot dA' \qquad (3.3.4)$$

where $E(x)$ is the sum of the intrinsic radiation at the surface element x, $B(x')$ is the sum of the reflected radiation from all other surface elements and the geometric term $cos\varphi_{\mathrm{x,x'}}\, cos\varphi_{\mathrm{x',x}} \cdot HID$ describes the occlusion problem. It ensures that only that parts of a scene contribute to the total radiosity which are not shielded by any obstacles. It is 1 if the visibility between the surface elements is not hidden, otherwise it is 0. The angle $cos\varphi$ is defined between the outward-facing surface normal and the direction from where the radiation propagates $\vec{d}_{\mathrm{x,x'}}$. The reflection coefficient c_{r} specifies the relationship between the absorbed and the reflected radiation as mentioned above. The decay of radiation with increasing distance between two surface elements is taken into account by the term $1/(d^2_{\mathrm{x,x'}})$. The geometrical form factor $F_{\mathrm{i,j}}$ is introduced in its differential form in order to simplify Equation 3.3.4. This results in:

$$F_{\mathrm{i,j}} = \frac{1}{A_{\mathrm{i}}} \int_{A_{\mathrm{i}}} \int_{A_{\mathrm{j}}} \frac{cos\varphi_{\mathrm{i,j}}\, cos\varphi_{\mathrm{j,i}}}{\pi d^2_{\mathrm{i,j}}} \cdot HID_{\mathrm{i,j}} \cdot dA_{\mathrm{j}} dA_{\mathrm{i}} \qquad (3.3.5)$$

as reported in Goral et al. (1984); Ashdown (1994) or Cohen and Wallace (1995). A form factor $F_{i,j}$ describes the geometric relationship between two differential surface elements i and j in a scene. The integral over the entire scene surface is decomposed into its sum over discrete surface elements (patches) for an analytical solution such as:

$$F_{\mathrm{i,j}} = \sum_{jn=1}^{n} \frac{cos\varphi_{\mathrm{i,jn}}\, cos\varphi_{\mathrm{jn,i}}}{\pi d^2_{\mathrm{i,jn}}} \cdot HID_{\mathrm{i,jn}} \cdot \Delta A_{\mathrm{jn}} \qquad (3.3.6)$$

applies. By doing so, Equ. 3.3.4 can be reformulated as:

$$B_{\mathrm{i}} = E_{\mathrm{i}} + c_{\mathrm{r,i}} \sum_{j=1}^{n} B_{\mathrm{j}} F_{\mathrm{i,j}}, \quad 1 \leq i \leq n \tag{3.3.7}$$

for its analytical solution. Here B_{i} represents the total radiosity per surface patch i as the sum of the intrinsic radiation E_{i} at the surface element and the reflected radiation of the remaining patches $\sum_{j=1}^{n} B_{\mathrm{j}} F_{\mathrm{i,j}}$. Equation 3.3.7 is finally written in matrix notation:

$$\underbrace{\begin{pmatrix} E_1 \\ E_2 \\ \vdots \\ E_{\mathrm{n}} \end{pmatrix}}_{\mathbf{E}} = \underbrace{\begin{pmatrix} 1-c_{\mathrm{r},1}F_{11} & -c_{\mathrm{r},1}F_{12} & \cdots & -c_{\mathrm{r},1}F_{1\mathrm{n}} \\ -c_{\mathrm{r},2}F_{21} & 1-c_{\mathrm{r},2}F_{22} & \cdots & -c_{\mathrm{r},2}F_{2\mathrm{n}} \\ \vdots & \vdots & \vdots & \vdots \\ -c_{\mathrm{r,n}}F_{\mathrm{n}1} & -c_{\mathrm{r,n}}F_{\mathrm{n}2} & \cdots & 1-c_{\mathrm{r,n}}F_{\mathrm{nn}} \end{pmatrix}}_{(\mathbf{I}-\mathbf{T})} \underbrace{\begin{pmatrix} B_1 \\ B_2 \\ \vdots \\ B_{\mathrm{n}} \end{pmatrix}}_{\mathbf{B}} \tag{3.3.8}$$

This particular system of equations can be solved with established analytical methods (e.g. Gauss-Seidel).

3.3.4. Radiosity implementation

A 2D scene is shown in Figure 3.8 that illustrates the meaning of the individual terms (e.g. form factor). The scene was discretized into N surface patches by means of a CFD mesh generator. The form factor between two patches is illustrated by means of a sender face ($i = 1...N$) at the position x (top right of the scene) and a receiver face ($j = 1...N,\ j \neq i$) at the position x' (bottom). Both patches have the absolute distance vector $|d_{12}|$ but different viewing direction vectors $\vec{V}$. The occlusion problem can be interpreted as a shadowed region by means of Figure 3.8. Patches which are visible from the sending face are marked in green, hidden ones are red.
Form factors which are senseless in terms of its physical meaning and its portions to the total radiation power can be excluded a-priori in order to avoid unnecessary calculations. Such patches might be located on an averted side with respect to the sending patch or they might be somehow covered by one or more overlying patches. This exclusion can be either done by using the directional property of Lambertian emitter which allowed no reflection of radiation for $cos\varphi \leq 0$. Furthermore, the z-buffer algorithm is often applied in order to solve the occlusion problem, compare Cohen and Wallace (1995) or Ashdown (1994).
A radiosity algorithm was implemented in *Matlab*™. Figure 3.9 shows the calculated total radiation B in a scene with two obstacles. The scene was discretized in about 5300 equidistant patches by a mesh generator. The illuminating element (emitter top right) was initialized with an intrinsic radiation of $E = 10$, whereas all the other elements had

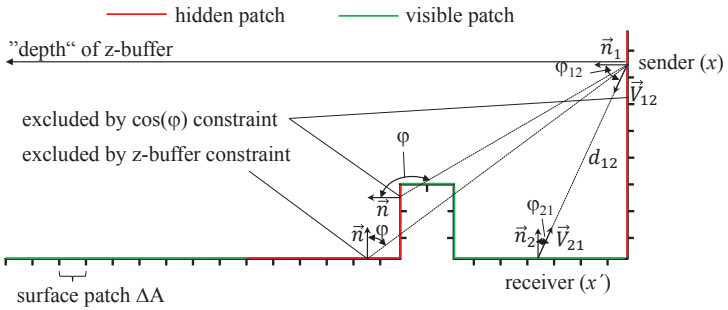

Fig. 3.8.: Illustration of a discretized occlusion-scene with its geometrical form factor(s) between a sender and a receiver patch; visible (*green*) and invisible (*red*) elements from the sender position are highlighted.

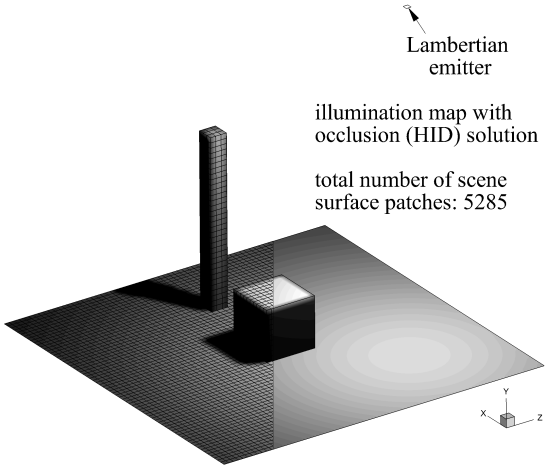

Fig. 3.9.: Simulated propagation of light from a diffuse Lambertian emitter (*top right*) calculated with the radiosity algorithm.

$E = 0$. The algorithm produced a physically meaningful solution in all areas (i.e. occlusion, the decay of intensity with increasing distance from the emitter, the superposition of light where surfaces intersect). The algorithm was applied in the following to correct the SI-effect from the experiments presented above. Initially, some conditioning of the experimental data was required. The experimental data was projected on a surface grid that represented a discretized geometry of the corner-experiment. The only parameter

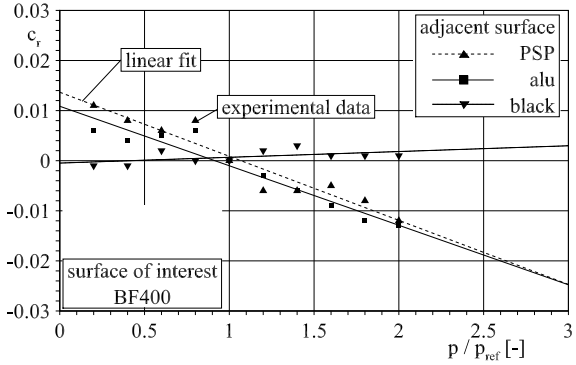

Fig. 3.10.: Pressure dependency of the absorption coefficient c_r for the three adjacent configurations (*symbols*) of the BF400-coated base plate; linear fit lines of the empirical absorption coefficients are included.

which was free to be varied and by which the radiosity solution could be controlled on the constraint of a steady state (with respect to illumination and geometry) was the radiation absorption coefficient c_r. The goal was to find values for c_r which finally produce a radiosity solution that had minimum deviations from the experimental data. The consideration of the intensity ratio change required a non-physical interpretation of the absorption coefficient: The radiosity in the vicinity of adjacent surfaces may increase or decrease depending on the pressure ratio. Hence, the loss of radiation energy must also be allowed. This slightly altered interpretation of the Lambertian model resulted in the fact that the absorption coefficient may not only have positive values between 0 and 1 but can also be negative. Finally, c_r was varied in the range of $-0.05 \leq c_\mathrm{r} \leq 0.05$ with $\Delta c_\mathrm{r} = 0.001$ for each calibration pressure.
Figure 3.10 displays the empirical c_r values (*symbols*) for the BF400 configurations. The scattered data were approximated by a linear fit. It can be seen that the reflection coefficient is nearly constant at $c_\mathrm{r} = 0$ for the black absorber paint. Its pressure-invariant slope confirms a good suppression of the SI-effect as it was already assumed from the first impressions. The other two configurations show a significant pressure dependency. The measured intensity distributions were finally corrected by means of the radiosity algorithm and the c_r values from the linear fits were applied.
For the correction, the actually measured intensity ratio was considered as the total radiation solution B. Hence, Equ. 3.3.7 must be reformulated in order to calculate the intrinsic radiation E without the superposition of the SI-effect. Figure 3.11 shows the comparison between the measured (*left sample half*) and the corrected intensity ratio

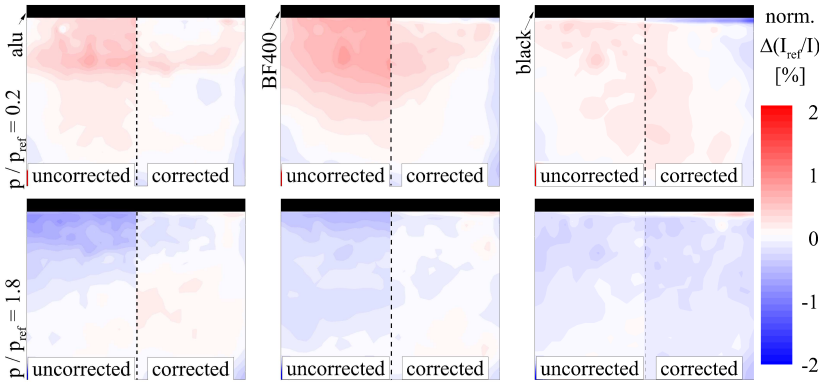

Fig. 3.11.: Comparison of the intensity change in the vicinity of a rectangular corner due to self-illumination; *Left sample half:* measured SI-effect; *Right sample half:* radiosity-corrected SI-effect; *Adjacent surfaces* (from left to right): frosted aluminum, BF400, absorber paint; pressure ratios: $p/p_{\mathrm{ref}} = 1-80\,\%$ (*top*) and $p/p_{\mathrm{ref}} = 1+80\,\%$ (*bottom*).

(*right sample half*) for the three configurations of the BF400 base plate. The pressure ratios are again $p/p_{\mathrm{ref}} = 1 \pm 0.8$.
It is obvious that the self-illumination can be reduced by 80 % in the vicinity of the intersection by means of the radiosity algorithm. However, it is also evident that the radiation propagation disobeys an ideal-diffuse propagation law as indicated by the remaining intensity pattern in the vicinity of the intersection. The comparison of the first two samples (PSP $\leftrightarrow$ aluminum and PSP $\leftrightarrow$ PSP) with the configuration PSP $\leftrightarrow$ black shows that self-illumination might be better suppressed by a black absorber coating. All surfaces that intersect with a PSP-coated area and which are not from interest during the PSP experiment should be covered with a black absorber paint. Nevertheless, it could be confirmed that the radiosity algorithm can be a possibility to correct the self-illumination effect on adjacent surfaces which are covered with a PSP coating.

3.4. Paint contamination

PSP coatings tend to absorb liquids and solved contaminations from the gas in the application surrounding as a consequence of the coating's permeable binder, compare Sakaue et al. (2006). Figure 3.12 shows the effect of a hydrophilic (*left*) and a hydrophobic binder (*right*) on a water droplet. Hydrophobic surfaces are characterized by a large

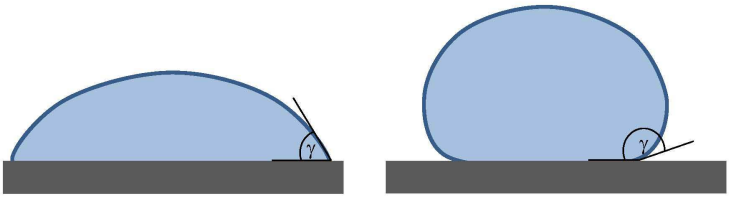

Fig. 3.12.: Water droplets on a hydrophilic (*left*) and on a hydrophobic surface (*right*).

contact angle γ but by a small affected area. Hence, a contamination typically influences the porosity of the PSP. This can cause cross-effects to the quenching and the diffusion time. This, in turn, can reduce the pressure sensitivity and the temporal resolution.
The following experiments assessed the impact of contaminations like oil droplets or carbon soot particles on the pressure sensitivity of a PSP coating and classified the order of magnitude of the measurement error. The experiments were carried out in the static calibration chamber. Two paint samples were coated with 20 μm of the binary PSP BF400. Each sample was split up into four quadrants: three quadrants were artificially contaminated with different intensities; the fourth was used as reference. A sudden pollution of the paint surface is simulated by this strategy.
Figure 3.13 shows the samples in an overall view on the left. The upper sample was polluted with a conventional, transparent salad oil. The lower sample was contaminated with powdered carbon particles which were dissolved in toluene in order to apply the contamination by a spray gun. The microscopic closeups aside display the different contamination levels. The images underneath show the binarized closeup which was used to estimate the degree of contamination. The contaminations emulated typical pollutions as they occur in the wind tunnel facilities at UniBwM. Oil droplets highly likely residue from the seeding particles of PIV measurements. Carbon soot particles imitate conventional dust.
Both samples were calibrated twice, clean and contaminated, at $T = 25\,^{\circ}\mathrm{C}$ in the range of $[10 \leq p_s \leq 160]\,\mathrm{kPa}$ with $\Delta p = 10\,\mathrm{kPa}$. The reference pressure was $p_{\mathrm{ref}} = 100\,\mathrm{kPa}$. The clean quadrant served as a reference for the determination of the systematic deviation between the two consecutive calibrations. The remaining experimental setup was the same like for a conventional PSP calibration, as introduced earlier.
Three topics were from major interest and should be answered with these experiments:

1. How is the contamination effect on the PSP pressure sensitivity and on the measurement accuracy?

2. Is it possible to compensate the contamination effect by means of a reference dye in a binary-PSP coating? How is the difference in these results compared with

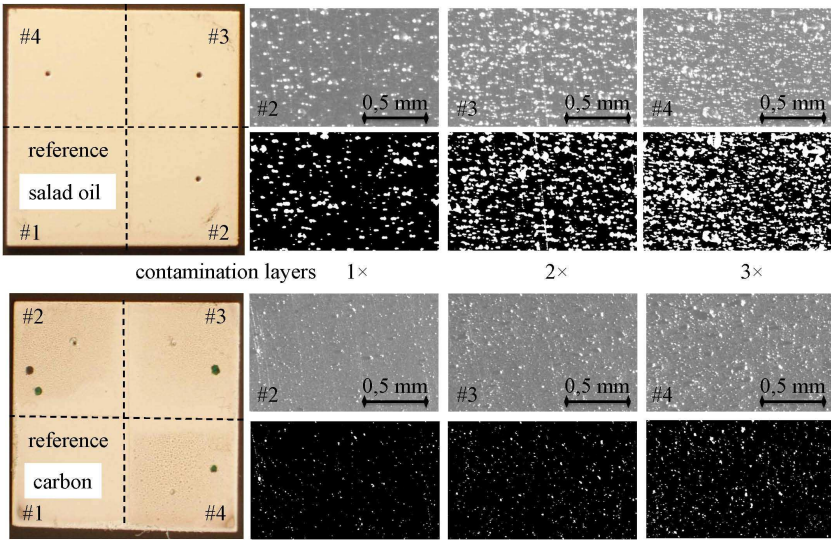

Fig. 3.13.: Macroscopic photograph of the contaminated sample with 3 contaminated quadrants of different contamination levels (*closeups*). The 4th reference quadrant was left blank; *Top:* salad oil contamination; *Bottom:* contamination with carbon soot particles.

the results from a uni-PSP?

3. Is it possible to minimize the impact of the contamination by an adept designation of the recording times for the PSP intensity images (wind-off prior wind-on or wind-on prior wind-off) and how is the remaining measurement uncertainty?

The intensity ratio I_{ref}/I is considered in the following in order to answer these questions. The reference and the pressure-sensitive dye in the BF400 were evaluated either isolated or combined in order to simulate a contamination of a uni-PSP or of a binary-PSP.
A continuously increased contamination during a wind tunnel run can obviously lead to a continuous change of the pressure sensitivity with time. The third item examined the question for the best moment to record the wind-off/wind-on intensity images from contaminated surfaces. A ratio indexed with clean./cont. simulated that the wind-off images were recorded from the clean PSP surface before the wind tunnel was started. An index cont./cont. means that the wind-off images were recorded from the contaminated surface after the wind tunnel was stopped. The wind-on images were recorded from the

contaminated surface in both cases. The classic calibration of the clean sample served as a reference for the calculation of the measurement uncertainty.
The specific evaluation schemes and sub routines were as follows:

1. averaging, image alignment and dark-frame subtraction for the intensity images of the pressure monitor $\overline{\mathbf{I}}_{\mathrm{p}}(p)$,

2. averaging, image alignment and dark-frame subtraction for the intensity images of the reference monitor $\overline{\mathbf{I}}_{\mathrm{r}}(p)$,

3. calculation of the normalized pressure intensity image by means of the reference image $I = \overline{\mathbf{I}}_{\mathrm{p}}(p)/\overline{\mathbf{I}}_{\mathrm{r}}(p)$,

4. calculation of the Stern-Volmer ratios which simulate the different image acquisition states:

   a) reference: $(I_{\mathrm{ref}}/I)_{\mathrm{clean/clean}} = I_{\mathrm{clean}}(100\,\mathrm{kPa})/I_{\mathrm{clean}}(p)$,

   b) clean / cont.: $(I_{\mathrm{ref}}/I)_{\mathrm{clean/cont.}} = I_{\mathrm{clean}}(100\,\mathrm{kPa})/I_{\mathrm{cont.}}(p)$,

   c) cont. / cont.: $(I_{\mathrm{ref}}/I)_{\mathrm{cont./cont.}} = I_{\mathrm{cont.}}(100\,\mathrm{kPa})/I_{\mathrm{cont.}}(p)$,

5. extraction of the representative intensities from a region of $50^2\,\mathrm{px}^2$ in the center of each quadrant,

6. calculation of the deviations between the clean reference calibration and the contaminated calibrations.

The results of the oil contamination are displayed in Figure 3.14 and the ones from the carbon pollution are shown in Figure 3.15. The upper part of the individual figures shows the Stern-Volmer plots. The lower part displays the intensity deviations of the different contamination levels from the clean reference case in percent. The different contamination levels are shown color-coded. The left- and right-hand-side compare the results from the binary- and the uni-PSP, respectively.
It can be seen that even a moderate contamination only has a small effect on the intensity ratio in the case of the oil-contaminated sample, no matter if the ratio $(I_{\mathrm{ref}}/I)_{\mathrm{clean/cont.}}$ or the ratio $(I_{\mathrm{ref}}/I)_{\mathrm{cont./cont.}}$ is considered. This effect is assumed to be mainly caused by the hydrophobic surface characteristic of the PSP. The droplets effectively cover a small area of the PSP coating. This leads to a reasonable small affection of the pressure sensitivity. The quencher can still diffuse into the binder and deactivate the luminophores. The transparency and stationarity of the droplet furthermore causes that the effect on the excitation and emission intensity could be widely reduced by the reference dye in the PSP coating. A deviation of 1-2 % from the clean reference calibration

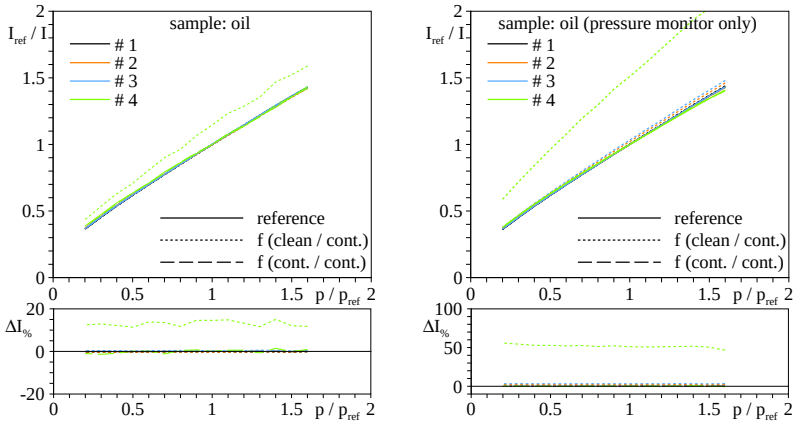

Fig. 3.14.: *Left:* Influence of the oil contamination on the intensity ratio using both the pressure and the reference probe and the isolated evaluation of the pressure probe (*right*); *Top:* Stern-Volmer plots; *Bottom:* difference in the individual ratios with respect to the clean reference ratio; the contamination levels of the individual quadrants are color-coded.

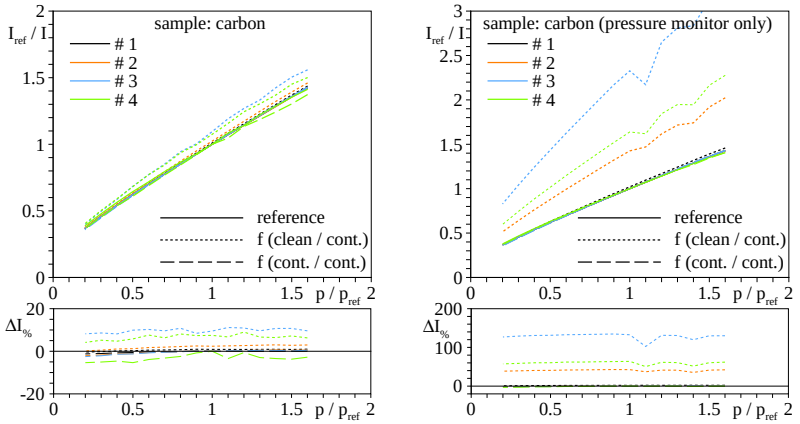

Fig. 3.15.: *Left:* Influence of the carbon contamination on the intensity ratio using both the pressure and the reference probe and the isolated evaluation of the pressure probe (*right*); *Top:* Stern-Volmer plots; *Bottom:* difference in the individual ratios with respect to the clean reference ratio; the contamination levels of the individual quadrants are color-coded.

followed for moderate oil contaminations if a binary-PSP can be used. Using a uni-PSP, the deviation slightly increases up to 3-5 %. The strong oil contamination (#4) led to the formation of a thin film on the PSP surface. This film caused the suppression of the gas diffusion and clearly affected the pressure sensitivity. Hence, a change in the intensity ratio by about 15 % (with respect to the clean reference case) is evident if the reference luminophore information is used. The isolated evaluation of the uni-PSP revealed a deviation by about 55 %.
The deviations in the intensity ratio for the carbon contamination instantly grow with increasing contamination level as expected. Macroscopic opaque soot particles deposited on the PSP surface and impeded the excitation of the luminophores. Microscopic particles penetrated into the porous binder and influenced the quenching process and hence the pressure sensitivity. The contamination effect is somehow compensated by the reference molecule. It resulted in deviations of up to 10 % for the binary-PSP. The deviations rise above 100 % for the isolated consideration of the pressure signal.
It should be noted that the individual contaminations did not lead to an increased pressure-sensitivity as indicated by the steeper slopes of the affected curves. This virtual increase aroused by the reduced intensities as a consequence of the contamination.
In general it can be stated from these experiments that the intensity ratio which is formed by means of clean and contaminated intensity images ($(I_{\mathrm{ref}}/I)_{\mathrm{clean/cont.}}$) is significantly affected from the contamination. The intensity ratio image clearly suffers from the local intensity drops as a consequence of the contamination. The removal of these areas from the final ratio image by appropriate image processing techniques might be possible but definitely introduces a residual measurement error.
If PSP experiments are carried out in facilities which suffer from moderate or strong contaminations, no matter if continuous or sudden pollutions, the wind-off intensity images should be recorded at similar contamination levels as the wind-on images immediately after the wind tunnel shut-down, as it was simulated by the ratios indexed with $(I_{\mathrm{ref}}/I)_{\mathrm{cont./cont.}}$. This approach can reduce the effect of the contamination but cannot suppress it. Advanced image processing strategies might help to further decrease the contamination effect.

3.5. Summary

Some dominant factors were examined that have the most significant impact on the PSP measurement accuracy under the conditions given at UniBwM (e.g. PSP coatings, wind tunnel infrastructure, equipment).
In order to compensate the PSP temperature effect, different strategies are typically followed: A one-component PSP in combination with a surface temperature sensor on the model surface is usually applied at low-speed conditions. A binary-PSP in combination with a thermoelectric element is preferentially used for transonic/high-speed PSP exper-

iments. CFD calculations are preformed in addition if the temperature dependency of a PSP is high (compare pc-PSP). The simulated surface temperature distribution can be used as an input for the data evaluation to correct the PSP temperature effect.
The investigation of a non-stationary illumination pattern as it can originate from relative motions between the model and the excitation (e.g. model motion, deformation, lamp vibration) showed that the synthetic motion of a homogenized intensity pattern of an LED excitation that is typically used at the department caused a change by about 0.16 % in the intensity ratio if the pattern is shifted not more than ± 10 px. A PSP with a pressure sensitivity of 76 %/ 100 kPa would suffer from an uncertainty of about 200 Pa as a consequence of this motion.
The self-illumination effect was classified by means of an experiment on a generic corner. It was shown that the error in the vicinity of the intersection of two adjacent surfaces ought to be in the range of ± 2 %. A semi-empirical approach was presented for the correction of the self-illumination effect based on a radiosity algorithm. The corrected results showed that the self-illumination effect could be reduced by 80 % by means of the algorithm. Anyhow, if a PSP measurment is performed in the vicinity of adjacent surfaces where only one surface is from interest, the spare surface should be coated with a diffuse black absorber paint in order to suppress the self-illumination effect.
The study of oil and carbon soot contaminants on PSP surfaces revealed the order of magnitude of a potential measurement uncertainty as a consequence of the contamination. However, these uncertainties are difficult to estimate and may vary from a few percent up to > 100 % depending on the contamination and its intensity. The use of a binary-PSP usually promotes the suppression of small local contaminations. If contaminations are present in the wind tunnel flow, the wind-off intensity images should be acquired at similar contamination stages as the wind-on images. This might be right prior to and after the wind tunnel shut-down. Anyway, unless wind tunnel facilities are affected by any contaminations, a carefull cleaning of the facility is mandatory before testing.

4. *IRES* - data reduction for PSP

4.1. Overview

The PSP measurement technique is mainly used at large aerospace research facilities in contrast to established optical measurement techniques such as PIV or LDV. This is one reason why mainly in-house solutions exist for PSP data evaluation. European evaluation solutions like *Topas* (DLR), *OMS* (TsAGI) or *Afix* (ONERA) are usually not sold commercially but sometimes provided within cooperations. Due to the comparably small number of PSP measurement systems at university and research departments, up to now only a few commercial providers of PSP systems established. *ISS Inc.* provides sale and development of PSP systems as well as evaluation routines based on *OMS*, see ISS Inc. (2013). The drawback of a black-box solution with its lack of adaptation opportunities to individual fluid-mechanical problems made this evaluation routine unsuitable for the experiments carried out at UniBwM. Therefore an own in-house solution named *IRES - Intensity Reduction & Evaluation Software* was developed as a proprietary image processing tool. It was designed for the analysis and conversion of digital intensity images into pressure and temperature distributions. Furthermore, it was specifically adapted to some fixed boundary conditions such as:

- the variety of problems – data evaluation should work for micro-fluidics as well as macroscopic low-speed, transonic and supersonic fluid-mechanical experiments,
- the measuring equipment – interoperability with available hard- and software,
- its usability – simple application of the tool by staff or students from the department,
- its expandability – numerous individual flow problems should by combined in one main routine including individual post-processing opportunities.

The efficient interaction between the given components of a PSP hard- and software system was from primary importance for the program design. Figure 4.1 illustrates the function of *IRES* as an interface between the specific system components. Existing recording systems should be used. They work reliably and ensure a synchronous data acquisition with a plurality of cameras and light sources as well as the simultaneous recording of sensor data of any kind. The program should process the data directly without reformatting in order to increase the evaluation efficiency. An interface for

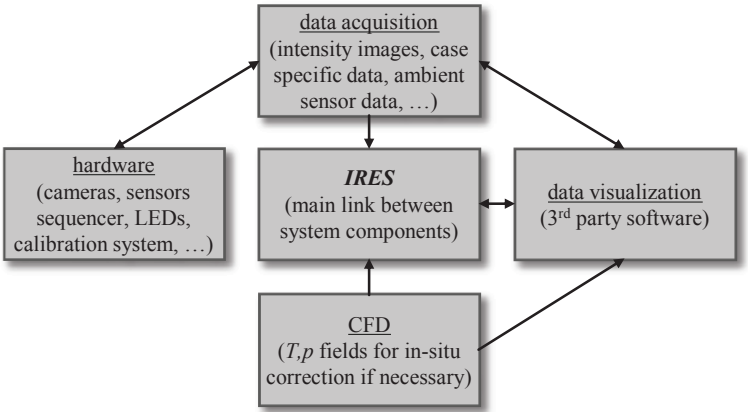

Fig. 4.1.: *IRES* as a link between the individual design constraints and systems.

CFD results should help to increase the measurement accuracy of the final pressure distribution (e.g. reduce the temperature effect by means of CFD surface temperature distributions). The output format should be compatible with common visualization tools (e.g. *Tecplot*™, *Ensight*™).
The tool should be able to perform state-of-the-art image alignment and data projection onto 3D grids by means of well defined marker distributions. The grid projection might be required because:

1. typically, two cameras are used for binary-PSP measurements at UniBwM. Hence, the signal can be recorded from (slightly) different viewing angles by each camera. Especially the intensity images from complex geometries have to be dewarped and aligned by means of intrinsic and extrinsic camera parameter (explanation follows below).

2. aerodynamic forces can cause a potential model deformation or a translation with respect to the wind-off state during the flow state. A calculation of the intensity ratio that does not account for these effects is simply wrong because it can establish correspondences between two points which are usually physically independent as it was examined in the previous chapter.

Hence, advanced data analysis techniques are typically applied for high precision PSP results. In the past, many approaches were presented that increased the accuracy of the intensity image alignment. An overview of the most conventional ways is summarized by Venkatakrishnan (2004). Shanmugasundaram and Samareh-Abolhassani (1995), Bell and McLachlan (1996) or Le Sant et al. (1997) introduced fundamental

works on alignment techniques based on image features. The features must be detected in both, the wind-off and the wind-on images. These features could be artificial markers (e.g. registration markers or pressure taps) or natural textures (e.g. intensity variations due to the illumination pattern or the luminophore concentration). The images are segmented into polyhedrons on behalf of the features and dewarped by means of affine transformations. Affine transformations require a large number of features for a high accuracy alignment especially for complex geometries. Further extensions to this alignment technique were presented by Liu et al. (2000), Le Sant et al. (2005) or Kuzub et al. (2011).
Sung et al. (2005) presented a correlation-based image alignment by means of standard PIV evaluation algorithms. The wind-off and wind-on intensity images were correlated and the resulting shift vector field was used for a reconstruction of the deformed or shifted intensity image. This comparably time-consuming method is able to produce high quality image alignments depending on the texture of the intensity image.
A common approach to reduce the data volume is the projection of the intensity image on a discretized surface grid of the model like it is used for CFD calculations. This method was introduced for PSP applications by Donovan et al. (1993) and extended by Bell and McLachlan (1996). It is based on the photogrammetry algorithms as they are applied in computer graphics. All standard operations for the calculation of the final pressure distribution (dark-frame subtraction, ratio calculation, averaging or filtering) are performed on the grid.
IRES uses a hybrid approach. The image alignment is performed in 2D by means of a camera calibration and a working grid. The working grid is created from a coarse input grid. Details of the implementation and the operation are discussed now.

4.2. Implementation

The basic functions of *IRES* are described on the basis of a PSP evaluation. The general procedure also applies to the evaluation of TSPs. For more information on the proper usage of the tool, the reader is referred to the user guide.
IRES was developed in *Matlab*™ using its functions and comfortable image processing toolboxes from the version R2012a. The flow chart in Figure 4.2 summarizes the tool and its main functions. Generally, *IRES* provides the possibility to process the intensity images of up to 10 pressure cameras (in the following denoted as red camera, with respect to the color of the luminescence signal) and 10 reference cameras (green camera). By this, 360 ° PSP measurements can be performed with high spatial resolution.
During the implementation, it was also focused on the use of the parallel-processing functionality. It raises the temporal efficiency during the evaluation of large amounts of data as they might origin from time-resolved measurements. It was additionally focused on the automation of the analysis. Input parameter files ensure an automated and

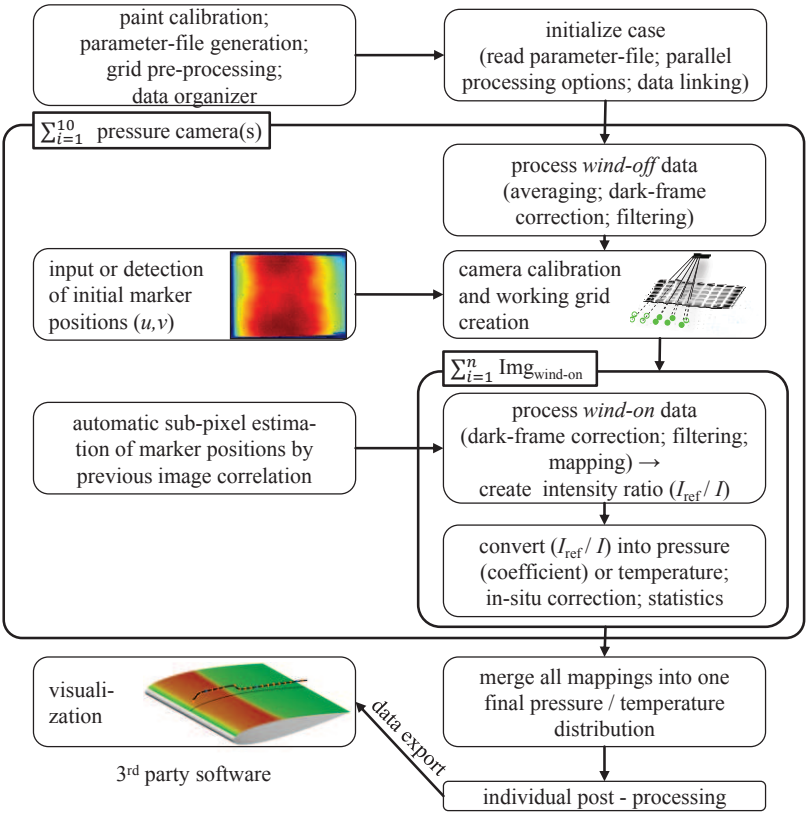

Fig. 4.2.: Flow chart for a PSP/TSP data evaluation with *IRES*.

reproducible evaluation. The index "wof" is used in the following if wind-off images are discussed (index "won" for wind-on images). All standard operations (e.g. dark-frame subtraction, averaging) are described in detail in Liu and Sullivan (2005) and are not discussed here.

Assuming that a PSP measurement is performed using a binary coating (red and green camera). The intensity is recorded at the wind-off and wind-on state. The image alignment is based on the red$_{wof}$ camera coordinate system. All remaining intensity images such as red$_{won}$, green$_{wof}$ and green$_{won}$ are mapped into the red$_{wof}$ camera system by means of individual camera calibrations and a working grid. The working grid has the same resolution of grid points as the red$_{wof}$ camera has pixel that carry PSP information (no background). The working grid must be created only once for each data set. The

projection approach has advantages and drawbacks. Three major advantages are:

- sub-pixel accurate image alignment for all intensity images of up to 10 camera sets,
- usage of simple two-dimensional image filter techniques which are constant for the entire ratio image,
- the possibility of the final usage of either the two-dimensional image information or the reduced data on a three-dimensional grid.

Three drawbacks are:

- creation of the working grid might be memory and time-consuming for images with very high resolutions (>10 Mpx),
- intensity image mapping from one camera to another can be time-consuming,
- the interpolation during the image alignment from one camera to another might slightly affect the data (smoothing or noise increase).

After all involved images were mapped into the red_{wof} system, the calculation of the intensity ratio and the pressure conversion follows. The final results can be post-processed by means of individually adapted functions (e.g. integration of pressures in order to calculate forces or spectral analysis). The operational background of fundamental *IRES* subroutines is explained below.

4.2.1. Input files

IRES requires a specific folder structure and some basic input files. The folder structure can be found in Appendix B. Furthermore, seven input files are mandatory for a successful *IRES* evaluation. The file "case-name.set" is used to set the paths and for establishing the internal case variables. The name of this file should contain relevant test parameters.
The parameter file named "Parafile_case-name.dat" ensures the automatic evaluation. It contains relevant evaluation presets. An exemplary parameter file is discussed in detail in Appendix B.
A surface grid file called "case-name_InputGrid.dat" is required that includes a discretized surface in the ASCII format. This grid serves as the basis for the generation of the working grid (explanation follows below) and it carries the surface pressure mapping for visualization if desired. The entire surface grid must consist either of triangles or rectangles, a hybrid mesh is not allowed. It can be created with any CFD mesh generator. So far, *Gambit*™ surface meshes are supported which were converted into the ASCII-hypermesh format by *TGRID*™.

Four files are mandatory that contain the environmental conditions during the experiments for each recorded image. The files "wind-off_pressure_Pa.dat" and "wind-off_temperature_K.dat" contain the ambient static pressure in Pascal and the static model temperature in Kelvin for each wind-off image. The same applies for the wind-on files "wind-on_pressure_Pa.dat" and "wind-on_temperature_K.dat". The *temperature* files remain empty if a surface temperature distribution was available from TSP, CFD or IR data (plug-in for CFD and IR not yet implemented).
The in-situ correction of the PSP results is applied by means of the "tap_pressures_Pa.dat" file. It contains an $m \times n$ matrix with n static pressure readings from the model in Pascal for m wind-on intensity images.

4.2.2. Marker detection

Image registration markers on the model surface are mandatory for an *IRES* evaluation because the individual camera calibrations are calculated from the correspondences between the image marker positions and their geometric positions on the model. Dark, round spots with an imaged diameter of about 10 px are particularly suited as registration markers. The markers should be distributed randomly over the model whereas the region-of-interest should be surrounded by the markers. Their geometric positions must be well known in any case. For a planar test geometry, at least four markers are required. In the case of a complex geometry, at least six registration markers must be noticeable for each camera.
IRES has an implemented marker detection routine that allows the linking between the markers in the image and their geometric positions. The user has to identify the coarse marker position in the first intensity images of each involved camera. The detection in the successive images is done automatically. *IRES* calculates the precise sub-pixel positions of each marker from the coarsely picked positions. Therefore, the intensity image is segmented. The size of the segmented image can be defined by the "marker search radius". Several algorithms can be selected for the determination of the marker positions. They provide different accuracy levels according to the quality of the intensity images. The centroid algorithm can be the best choice for markers which appear perspectively distorted or that are close to edges. The segmented image is separated into fore- and background informations by means of an intensity threshold. The centroid of the segmented foreground information is calculated by means of standard *Matlab*™ functionality. The centroids position is subsequently used as the sub-pixel precise marker position. The segmentation into fore- and background and hence the calculation of the centroid is affected by image noise. Hence, the estimated position of the same marker may vary by some tenths of a pixel in noisy subsequent images.
A much more precise marker position estimation can be performed by means of a cross-correlation of the segmented image with an artificial marker. The intensity profile of the

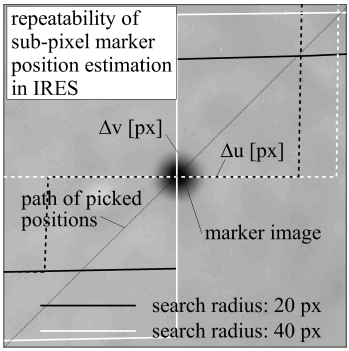

Fig. 4.3.: Repeatability of the detected marker position for various picked positions (*diagonal line*) for changing marker search radii (*black and white lines*). The horizontal (*dashed*) and vertical deviations (*solid*) between the detected and the original marker position are outlined.

artificial markers is either Gaussian or top-hat. The shape (e.g. orientation or stretching) is estimated by an initial fore- and background segmentation. The shape parameters are used as an input for the generation of the artificial marker. The sub-pixel accurate determination of the marker position from the 2D cross-correlation plane works similar to a PIV evaluation according to Equ. 2.2.16.
Figure 4.3 proves the reliability and repeatability of the correlation-based marker detection for various coarsely picked positions (*diagonal line*). The results are displayed for varying marker search radii. The calculated positions must be independent from the picked position in order to ensure a safe and reliable marker determination in an automatic evaluation of subsequent (potentially moving) PSP images. The high accuracy requirements are mandatory for a precise camera calibration which is the basis for the creation of the working grid and the image alignment.

4.2.3. Working grid

IRES requires a working grid for the sub-pixel accurate mapping of all intensity images from every camera into the red_{wof} reference camera system at full image resolution. The image alignment as it was implemented in *IRES* implies the procedure sketched in Figure 4.4:

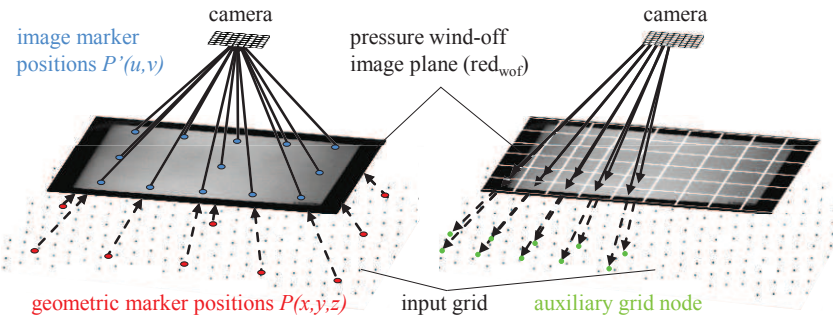

Fig. 4.4.: Schematic of the working grid creation in *IRES*; *Left:* camera calibration based on the model markers and the coarse input grid; *Right:* creation of the working grid (*green*) with the red_{wof} camera resolution by applying the camera calibration for each pixel.

1. A specific calibration as given by the relations 4.2.1 and 4.2.2 must be performed for each camera in order to calculate the intrinsic and extrinsic camera parameter as a basis for the image mapping from one camera into another. The camera calibration is performed by means of the wind-off intensity image, the geometric (*red*) and image marker positions (*blue*), compare schematic on the left in Figure 4.4.

2. An auxiliary grid (working grid) is created by means of the wind-off intensity image and the calibration of the reference camera system as well as the input grid. The working grid has the same number of nodes (*green*) as the reference camera has pixels, whereas pixels with background informations (no PSP) are skipped, compare right in Figure 4.4.

$$\underbrace{\begin{pmatrix} u \cdot s_c \\ v \cdot s_c \\ s_c \end{pmatrix}}_{\text{image coordinates } P'} = \underbrace{\begin{pmatrix} L_1 & L_2 & L_3 & L_4 \\ L_5 & L_6 & L_7 & L_8 \\ L_9 & L_{10} & L_{11} & L_{12} \end{pmatrix}}_{\text{transformation matrix } \mathbf{L}} \cdot \underbrace{\begin{pmatrix} x \\ y \\ z \\ 1 \end{pmatrix}}_{\text{world coordinates } P} \tag{4.2.1}$$

$$\begin{aligned} u &= \frac{L_1 x + L_2 y + L_3 z + L_4}{L_9 x + L_{10} y + L_{11} z + L_{12}} \\ v &= \frac{L_5 x + L_6 y + L_7 z + L_8}{L_9 x + L_{10} y + L_{11} z + L_{12}} \end{aligned} \tag{4.2.2}$$

The camera calibration is based on the pin-hole camera model, as proposed by Tsai (1986). The basic relation that links the image points $P'(u,v)$ and the geometric coordinates $P(x,y,z)$ is given in Equ. 4.2.1 and 4.2.2 whereas the coefficients of the transformation matrix L describe the camera calibration, see Azad et al. (2009). From the coefficients, the intrinsic (e.g. focal length or principle point) and extrinsic camera parameter (orientation and position) can be calculated. The specific relations for the conversion are given in Appendix B in Equ. B.0.1 and B.0.2. A set of pseudo-code algorithms describes the calibration procedure and the creation of the working grid. The algorithms are also attached in Appendix B.
The transformation coefficients L in Equ. 4.2.1 can be calculated by means of $n \geq 6$ marker correspondences using Algorithm 1. The working grid is generated from the knowledge of the camera calibration and a raw camera image in the red_{wof} system by means of Algorithm 3. The remaining intensity images are mapped from their specific cameras onto the reference image by means of the created working grid and the Algorithms 2, 4 and 5. For a high-accuracy image alignment, a precise camera calibration is required. This, in turn, premises an accurate determination of the marker positions in the individual intensity images. It finally clarifies the effort that was put into the precise marker determination at the beginning of this section.

4.2.4. Pressures conversion

A bi-square fitting function of the form:

$$\left(\frac{I_{\text{ref}}}{I}\right) = A + B \cdot T + C \cdot \left(\frac{p}{p_{\text{ref}}}\right) + D \cdot T^2 + E \cdot \left(\frac{p}{p_{\text{ref}}}\right) \cdot T + F \cdot \left(\frac{p}{p_{\text{ref}}}\right)^2 \quad (4.2.3)$$

was implemented in *IRES*. Equ. 4.2.3 is solved for pressure or temperature in case of a PSP or a TSP evaluation, respectively. The coefficients $A...F$ are paint characteristics which can be determined in a calibration chamber or by an in-situ calibration. The temperature information for the compensation of the temperature effect in a PSP measurement either comes from a temperature sensor, TSP/ IR data or a CFD calculation.

4.3. Validation

The accuracy of the calculated intensity ratio is examined by means of synthetic images which emulate a transient measurement series. Two image series (500 images each) were generated that simulate the major impact factors on the ratio accuracy. One data set was created with different image qualities (noise levels) that can affect the precise marker determination. State-of-the-art CCD and CMOS cameras can have typical noise levels between $[0.1 \leq \sigma_{\text{N}} \leq 5]\,\%$. The second image set emulated a shift between the

wind-off and the wind-on images as a consequence of a potential model motion (or aero-elastic deformation) which might be resolved in a transient image series. The images were further defined by:

- The size was $512^2\,\mathrm{px}^2$;,
- The individual image consisted of a flat-field part and a superimposed Gaussian white noise;
- The wind-on/wind-off flat-field ratio was 1;
- Six registration markers were included in order to map the images on a generic surface;
- Set 1: The noise level was varied between $[0.1 \leq \sigma_\mathrm{N} \leq 5]\,\%$;
- Set 2: A model motion was simulated while a continuous sinusoidal shift around the image center with $[1 \leq r \leq 10]\,\%$ was applied to each image. The images were finally superimposed with 1 % white Gaussian noise.

The intensity ratio from the individual images was calculated in *IRES* whereas no image filtering was applied. The individual ratio images were subsequently averaged in order to evaluate the noise level with respect to the number of averaged ratio images. The averaged intensity ratio for every loop was evaluated in a rectangular box of $6^2\,\mathrm{px}^2$ close to the image center. Within the box the mean μ and the standard deviation σ which define the signal-noise-ratio $SNR = \mu/\sigma$ were calculated for the intensity ratio.
The results of the noise study are shown in Fig. 4.5. The left-hand side shows a semi-logarithmic plot of the SNR with respect to the image number for various noise levels (*symbols*). The SNR increases as expected with $SNR \propto 1/\sqrt{N_\mathrm{Img}}$. The right-hand side presents the residual noise portion $1/N \cdot \sum(I_N/I_0 - 1) \cdot 100\,\%$ that is finally present in the averaged ratio by knowing that the exact ratio should be 1. The noise residuum is a direct measure for the accuracy of the raw (unfiltered) intensity ratio.
Images with a noise level of 1 % finally produce a noise level of about 0.2 % in the individual intensity ratio. As expected, an increased number of samples further decreased the noise level below 0.003 % after averaging 500 intensity ratios.
The spatial filtering of the intensity ratio is mandatory in PSP applications in order to reduce the residual noise. The data set which was superimposed with 1 % noise was re-evaluated with an activated image filtering of size $6^2\,\mathrm{px}^2$. The residuals are included in the right figure, as indicated by the hollow triangles. It was shown that the filtering can decrease the residual noise by a factor of 10 down to 0.032 % for a single evaluated image pair.
A noise level of 5 % which is present in the raw intensity images produced a residual noise level of about 1 % in the processed intensity ratio if only one image is evaluated. A significant higher number of ratio images must be averaged in order to get comparable results as for the 1 % noise level. This is mainly caused by

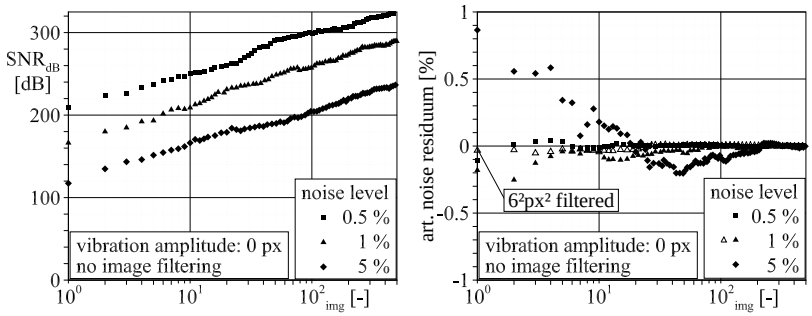

Fig. 4.5.: *Left:* signal-to-noise ratio [dB] in the final intensity ratio for various raw image noise levels evaluated with *IRES*; *Right:* residuum of the remaining noise level with respect to different raw image noise levels while averaging 500 intensity ratio images.

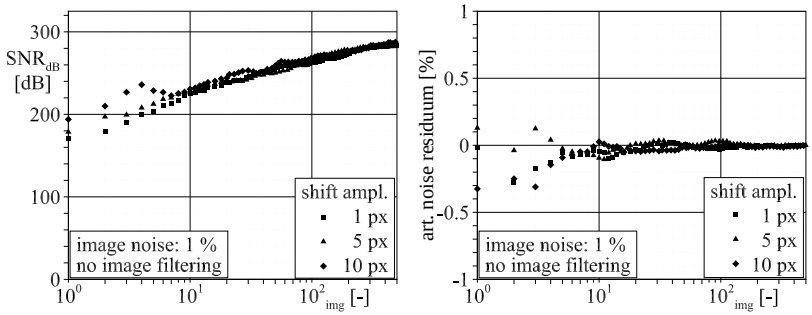

Fig. 4.6.: *Left:* signal-to-noise ratio [dB] in the final intensity ratio for various model motion amplitudes evaluated with *IRES*; *Right:* residuum of the remaining noise level with respect to different model motion amplitudes while averaging 500 intensity ratio images, from Bitter et al. (2012).

a slight variation in the estimated marker location due to the image noise. As a consequence, the camera calibrations of the individual images were slightly different. This directly affected the image alignment.

The results for the data set that emulated the synthetic model motion are displayed in a similar manner in Fig. 4.6. The SNR (*left*) remains almost unaffected from the model motion amplitude if more than 7 images are averaged. As shown on the right, a single unfiltered ratio image has a residual noise level of about $\pm 0.3\,\%$ at its maximum. From 7 images on, the residual noise level drops down significantly and is nearly not affected

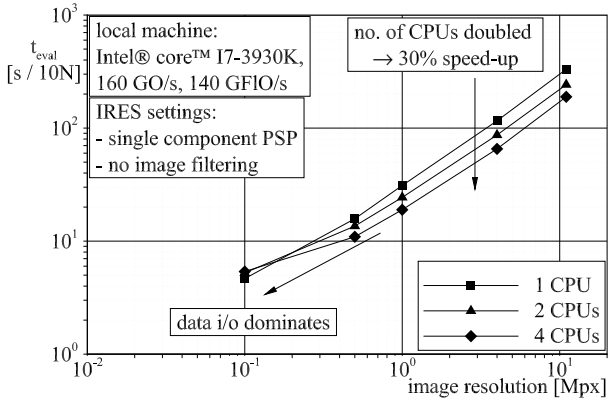

Fig. 4.7.: Computation performance with respect to the intensity image resolution using the single and parallel CPU evaluation options in *IRES*; evaluation performed on an *Intel I7*™ dual quad-core CPU.

by any model motion amplitude.
It can be summarized that intensity ratios from wind-off/wind-on intensity images that:

- have a moderate noise level of about 1 %,
- showed model motions or deformations from ≤ 10 px,
- were finally smoothed by an appropriate gradient-preserving image filter

can be evaluated with an accuracy of about 0.04 %. With a pressure sensitivity of 76 %/ 100 kPa this would result in an uncertainty of about 50 Pa in the individual filtered ratio image as a consequence from the mapping procedure within *IRES*. A significant decrease of the uncertainty down to about 0.006 % (or 8 Pa) in the final ratio image is possible if more than 7 ratio images were averaged.
Finally, the evaluation time was benchmarked by means of synthetic intensity images of varying resolution. They were processed using the parallel-processing option. The image resolutions varied between 0.1 Mpx and 11 Mpx (*pco.4000*). The evaluation included the image filtering, an in-situ correction and the data projection on the 3D grid. The results are presented in Figure 4.7. If the *Intel I7*™ dual quad-core CPU architecture is used (140 G(Fl)O/ s) a doubling of the CPU number resulted in a 30 % speed-up for images with resolutions ≥ 0.5 Mpx. The processing of 10 intensity images with the highest resolution took about 130 s on four parallel CPUs. If the image resolution is smaller, the data-i/o dominated the image processing and the benefit of the parallel-processing option vanished.

4.4. Summary

The PSP data processing tool *IRES* which was developed at UniBwM was introduced within this chapter. The basic functionality was discussed whereas the precise marker determination and the image alignment were focused.
The processing of two synthetic images series that emulated different image qualities or potential model motions validated the performance of *IRES* with respect to the evaluation of transient PSP image series. It was shown that the final image alignment and, hence, the intensity ratio is dependent on the quality of the raw intensity images. If the intensity images contain noise levels up to 1 % and the model motion amplitudes are below 10 px an individual filtered pressure image contains a residual uncertainty of about 50 Pascal as a consequence from the mapping process in *IRES*. This residual was significantly decreased by means of image averaging for more than seven intensity images.
The evaluation performance of the program was assessed on a state-of-the-art desktop PC using the implemented parallel-processing option in *IRES*. A doubling of the CPU number resulted in a 30 % speed-up for high-resolution intensity images.

5. Benchmark of the PSP system

5.1. Wind tunnel facilities

5.1.1. Trisonic wind tunnel Munich

The trisonic wind tunnel (TWM) at UniBwM is a blow-down wind tunnel. Its subsystems are sketched in Figure 5.1. Air is taken from the atmosphere, dried, compressed to 2 MPa and stored in two vessels (2) - each having a volume of 190 m^3. The filling of the storage vessels from ambient pressure takes about 1.5 hours with 3 compressors (1). The compressed gas is led through a feed line with safety devices into the wind tunnel facility for operation. The mass flow is controlled by a hydraulic piston valve located at position *a*. The total pressure in the facility can be adjusted in the range of $p_t = [120 \ldots 500]$ kPa by means of this control unit. The accuracy of the pressure

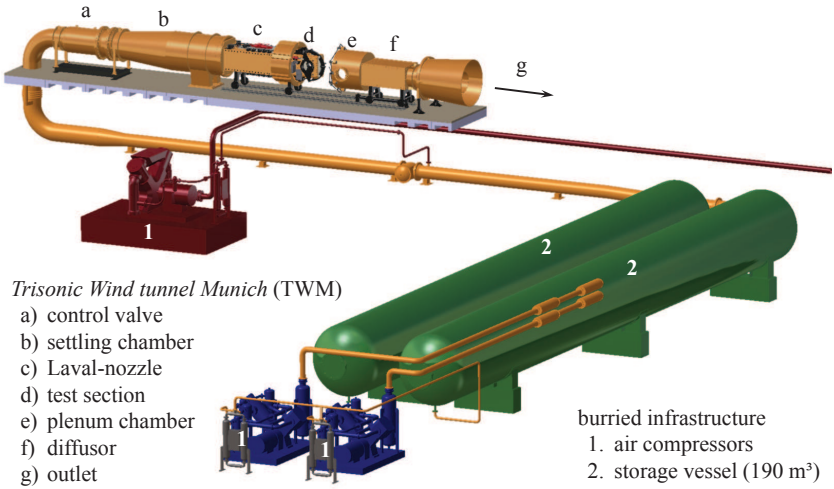

Fig. 5.1.: Sub systems of the trisonic wind tunnel Munich (TWM).

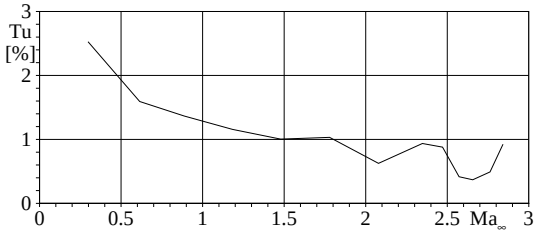

Fig. 5.2.: Turbulence level of the TWM with respect to the flow Mach number at unit-Reynolds numbers around $1.5 \cdot 10^6\,\mathrm{m}^{-1}$.

adjustment is 0.5 kPa. Unit-Reynolds numbers from $\mathrm{Re} = [7 \ldots 80] \cdot 10^6\,\mathrm{m}^{-1}$ are possible as a consequence of the total pressure variation. Tracer particles for PIV investigations can be introduced at the position of the control valve while using the strong turbulence for their mixing with the flow at this position. The flow is further led through the settling chamber with flow straighteners (*b*) before it passes the Laval nozzle (*c*). The nozzle allows a continuous adjustment of the flow Mach number in the range of $\mathrm{M}_\infty = [0.3 \ldots 3.0]$. The setting accuracy is $\Delta\mathrm{M}_\infty = 0.005$. The maximum wind tunnel run time with full storage vessels at the lowest total pressure in the test section is about 300 s at $\mathrm{M}_\infty = 3.0$. The maximum flow rate is about 240 kg/ s at $p_{\mathrm{t,max}}$ and $\mathrm{M}_\infty = 1.0$. Here, the maximum run time for measurements is about 40 s.
The test section (*d*) has a rectangular cross section and a measurement volume of about $[1{,}200^{\mathrm{L}} \times 300^{\mathrm{W}} \times 675^{\mathrm{H}}]\,\mathrm{mm}^3$. There are various optical accessibilities to the test section from both sides and from the top. The test section can be equipped with perforated walls in order to avoid blockage effects of larger models. Models can be mounted either using guiding slots in the side walls or via a rear sting mount. The angle of attack can be adjusted contentiously in both cases between $[-5 \leq \alpha \leq 25]^\circ$. The test section is surrounded by a plenum chamber (*e*). The minimum optical path for an optical observation of the flow from the inside of the plenum chamber is about 0.3 m. From the outside this distance is not shorter than about 1.4 m. The flow finally passes the diffuser (*f*) that re-compresses the gas before it is guided back to the atmosphere (*g*).

Wind tunnel characteristics

The wind tunnel turbulence level was assessed for different flow Mach numbers by means of PIV as shown in Fig. 5.2. The turbulence level is around 1.5-2.5 % at subsonic conditions and decreases down to 0.5 % at supersonic conditions.

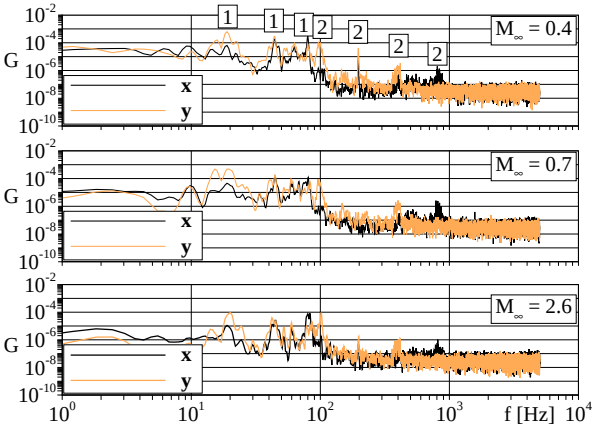

Fig. 5.3.: Axial (*black*) and horizontal (*orange*) vibration power spectra of the TWM facility at Mach numbers $M_\infty = [0.4;\ 0.7;\ 2.6]$ (from top to bottom). Two dominant frequencies at $f \approx [20;\ 100]$ Hz originated from the hydraulic control valve.

High flow rates cause vibrations of the entire facility. In order to identify specific characteristics and separate them from potential dominant flow features, the vibration spectrum of the facility was investigated. A marker at one of the side walls was tracked using a high-speed camera with a recording rate of $f_s = 10$ kHz. The camera was isolated from the surrounding and stored in a special air-cushioned system. Figure 5.3 shows the axial (x) and horizontal (y) power spectral density G of the marker at different sub- and supersonic flow Mach numbers. Two dominant frequencies at $f \approx [20; 100]$ Hz and their higher harmonic portions can be examined from the plot. It is assumed that these vibrations are mainly caused by the hydraulic flow control valve.

5.1.2. Open-jet wind tunnel

Beside an Eiffel wind tunnel, an open-jet wind tunnel as schematically shown in Fig. 5.4 is available for low-speed investigations at UniBwM. The facility can be equipped with two individual nozzles with exit diameters of $D = [170; 370]$ mm. The wind tunnel is continuously driven by a 2.4 kW radial fan that produces a maximum total pressure change of about 980 Pa. Hence, flow speeds up to 60 m/s can be reached at the exit of the smaller nozzle.

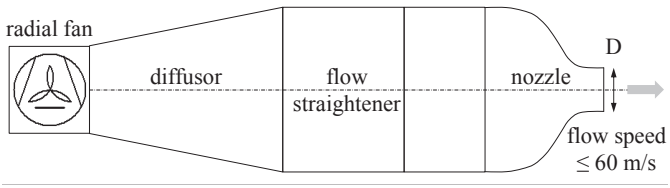

Fig. 5.4.: Schematic of the open-jet wind tunnel at UniBwM. Flow speeds up to 60 m/s can be reached with interchangeable nozzles.

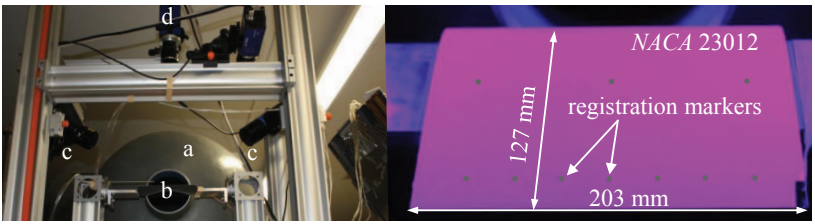

Fig. 5.5.: Experimental setup at the open-jet wind tunnel (a) for the low-speed PSP validation experiments on a *NACA* 23012 airfoil (b); 405 nm LED excitation (c) and camera with signal filter (d), from Bitter and Kähler (2011).

5.2. PSP at low-speed conditions

5.2.1. Experimental setup

The validation experiments for the PSP system at low-speed conditions were conducted using a *NACA* 23012 airfoil in the open-jet wind tunnel. The experimental setup is shown in Figure 5.5. The airfoil (*b*) was made from steel and had dimensions of $c = 127\,\text{mm}$ chord length and $b = 203\,\text{mm}$ span ($\Lambda = b^2/S = 1.5$). The airfoil was mounted about 50 mm away from the nozzle exit. It was positioned in the center of the nozzle so that the airfoil protruded some centimeters beyond the nozzle diameter. The rigid construction of the setup and low aerodynamic forces completely suppressed model motion or deformation during the experiments.
The following model painting procedure was applied: A white diffuse screen layer from a conventional base coat was applied to the cleaned model surface in order to compensate some surface inhomogeneities and to increase the SNR. 20 image registration markers were positioned on this coating using a rotating waterproof pen in a 3-axis CNC machine. By this procedure, the markers were precisely applied with a position-

ing accuracy of 0.05 mm. The airfoil was coated with the uni-PSP (UF400) after the marker application. Hence, the markers remained clearly visible in the individual intensity image but completely vanished in the intensity ratio. No affection of the PSP layer was ascertained from the waterproof pen even some weeks after testing. The total layer thickness was approximately $35-40\,\mu$m (measured with a *Quanix 1500*).
The excitation of the PSP layer was done using two pulsed 405 nm high-power LEDs, as highlighted in Fig. 5.5. They were mounted about 350 mm away from the model. The LEDs produced an optical power of about 3 W in pulsed mode operation (frequency: $f_{\mathrm{LED}} = 250\,$Hz, pulse duration: $t_{\mathrm{p}} = 220\,\mu$s). The LEDs only flashed during the image recording in order to preserve the paint from aging.
A 14 bit *pco.4000* CCD camera (*d*) with sensor dimensions of $4{,}008 \times 2{,}672\,\mathrm{px}^2$ (11 Mpx) was used for the image recording. It was mounted perpendicular to the flow vector ahead the suction side of the airfoil at a distance of 370 mm. A 570 nm long-pass interference filter (transmission $> 95\,\%$, optical density $OD > 6$) was installed between the camera and the *Zeiss* Makro-Planar T*2 / 50 mm lens in order to avoid a potential filter leakage, see Gongora-Orozco et al. (2009). The spatial resolution with the optical components was about 11.5 px/mm at an angle of attack $\alpha = 12^\circ$. This corresponds to an optical magnification of $M \approx 1:9$. The camera intergration time was $t_{\mathrm{i}} = 900\,$ms in order to have a luminescence intensity level close to the full-well capacity of the camera ($\approx 15{,}000\,$cts).
This experimental setup was chosen in order to emulate the spatial dimensions at the TWM test section where similar validation experiments were conducted under high-speed conditions (next section). This approach should ensure a better comparability of the uncertainty analysis from both test series.

5.2.2. Methodology

The experiments were conducted at various flow speeds at changing angles of attack α. The individual test cases are summarized in Table 5.1. The angle of attack was adjusted from the resting position at $\alpha = 0^\circ$ after the wind tunnel was started in order to avoid a potential flow separation. The wind tunnel already run 10 minutes before the recording of the intensity images was started in order to allow a homogenization of the surface temperature. A pt100 surface temperature sensor was attached to the model for the compensation of the PSP temperature effect. Its values were recorded for each individual image with an accuracy of 0.1 K. Seven intensity images as well as dark images were recorded at the wind-on and wind-off states. The wind-off images were recorded directly after the wind tunnel was stopped shortly after the acquisition of the wind-on images. The airfoil was equipped with static pressure taps. Three ports on the suction side were selected in order to use their readings for the in-situ correction of

quantity	change parameters (flow speed variation)		
open jet velocity U_∞ [m / s]	20	40	60
dynamic pressure q_∞ [Pa]	225.2	900.9	2,027.2
angle of attack α [°]	[12; 20]	12	[12; 20; 24; 28]
Reynolds number $\mathrm{Re_c}[\cdot 1000]$	160	320	480
ambient pressure p_∞ [Pa]	95,200		
ambient temperature T_∞ [°C]	25.2		
model temperature T_s [°C]	25.1		
magnification M [1]	1 : 9		
eff. pixel array $w \times h$ [px^2]	$2{,}300 \times 1{,}400$		
integration time t_i [ms]	900		
optic	*Zeiss* Makro-Planar T* 2 / 50 mm		

Tab. 5.1.: Flow conditions and acquisition parameter for the *NACA* 23012 low-speed PSP experiments in the open-jet wind tunnel.

the PSP results. Seven more ports were used for a comparison of the raw PSP results with the tap readings. This procedure should give an estimation of the measurement uncertainty. The pressure measurements at the static ports were conducted using a *ScaniValve* pressure scanning device. The sensor was able to resolve steady state static pressures in the range of $[-7 \leq p_\mathrm{s} \leq 7]$ kPa. The sensor voltage values were integrated over 2 s, averaged and finally converted into pressures by means of a linear calibration fit. Due to the long integration time, the static pressure taps were only read out once during the test series. It was assumed that the values did not change with time during the test series.

5.2.3. Results

Figure 5.6 shows the ensemble-averaged distributions of the pressure coefficient $-\overline{c_\mathrm{p}}$ on the suction side of the airfoil for varying flow speeds $U_\infty = [20; 40; 60]$ m/s (from top to bottom) at $\alpha = 12°$. In Figure 5.7 the corresponding pressure distributions for varying angles of attack $\alpha = [20; 24; 28]°$ (from top to bottom) at a constant flow speed of $U_\infty = 60$ m/s are displayed. The readings from the conventional *ScaniValve* measurements are included (*symbols*) for the comparison with the PSP results. The ports which have been used for the in-situ correction are highlighted by the blue symbols.
Strong 3D flow effects occurred as a consequence of the experimental setup as indicated by the topology of the individual pressure distributions. For a reliable comparison of the PSP data with the pressure tap readings, the PSP data was extracted from the vicinity of the scattered pressure taps at the position of the black trace.

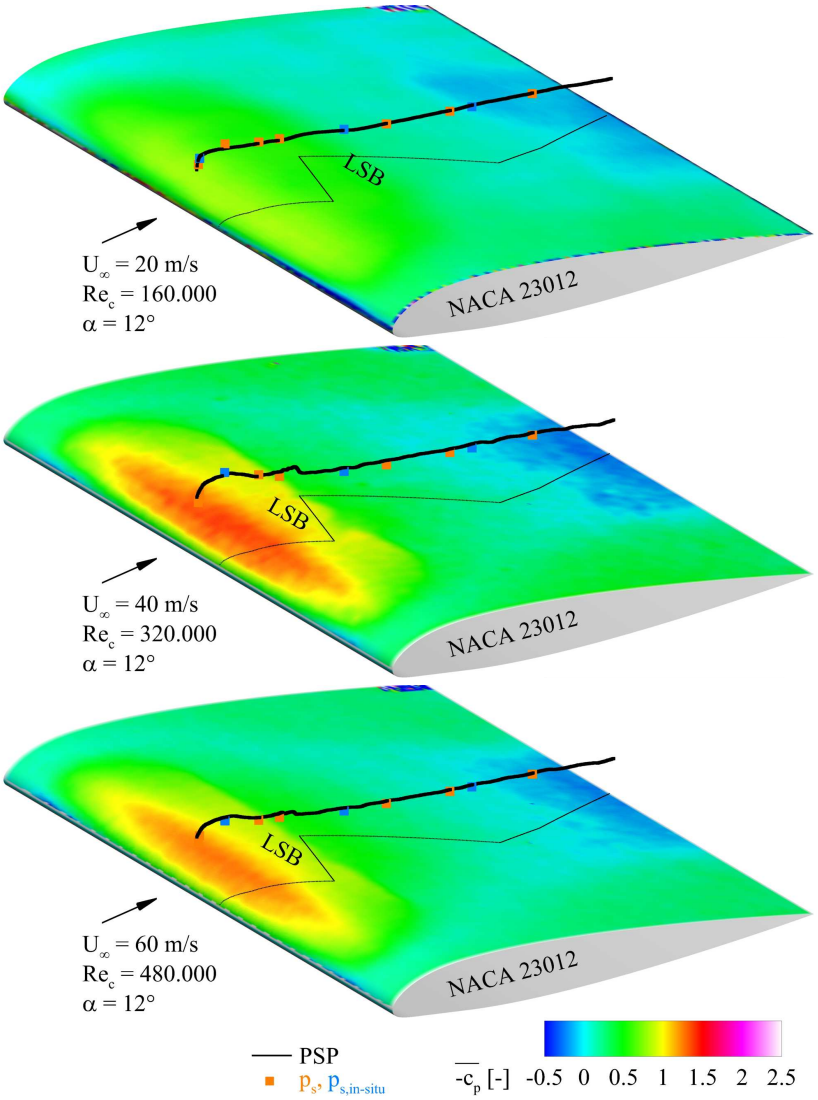

Fig. 5.6.: Pressure distributions on a *NACA* 23012 airfoil for different wind tunnel speeds $U_\infty = [20; 40; 60]$ m/s (from top to bottom) at a constant angle of attack $\alpha = 12°$.

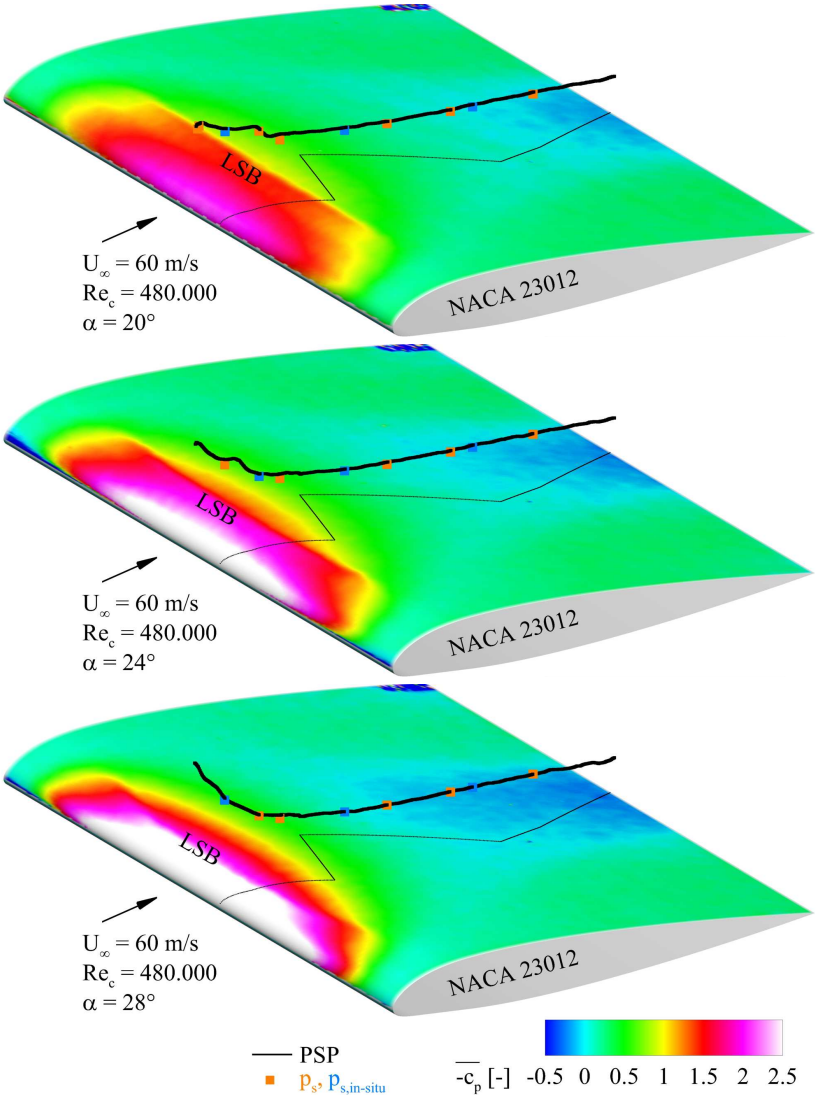

Fig. 5.7.: Pressure distributions on a *NACA* 23012 airfoil for different angles of attack $\alpha = [20; 24; 28]^\circ$ (from top to bottom) at a constant wind tunnel speed of $U_\infty = 60\,\mathrm{m/s}$.

At $U_\infty = 20\,\mathrm{m/s}$, a pressure gradient over the suction side of the airfoil of only $\Delta p_{ss} = p_{ss,max} - p_{ss,min} \approx 220\,\mathrm{Pa}$ was successfully resolved. A local flow separation (laminar separation bubble - LSB) clearly established behind the leading edge suction peak as a consequence of the flow Reynolds numbers, as indicated by the bump in the pressure lineplot. With raising flow speed, the length of the LSB decreased and the suction peak clearly established at the leading edge of the airfoil. The SNR of the PSP results also increased as a consequence of an increased dynamic pressure and hence a stronger pressure gradient. The highest SNR occurred at $U_\infty = 60\,\mathrm{m/s}$ and $\alpha = 28^\circ$. The temperature at the trailing edge of the airfoil changed by $\Delta T_{max} \leq 0.25K$ between the wind-on and the wind-off states during the individual experiments.

5.2.4. Measurement uncertainty

The deviation between the raw PSP results and the in-situ corrected results was estimated by means of some specific portions that were derived in Chapter 3 and by means of some assumptions from Liu and Sullivan (2005). Based on the individual uncertainties e_i, a global uncertainty $E_{est} = \sqrt{\sum {e_i}^2}$ is calculated. A portion of $e_T \approx 0.5\,\%$ is expected from the maximum temperature drift during the low-speed experiments as a consequence of the temperature dependence of the uni-paint ($T_{sens} = 0.6\,\%/K$). The uncertainty of the temperature sensor was included into this portion. The other individual portions are expected to have the following values:

specific uncertainty e_i	assumed portion [%]
a-priori calibration	1
paint thickness*	0.4
luminophore concentration*	0.3
photo degradation	0.3
spectral filter leakage*	0.5
excitation instability	0.1
model motion	0.1
temperature effect	0.5
mapping procedure	0.04 (7 images averaged)
total E_{est}	1.4

Tab. 5.2.: Estimation of the total PSP measurement uncertainty E_{est} representing the deviation between the actual and the in-situ corrected PSP results; * portions taken from Liu and Sullivan (2005).

U_∞ [m/s]	α [°]	Δp_{ss} [kPa]	$\overline{\Delta c_p}$	$\Delta c_{p,rms}$	E_{real} [%]
20	12	0.22	-0.0279	0.1381	-2.87
	20	0.19	0.0760	0.1656	14.28
40	12	1.02	-0.0138	0.0673	-1.22
60	12	2.23	0.0169	0.0444	1.49
	20	3.09	0.0152	0.0528	0.99
	24	3.73	0.0328	0.0678	1.78
	28	4.13	-0.0158	0.0654	-0.77
PSP accuracy at low speeds ($U_\infty \geq 40$ m/s)				0.0603	1.29

Tab. 5.3.: Relative and absolute measurement uncertainty in the final pressure mappings from the low-speed PSP experiments conducted on a *NACA* 23012 airfoil in the open-jet wind tunnel.

A total estimated deviation of $E_{est} \approx 1.4\%$ is expected between the raw and the in-situ corrected pressure mappings from these assumptions. The actual deviation was 2%. The deviations are in good agreement with each other because the values from Liu and Sullivan (2005) are only assumptions and some parameters (e.g. sensor linearity) were not even considered. Nevertheless, this error portion is only an intrinsic measure which expresses the execution quality of the PSP measurements itself. This error portion should completely vanish by applying an in-situ correction with static pressure taps. Hence, the absolute uncertainty of a PSP pressure distribution was calculated in the following manner:

- Calculate the pressure coefficients at each pressure taps as gathered ether from the pressure taps ($c_{p,s}$) or from the in-situ corrected PSP distribution in the vicinity of the pressure taps ($c_{p,psp}$).
- Calculate the difference at each pressure tap position and consider the average $\overline{\Delta c_p} = \overline{c_{p,s} - c_{p,PSP}}$ and the corresponding RMS values $\Delta c_{p,rms}$.

The taps which were used for the in-situ correction were not included in the calculations. The RMS value $\Delta c_{p,rms}$ finally represents the absolute measurement uncertainty for each test case. The results are given in Table 5.3.
The effective relative measurement uncertainty E_{real} was calculated between the tap data (p_s) and the PSP data (p_{psp}) in Pascal, normalized with the maximum pressure difference over the suction side of the airfoil (Δp_{ss}), such as:

$$E_{real} = \frac{\overline{p_s - p_{psp}}}{\Delta p_{ss}} \cdot 100\% \quad \text{with} \quad \Delta p_{ss} = p_{ss,max} - p_{ss,min} \tag{5.2.1}$$

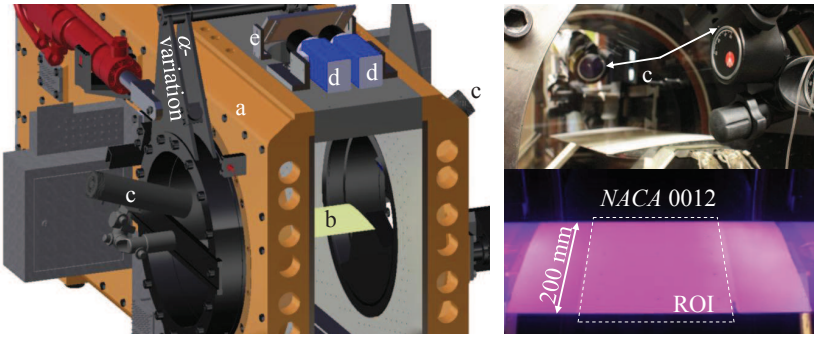

Fig. 5.8.: Experimental setup at the TWM (a) for the transonic PSP/TSP measurements on a *NACA* 0012 airfoil (b); 405 nm LED excitation (c), camera with signal filter (d) and mirror (e).

The measurement uncertainty was the highest at very low flow speeds due to the low dynamic pressure that caused only a small pressure gradient. PSP results can be obtained with an average relative measurement uncertainty of about 1.4% at flow speeds $U_\infty \geq 40\,\mathrm{m/s}$. The individual measurement uncertainties were finally averaged over all test cases in order to announce an absolute global measurement uncertainty for low-speed applications. Hence, the determination of the pressure coefficient was possible with $\Delta c_{p,\mathrm{rms}} \approx 0.06$. Compared with values from e.g. Engler et al. (2002) these values match the expectation at low-speed conditions and proved a good system performance. The comparably high uncertainty is the combined consequence mainly of the fairly low dynamic pressure, the small pressure gradient and the sensitivity of the paint.

5.3. PSP at transonic conditions

5.3.1. Experimental setup

Validation experiments of the steady PSP system were conducted in the TWM facility under transonic test conditions. PSP and TSP experiments were performed subsequently on two individual *NACA* 0012 airfoils. The TSP data was intentionally recorded in order to generate a data base for the validation of the TSP data evaluation in *IRES*. It was planned to validate the correction of PSP results by means of a TSP data set.
The binary-PSP (*BF400*) and the one-component TSP (*CCTE*) were applied on the suction side of the individual airfoils. Underneath the PSP layer, a base coating was applied and the marker application procedure resembled the low-speed test series. The

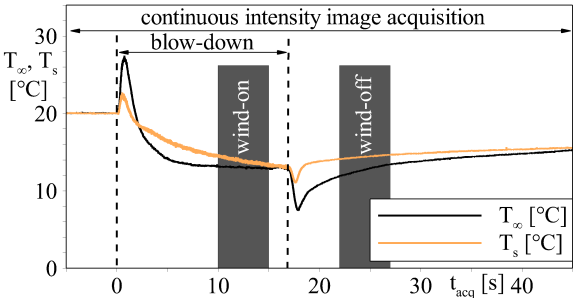

Fig. 5.9.: Development of the flow temperature T_∞ and the model surface temperature T_S before, during and after a wind tunnel run; 3 wind-on and wind-off intensity images were extracted from the time series data (gray boxes).

total PSP layer thickness was about $35-45\,\mu$m. The base coating thickness underneath the TSP was higher as it served for thermal insulation. The final thickness including the active TSP layer was about $120\,\mu$m.
The experimental setup in the TWM test section is sketched on the left in Figure 5.8. The right-hand side presents a closeup of the excitation LEDs and the PSP airfoil. The figures point out the spatial dimensions that were also implemented during the low-speed test series. The airfoils span extended the entire channel width (chord length was $c = 200\,$mm, $\Lambda = 1.5$). The LEDs were operated with the same parameters as in the low-speed experiments. Two 14 bit *pco.4000* CCD cameras mounted horizontally due to limited space were used for the PSP tests and one was used for the TSP measurements. Their view was deflected by 90° on a mirror. Each camera was equipped with a *Zeiss* Makro-Planar T* 2 / 50 mm lens and a filter mount between the camera and the lens. Interference filters were applied for signal separation (PSP_{red}: long-pass, $\lambda = 640\,$nm; PSP_{green}: band-pass, $\lambda = 550 \pm 40$; TSP: long-pass, $\lambda = 570\,$nm, $OD > 6$). A region-of-interest (ROI) of about $[150^W \times 200^L]$ mm was detectable by each camera. The spatial resolution at $\alpha = 4^\circ$ was about 11.1 px/mm (i.e. $M \approx 1:10$).
There were 42 static pressure ports located circumferentially around each airfoil, wheres 20 ports were available for the comparison with the PSP data inside the ROI. Three ports were used for the in-situ correction and the remaining ones were applied for the accuracy assessment. The static pressure at the ports was measured with a digital pressure scanning device *ESP-64HD* that was sampled with 1 kHz. The readings were finally averaged over 1 s averaged.
Each model was equipped with a pt100 RTD located at the trailing edge inside the ROI. The voltage values of the sensors were sampled with 1 kHz and recorded continuously for each intensity image.

quantity	change parameters (Mach number variation)			
Mach number M_∞ [1]	0.3	0.65	0.7	0.8
Reynolds number $Re_c[\cdot 10^6]$	4	[4; 6]	4	4
run static pressure p_s [kPa]	291.2	[120.4; 173.1]	112.5	93.2
dynamic pressure q_∞ [kPa]	18.3	[35.6; 51.2]	38.6	41.7
angle of attack α [°]	4	[0; 4; 8]	4	4
magnification M [1]	1 : 10			
pixel array $w \times h$ [px^2]	$1{,}670 \times 2{,}200$			
integration time PSP t_i [ms]	1,500			
integration time TSP t_i [ms]	800			
optic	*Zeiss* Makro-Planar T* 2 / 50 mm			

Tab. 5.4.: Flow conditions and acquisition parameter for the *NACA* 0012 PSP/TSP experiments in the trisonic wind tunnel (TWM).

5.3.2. Methodology

The blow-down process of the wind tunnel facility caused a continuous change of the surface temperature as a consequence of the fluid expansion. A complete homogenization of the surface temperature was not possible due to the limited run time. Figure 5.9 shows the typical behavior of the flow and the static model temperature during a wind tunnel run. The intensity images for each test case were recorded as a time series with a fixed frequency of $f_{acq} = 0.5\,\text{Hz}$. After the wind tunnel was started, the temperature was allowed to adapt for about 15 - 20 s before there was time for 3 wind-on intensity recordings at fairly stable temperature conditions. Three wind-off images were recorded immediately after the wind tunnel reached its resting state shortly after its shut-down.

A malfunction of the angle-of-attack control unit impeded the airfoil pitching after the wind tunnel start in order to prevent potential flow separations. The angle of attack was calibrated and locked manually prior to each test. The facility was extensively cleaned before the experiments in order to avoid potential paint contaminations caused by seeding fluids in the flow or on the walls of the wind tunnel.

Flow parameters like Mach and Reynolds number or the angle of attack were varied during the experiments. Only one flow condition was varied at the same time. A constant Reynolds number resulted in large static pressure differences inside the test section during the individual tests. All relevant flow quantities and acquisition parameter are summarized in Table 5.4.

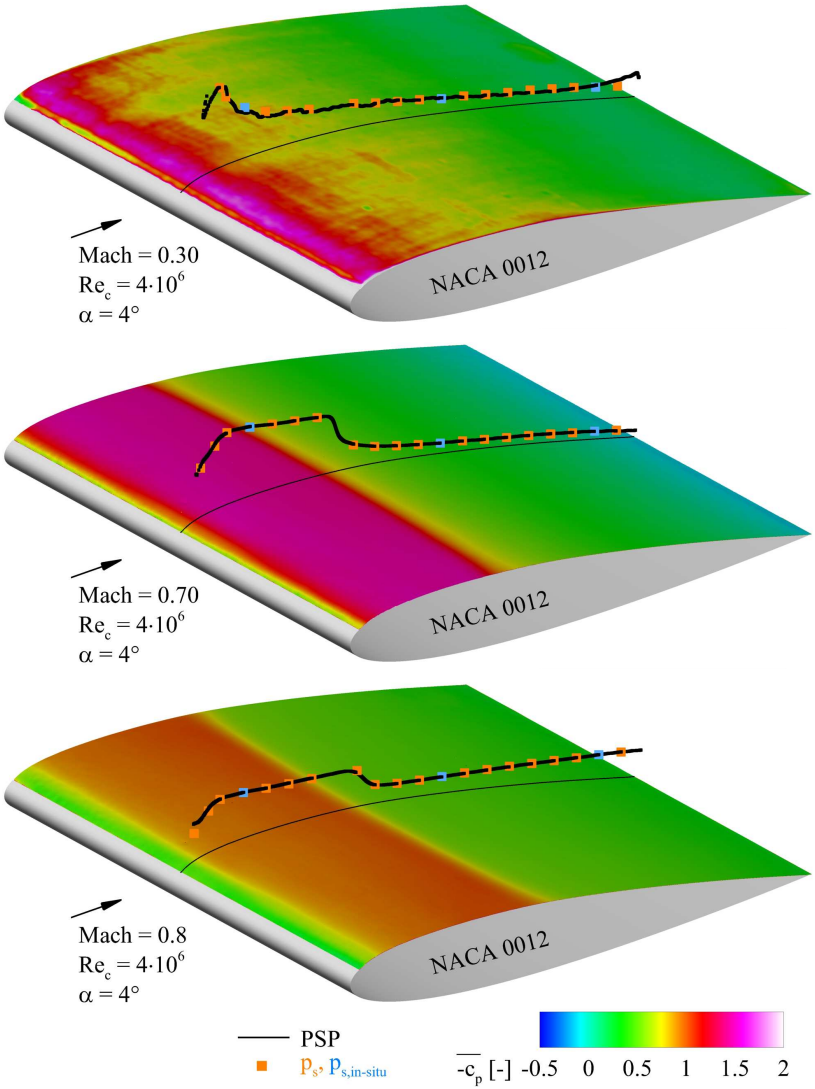

Fig. 5.10.: Pressure distributions on the suction side of a *NACA* 0012 airfoil for different flow Mach numbers $M_\infty = [0.3; 0.7; 0.8]$ (from top to bottom) at a constant angle of attack $\alpha = 4°$ and a constant Reynolds number $Re_c = 4 \cdot 10^6$.

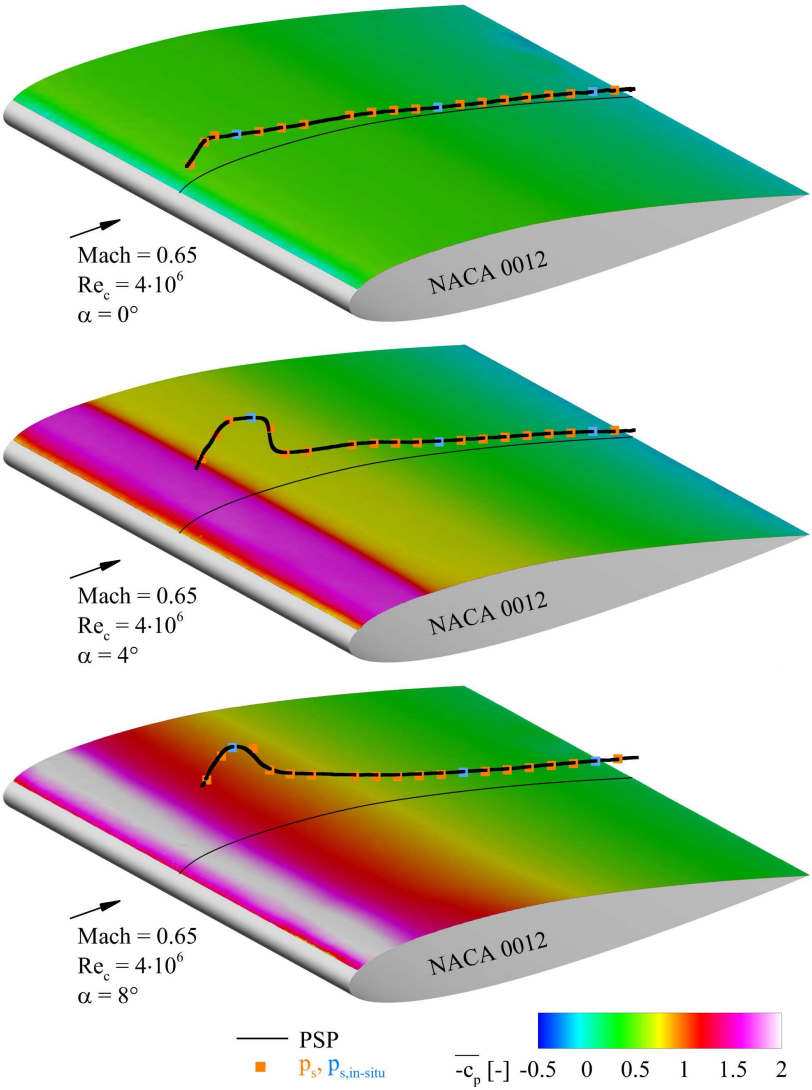

Fig. 5.11.: Pressure distributions on the suction side of a *NACA* 0012 airfoil for different angles of attack $\alpha = [0; 4; 8]^\circ$ (from top to bottom) at constant wind tunnel Mach and Reynolds numbers $M_\infty = 0.65$, $Re_c = 4 \cdot 10^6$.

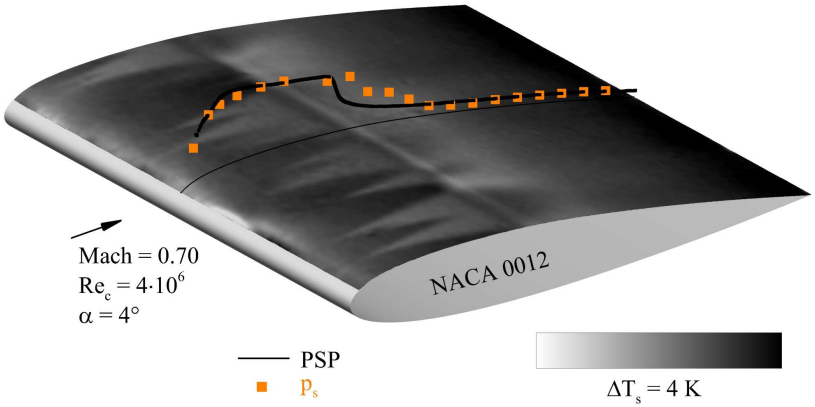

Fig. 5.12.: Temperature map on a *NACA* 0012 airfoil at $M_\infty = 0.7$, $Re_c = 4 \cdot 10^6$ and $\alpha = 4^\circ$. The pressure distribution from the TSP airfoil (*orange*) is compared with the one from the PSP airfoil (*black*) in the plane of symmetry.

5.3.3. Results

Figure 5.10 shows the ensemble-averaged surface pressure distributions $-\overline{c_p}$ on the suction side of the airfoil for various Mach numbers $M_\infty = [0.3; 0.7; 0.8]$ (from top to bottom) at a constant angle of attack $\alpha = 4^\circ$ and a constant Reynolds number $Re_c = 4 \cdot 10^6$. Figure 5.11 displays the corresponding pressure mappings for different angles of attack $\alpha = [0; 4; 8]^\circ$ (from top to bottom) at constant Mach and Reynolds numbers $M_\infty = 0.65$ and $Re_c = 4 \cdot 10^6$, respectively. The results show a widely two-dimensional flow topology unlike the results from the low-speed experiments. Hence, the PSP data could be extracted at the plane of symmetry at $y = 0$ for a comparison with the readings from the static pressure ports as indicated by the black trace. The pressure distribution at $M_\infty = 0.3$ hypothesizes that the flow was not fully developed and suffered from the high turbulence level. The high static pressure inside the test section as a consequence of the constant Reynolds number additionally affected the result. A pressure difference of $\Delta p_{ss} = 19.2\,\text{kPa}$ was measured along the suction side of the airfoil at $M_\infty = 0.3$. The other plots show a smooth and homogeneous pressure distribution. The location of the suction peak at the leading edge as well as the position of the re-compression was determined precisely. The re-compression partly occurred as a sharp shock (e.g. $M_\infty = [0.65; 0.7]$ at $\alpha = 4^\circ$) or as blurred isentropic re-compression (e.g. $M_\infty = 0.65$ at $\alpha = 8^\circ$).
Figure 5.12 shows the surface temperature distribution on the suction side as a result

M_∞	α [°]	Re_c [$\cdot 10^6$]	Δp_{ss} [kPa]	$\overline{\Delta c_p}$	$\Delta c_{p,rms}$	E_{real} [%]
0.3	4	4	28.1	-0.0150	0.0443	-0.98
0.65	0	4	19.2	-0.0038	0.0153	-0.72
	4	4	59.1	-0.0143	0.0300	-1.05
	4	6	85.0	0.0130	0.0287	0.79
	8	4	61.7	0.0224	0.0439	1.39
0.7	4	4	58.2	0.0032	0.0181	0.21
0.8	4	4	31.3	-0.0002	0.0232	-0.07
PSP accuracy for the TWM test series					0.0309	0.86

Tab. 5.5.: Relative and absolute measurement uncertainty in the final PSP results at high-speed test conditions in the TWM.

of the TSP measurements. Several issues finally impeded the application of the TSP results for a reduction of the PSP temperature effect. Since the transition of the boundary layer state from laminar to turbulent was not enforced by some artificial surface roughness, turbulent wedges formed on the leading edge as a consequence of small surface roughness due to impact of dust or ice particles or other painting enclosures. The transition can also be tripped by means of some artificial surface roughness such abrasive paper. The second issue was the deviation between the geometric cross sections of the individual airfoils. The geometry difference led to a difference in the pressure distributions between both airfoils as to be seen by comparing the static pressure readings from the TSP airfoil (*orange*) and the data from the PSP airfoil (*black*). An image-pattern correlation measurement (optical geometry reconstruction) of both clean airfoils without any coating revealed contour deviations of 0.1 mm at its maximum. Due to this issue the idea of correcting the PSP data by using the TSP information was renounced. Nevertheless, it could be stated that the surface temperature distributions can be measured within an accuracy of $\Delta T < 0.1\,\mathrm{K}$ by means of the TSP measurement technique.

5.3.4. Measurement uncertainty

The deviation between the raw PSP results and the in-situ corrected results under transonic conditions was estimated similar to the low-speed test series. Most of the individual uncertainty portions from the low-speed tests were also applied in order to estimate the total expected uncertainty of the raw PSP results E_{real} during the transonic tests. The portion of the temperature effect was adapted to $e_T = 0.3\%$. This value was estimated from the surface temperature gradient (about $\Delta T \approx 5\,\mathrm{K}$) and the temper-

ature sensitivity of the binary-PSP. On the other hand, the portion of the model motion had to be increased due to strong aerodynamic forces and a shift of about 1-2 px between the wind-on and the wind-off images. Finally, the deviation between the raw and the corrected results was estimated with $E_{\text{est}} \approx 1.3\%$. The actual deviation was $E \approx 1.7\%$. The agreement is even better compared to the low speed experiments. Table 5.5 discusses the relative and absolute measurement uncertainties E_{real} and $\Delta c_{\text{p,rms}}$ similar to the low-speed results for each test case. Since PSP measures absolute intensities, the significantly higher pressure gradient along the suction side resulted in an explicitly stronger intensity change in comparison with the low-speed results. This is also reflected in the final measurement uncertainties. A PSP measurement under transonic test conditions in the TWM facility is possible with an accuracy of $E_{\text{real}} \approx 0.86\%$ for flow Mach numbers of $0.3 \leq \text{M}_\infty \leq 0.8$. An absolute measurement uncertainty of $\Delta c_{\text{p,rms}} \approx 0.031$ can be given for the pressure coefficient calculation. The relative uncertainty during the transonic test was reduced by about 0.4 % in comparison to the low-speed experiments. A comparison with a wide variety of transonic experiments from literature revealed that state-of-the-art PSP systems are able to measure with an absolute uncertainty of $\Delta c_{\text{p,rms}} = 0.005 \ldots 0.01$. These values were partly reached in the presented experiments. Nevertheless, the scattering of the uncertainty values was slightly too large over the tested Mach and Reynolds number range. The uncertainty of prospective experiments can be reduced with a larger number of wind-on recordings and a better treatment of the temperature effect.

5.4. Summary

The performance of the entire PSP system as well as its measurement uncertainty were benchmarked by means of a low-speed and a transonic test series. Low-speed experiments were conducted in the open-jet wind tunnel facility on a *NACA* 23012 airfoil at flow speeds up to $U_\infty = 60\,\text{m/s}$. The final relative measurement uncertainty was between 1 and 2 percent for the low-speed tests. The low-speed pressure coefficient map can be calculated with an uncertainty of $\Delta c_{\text{p,rms}} = 0.06$.
Transonic PSP experiments were conducted in the TWM facility on a *NACA* 0012 airfoil at Mach numbers ranging from $\text{M}_\infty = [0.3 \ldots 0.8]$. The final relative measurement uncertainty was reduced below 1% during these experiments as a consequence of the larger pressure gradient and the higher SNR. A pressure coefficient map was finally estimated with $\Delta c_{\text{p,rms}} = 0.03$ for Mach numbers $0.3 \leq \text{M}_\infty \leq 0.8$. It was shown for both test series that the actual uncertainty between the raw and the in-situ corrected pressure distributions was about $E \approx 2\%$ (low-speed) and $E \approx 1.7\%$ (high-speed) which was in good agreement with the estimated value.
Temperature-sensitive paint measurements were also performed under transonic conditions. The data was suitable to benchmark the TSP evaluation in *IRES*. The determination of surface temperature distributions was possible with an accuracy of $\Delta T < 0.1\,\text{K}$.

6. Characterization of a turbulent separating/reattaching flow

This chapter concentrates on the investigation of the scientific key questions that are from particular interest within the project part of UniBwM (see introduction). In order to answer these questions, the dynamics of coherent flow pattern in the near wake are examined by means of transient optical velocity and pressure measurements. The investigations were conducted as follows:

1. The boundary layer state on the cylindrical body was initially investigated by means of the standard particle image velocimetry (PIV). It was from importance that the boundary layer, which separates from the base of the generic configuration, is fully turbulent at this position in order to match the real flight conditions.

2. The topology and dynamics of coherent flow pattern in the recirculation area were examined by means of the time-resolved particle image velocimetry (TR-PIV).

3. The coherent pressure dynamics in the recirculation area were characterized by means of the instationary pressure-sensitive paint measurement technique (iPSP). This test series was split into two sub series: The first series focused on the base flow in the lateral plane. The second series concentrated on the interaction between the wake flow and the nozzle structure (here: the support sting).

The particular interest of the project part at UniBwM is the characterization of the flow/structure interaction under transonic conditions at $M_\infty = 0.7$. Some experiments were additionally conducted at low-speed conditions ($M_\infty = 0.3$). Transient measurements were required in order characterize the flow dynamics as they might originate from dominant vortex shedding. The results are widely summarized in Bitter et al. (2011) and Bitter et al. (2012).
The outline of this chapter is as follows: The design and the technical equipment of the generic spacecraft model is initially discussed. The predictions from 2D- and 3D-RANS CFD simulations, which were performed in parallel to the experiments, are discussed in the following. The numerical simulations were performed in order to compare the topology of the wake flow with the test results. Afterwards, the experimental setups for the individual experiments are introduced before the methodology for the data acquisition and conditioning is presented separately for each test series. The results of the experiments are finally discussed in the order of their appearance.

6.1. Generic spacecraft model

Figures 6.1 and 6.2 show the components and the dimensions of the modular generic configuration that was used for the experiments. It is a 1:100 scaled generic model of an *ARIANE V* spacecrafts main stage without boosters. The main diameter of the model was $D = 54\,\text{mm}$ and its overall length was $l = 231.3\,\text{mm}$. It was designed in a shell-like construction to allow for the equipment with static and unsteady pressure and temperature sensors. The nose cone had a full aperture angle of 36° and a nose radius of $R = 5\,\text{mm}$. The cylindrical part had a length $l = 164.3\,\text{mm}$.
The model was equipped with 16 unsteady pressure transducers (*Kulite XCQ-62*) with a maximum gauge pressure difference of 350 kPa. 13 of the transducers were located in the base, see detail A in Figure 6.2. At the time of the experiments, it was only possible to acquire the signals from four sensors simultaneously. The picked sensors were located on a radial line at $r/R = [0.45; 0.52; 0.85; 0.95]$.
There were 4 static pressure ports on the cylindrical part circumferentially distributed over 90° which were used to avoid a potential oblique installation of the model in the test section. A pressure manifold was installed inside the model in oder to distribute the static reference pressure from the test section directly to the reference ports of the unsteady pressure transducers. Furthermore, the model included 4 static temperature sensors (PT1000 *RTD, M222*) - 2 at the cylindrical part and 2 inside the base. These were incorporated into the model's surface by a thermal adhesive.
A rear sting support was used for the installation of the model in the test section. It was turned from a steel pipe and had a length of about 700 mm. The outer diameter of the support was $D = 21.5\,\text{mm}$. It emulated the dimensions of a scaled nozzle which is placed instead at the original spacecraft. The length of the nozzle would have been about 1.2 times the model diameter. This type of model suspension was chosen in order to avoid strong three-dimensional flow effects that a strut-mounting would have caused (as investigated by van Oudheusden and Scarano (2008)). The influence of this model support on the flow (e.g. a potential delay or even prevention of the wake reattachment - open wake) was examined in Scharnowski and Kähler (2011). An open wake as a consequence of the model support occurred for inlet Mach numbers of $M_\infty > 2$ and was no problem at subjacent flow speeds.
All magnetically shielded lead wires and pressure hoses were fed through the sting support. From manufacturing reasons, the sting support carried no temperature and pressure sensors.

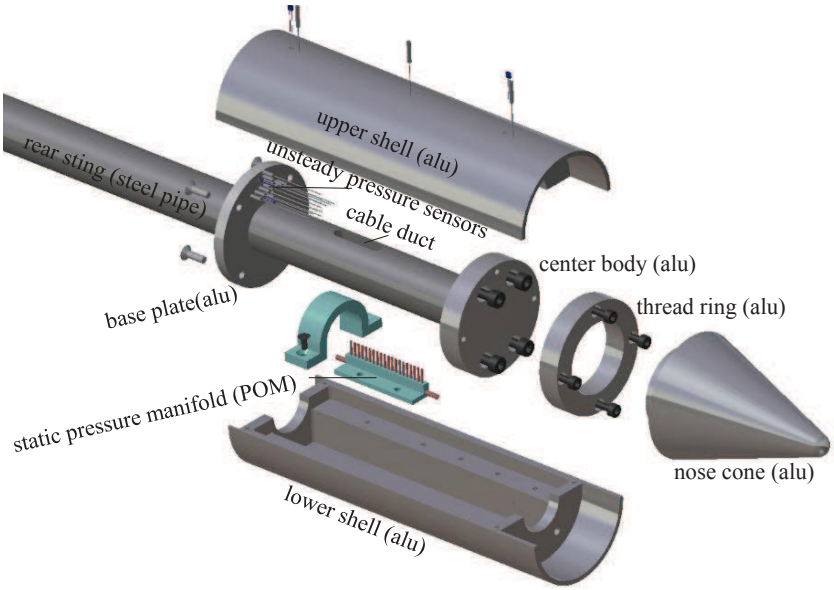

Fig. 6.1.: Components of the modular generic spacecraft model made from aluminum. The model is equipped with: 16 unsteady pressure transducers - 13 in the base and 3 in the cylindrical part; four static pressure ports at 90° in the vicinity of the nose cone; four static temperature sensors - two in the base and two in the cylindrical part.

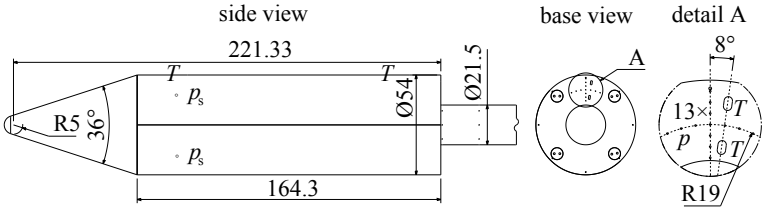

Fig. 6.2.: Dimensions of the generic spacecraft model (all dimensions in mm). The positions of the pressure transducers, the static pressure ports and the temperature sensors are marked with p, p_s and T, respectively.

6.2. Numerical predictions

Two- and three-dimensional Reynolds-Averaged Navier-Stokes (RANS) simulations were performed in order to:

1. get an impression of the flow topology in the vicinity of the model,
2. have a comparison for the experimental results,
3. simulate the follow-up behavior of tracer particles in the flow and estimate the tracer density in near-wall regions,
4. estimate the iPSP measurement uncertainty from the surface temperature distribution (as a consequence of compressibility effects).

The 2D mesh (created with *Centaur*™) consisted of about 200,000 unstructured grid nodes. The boundary layer on the model and sting support was resolved by 30 structured cell layers with an initial cell height of $h_{\mathrm{ims}} = 1.0 \cdot 10^{-6}$ m and a subsequent stretching of 1.24 in order to cover an expected boundary layer height of about 6 mm. A cell-refinement box was created in the wake that restricted the cell size to approx. 1 % of the model diameter. It extended from the base until $x/D = 5$ and $z/D = 2$. The flow problem was initialized with axisymmetric and pressure farfield boundary conditions.
The 3D mesh was created from one quarter of the model geometry inside the TWM test section. Horizontal and vertical symmetry conditions as well as pressure in- and outlet were defined at the corresponding walls. The grid consisted of about 3.3 million cells and had a similar cell refinement as the 2D mesh. About 800,000 structured elements were used for the boundary layer (30 layers, $h_{\mathrm{ims}} = 1.0 \cdot 10^{-6}$ m, stretching 1.24).
The simulations were performed by means of the commercial flow solver *Fluent* while they were initialized with the flow conditions at $M_\infty = 0.7$ from Tab. 6.1. The Reynolds-stress turbulence model with default parameters, an explicit time-stepping scheme with $CFL = 2$ and the density-based flow solver preset were applied in 2D and 3D. The results were converged (residuals $\leq 10^{-5}$) after approx. 15,000 and 5,400 iterations in 2D and 3D, respectively. Figure 6.3 compares the results of the 2D and the 3D simulations and estimates the displacement effect of the model in the test section compared to the free-flight boundary condition. A dislocation of the reattachment position of 5 % and an increase of the outer flow speed by 1.5 % was the consequence from the 3D boundary conditions. Hence, the more convenient 2D data can be used for a latter comparison with the data from the planar PIV measurements.
The follow-up behavior of tracer particles was examined by means of the 2D simulations in Fig. 6.4. The particles cannot follow strong flow gradients as a consequence of inertial effects. Such strong gradients occur at the position where the nose cone merges into the cylindrical part or were the flow separates from the base. Solid particles with the density of the seeding fluid DEHS ($\rho = 912\,\mathrm{kg/m^3}$) were injected into the flow up-

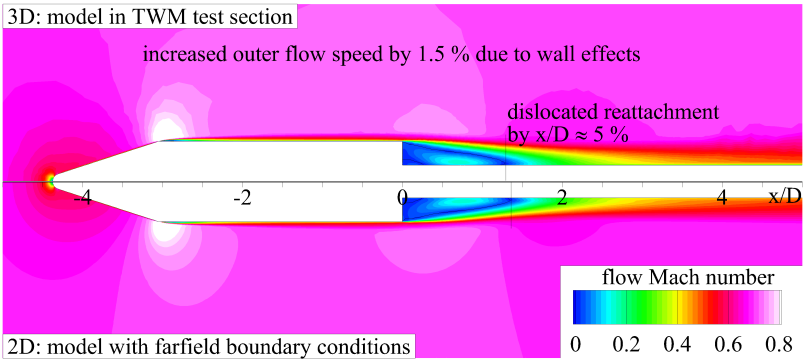

Fig. 6.3.: Comparison of the flow fields between the 3D-RANS simulation with TWM boundary conditions (*top*) and the 2D-RANS simulation with farfield conditions (*bottom*); $M_\infty = 0.7$, $Re_D = 1 \cdot 10^6$.

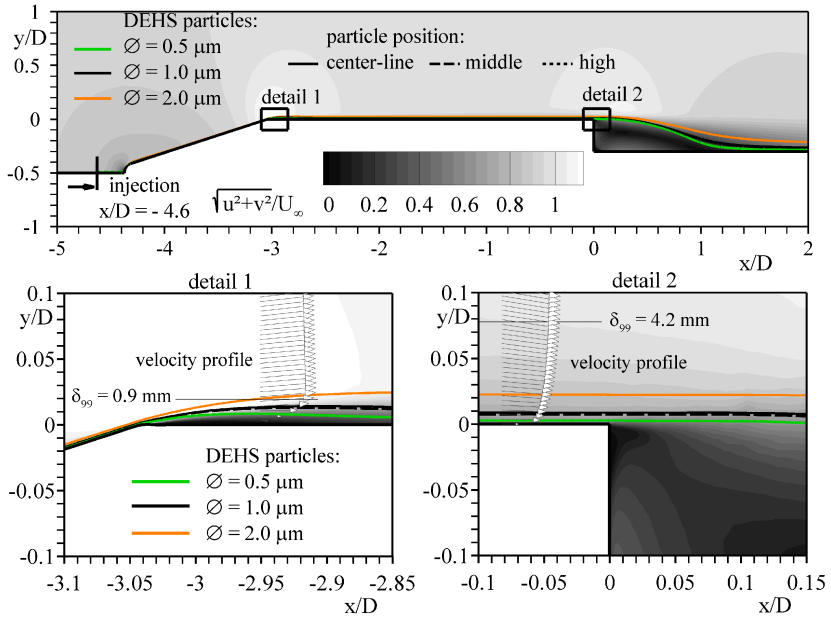

Fig. 6.4.: Contour-plot of the velocity magnitude in the vicinity of the model as a result from a 2D-RANS simulation at $M_\infty = 0.7$ test conditions characterizing the flow-follow behavior of tracer particles.

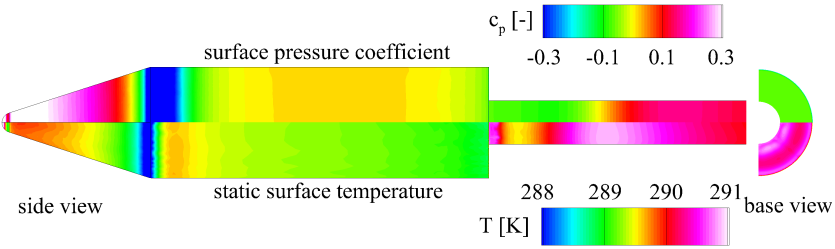

Fig. 6.5.: Results of a 3D-RANS simulation of the $M_\infty = 0.7$ test case; *Top:* surface pressure coefficient; *Bottom:* static surface temperature; *Left:* side view; *Right:* base view from the rear.

stream of the model. The size of the particles was varied between $[0.5 \leq d_p \leq 2.0]\,\mu$m indicated by the different colors of the particle trajectories. The particles were injected close to the symmetry line at $y_1 = 1 \cdot 10^{-5}\,x/D$ and at $y_{i=2,3} = y_1 + (i-1) \cdot 0.025\,x/D$. The particle trajectories nearly merge at the model nose. The smaller the particles, the better is their ability to follow the strong curvatures. The resolution of near-wall boundary layer domains is impeded by larger tracer particles and seems to be possible with particles that have a size of $0.5\,\mu$m or even smaller. However, three-dimensional and unsteady effects would carry a fraction of particles in near-wall regions and into the wake recirculation area during the experiments. Nevertheless, it is expected that the seeding density is significantly lower in these areas.

Figure 6.5 shows the surface pressure coefficient c_p as a result from the 3D simulations. A similar pressure distribution in the wake and on the model base is expected from the ensemble-averaged iPSP experiments. The absolute pressure difference between the core and the reattachment of the wake recirculation vortex is predicted to be approx. 19 kPa.

The lower part of the figure displays the static temperature distribution. A temperature gradient of $\Delta T \approx 3$K can be examined in the regions-of-interest for the iPSP measurements. An in-situ pressure error of about 7-8 % is expected if the temperature dependence of pc-PSP is applied.

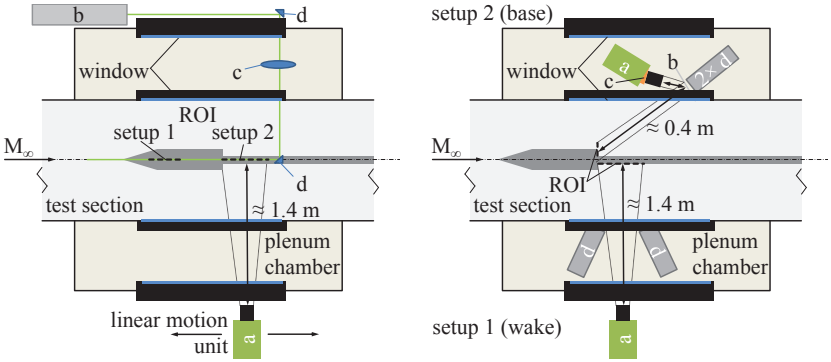

Fig. 6.6.: *Left:* Non-scaled schematic of the experimental setups for the TR-PIV investigations; camera (*a*), high-repetition-rate laser (*b*), light sheet optics (*c*), mirror (*d*); *Right:* setups for the iPSP experiments; near-wake characterization (setup 1); base flow investigations (setup 2); camera (*a*), mirror (*b*), Scheimpflug-angle correction device (*c*), excitation LED (*d*).

6.3. Experimental setup and test parameter

The TR-PIV and iPSP measurements were performed consecutively in the TWM facility at Mach numbers $M_\infty = [0.3; 0.7]$. The Reynolds numbers were chosen in order to match the demands of project partners who are responsible for more detailed numerical investigation on this configuration by means of large-eddy or detached-eddy methods. The Reynolds numbers (with respect to the base diameter) were $Re_D = [0.7; 1.0] \cdot 10^6$ (higher at $M_\infty = 0.7$). The wind tunnel turbulence level at the subsonic conditions was $Tu \approx [2.5, 1.2]\,\%$ (lower at $M_\infty = 0.7$). The individual experimtental setups are introduced in the following.

PIV measurements

A high-repetition-rate PIV system with a *Quantronix* Darwin Duo Nd:YLF double-pulse laser was used. The laser had a pulse duration of $t_p \approx 120\,\text{ns}$ providing 22 mJ laser light energy per cavity at 1 kHz repetition rate. The laser beam with a divergence of $D_M^2 \approx 25\,\text{mrad}^2$ was led through two spherical lenses with focal lengths of $F = -40\,\text{mm}$ and $F = +50\,\text{mm}$ followed by two cylindrical lenses with $F = -25\,\text{mm}$ and $F = +50\,\text{mm}$ in order to form the laser-light sheet. Its thickness in the focal line was approx. $1{,}500\,\mu\text{m}$. A perpendicular access of the laser beam into the plenum cham-

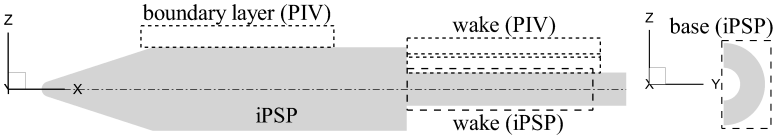

Fig. 6.7.: Definition of the coordinate system and the fields-of-view for the TR-PIV (*dotted*) and the iPSP measurements (*dashed*).

ber was mandatory in order to avoid a potential light sheet dislocation as a consequence of density changes during a wind tunnel run. A mirror on the sting support finally redirected the light sheet towards the model. The installation of the PIV system at the TWM test section is sketched on the left in Fig. 6.6. A *Phantom V.12* high-speed CMOS camera with a resolution of 1 Mpx (frame rate 6200 frames/s at full resolution) was used for the image recording. The field-of-view for the boundary layer investigations was $125^W \times 20^H\ mm^2$ and it started 0.2 model diameters ahead the junction of the cylindrical part and the nose cone, as outlined in Fig. 6.7. The wake investigations were split into two parts in order to have a high spatial resolution. Each wake field-of-view had a height of 0.22 model diameters with a slight overlapping, compare Fig. 6.7. The PIV tracer particles were generated from DEHS (Di-Ethyl-Hexyl-Sebacat) by means of two *PivTec* seeding atomizers. They produce particles with a mean diameter of $1\,\mu$m and a relaxation time of about $2\,\mu$s, see Ragni et al. (2011). The specific test conditions and recording parameters for the PIV experiments are given in the upper part of Table 6.1.

PSP measurements

The transient pressure-sensitive paint measurement technique with a polymer/ceramic base layer (pc-PSP) was used for the time-resolved characterization of coherent surface pressure pattern. The formulation of the base coat was introduced in Section 2.1.4. The active layer was composed from 5 mg of PtTFPP dissolved in 20 ml of toluene. Both compositions were applied to the model by a spray gun. The thickness of the entire coating was $d_{\text{poly}} \approx 15\,\mu$m.
The registration markers from round cavities with a diameter of 0.5 mm were incorporated in the model during the manufacturing process. They were cleared from polymer fill-up after the pc-PSP layer has dried.
The experiments were split into two test series regarding the scientific key questions. The sting support was coated with pc-PSP within a range of 100 mm (or $1.8\,x/D$) downstream of the model base in order to investigate the flow/structure interaction in the wake, see left side of Figure 6.8. The base was coated with pc-PSP over 180° for the

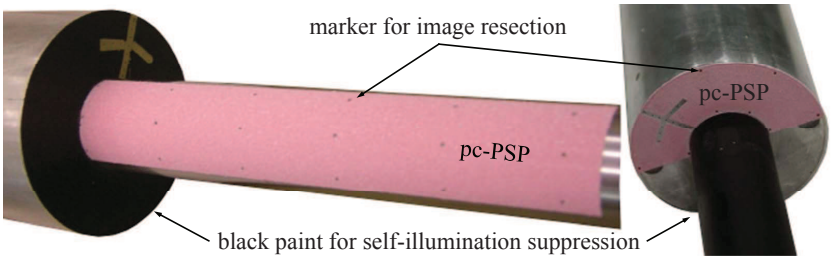

Fig. 6.8.: *Left:* rear-sting mounting covered with pc-PSP for wake dynamics characterization; *Right:* base covered with pc-PSP for mode structure investigations.

second test series in order to resolve potential characteristic pressure modes, compare right-hand-side in Figure 6.8. The corresponding experimental setups for these experiments are sketched on the right in Figure 6.6.
A *Phantom V.12* high-speed CMOS camera (a) was used for image recording in both test series. The camera was installed out of the plenum chamber at a distance of about 1.4 m away from the PSP surface during the wake investigations (setup 1). For the base-flow investigations (setup 2), the camera was attached directly to the wind tunnel wall in the plenum chamber at a distance of about 0.4 m. The camera view was deflected on a mirror (b) in order to allow the observation of the base area from the rear. The usage of a Scheimpflug device (c) was mandatory in order to ensure a constant image sharpness. The image would have been partly blurred as a consequence of the oblique viewing plane if this device is rejected.
A high pass filter with a cut-on wavelength of 570 nm (transmission $T \geq 93\,\%$, optical density $OD > 6$) was used in front of the objective lens for signal separation. Two *Luminus CBV-120UV* high power LEDs (d), each with 10 W optical power, were operated in continuous-wave mode for the excitation of the PSP. A spherical lens with a focal length of $F = -75\,\text{mm}$ and a diameter of $D = 120\,\text{mm}$ was used in front of each LED in order to maximize the excitation intensity for short integration times and to ensure a homogeneous light distribution. The LEDs were installed directly at the window to the test section inside the plenum chamber in both setups. The specific test conditions and recording parameters for the iPSP experiments are given in the lower part of Table 6.1.

	TR-PIV investigations				
region-of-interest ROI	boundary layer			wake (*left*: upper ROI; *right*: lower ROI)	
Mach number M_∞	0.3; 0.7				
Reynolds number $Re_D[\cdot 10^6]$	0.7; 1.0 (with respect to M_∞)				
run total pressure p_t [kPa]	200; 150 (with respect to Re_D)				
PIV sampling rate $f_{s,PIV}$ [Hz]	500			4,000	
Δt [μs]	6; 3 (with respect to M_∞)			10; 5 (with respect to M_∞)	
field-of-view $W \times H$ [mm^2]	125×20			125×35	125×30
pixel array [px^2]	$1{,}280 \times 200$			$1{,}280 \times 350$	$1{,}280 \times 300$
optics	Zeiss Sonnar T* 2.8/180 mm, F4				
magnification M	1 : 5				
recordings N [$\cdot 10^3$]	10			8	
	iPSP investigations				
region-of-interest ROI	wake (sample rate variation)			base (sample rate variation)	
Mach number M_∞	0.3; 0.7				
Reynolds number $Re_D[\cdot 10^6]$	0.65; 1.0 (with respect to M_∞)				
run total pressure p_t [kPa]	170; 150 (with respect to Re_D)				
run static pressure p_s [kPa]	160; 107 (with respect to Re_D)				
Kulite sampling rate $f_{s,kul}$ [Hz]	10,000				
iPSP sampling rate $f_{s,iPSP}$ [Hz]	1,000	2,000	4,000	1,000	2,000
cut-off frequency f_c [Hz]	512	1,024	2,048	512	1,024
integration time $t_{i,iPSP}$ [μs]	999	499	249	999	499
field-of-view $W \times H$ [mm^2]	106.4×32.2	80.5×23.4	51.8×17.6	31.4×57.5	31.4×57.5
pixel array [px^2]	$1{,}184 \times 352$	896×256	576×192	336×768	336×768
optics	Zeiss Sonnar T* 2.8/180 mm, F5.6			Zeiss Macro-Planar T* 50 mm, F4	
magnification M	1 : 4.5			1:4.6	
recordings N [$\cdot 10^3$]	12	24	44	21	

Tab. 6.1.: Flow conditions and image acquisition parameter for the transient PIV and PSP investigations in the TWM.

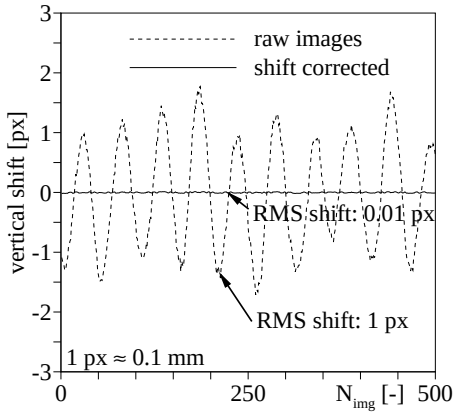

Fig. 6.9.: Time series of 500 PIV recordings showing the raw (*dashed*) and the shift corrected (*solid*) wall position at $M_\infty = 0.7$.

6.4. Data handling

PIV measurements

Data acquisition

The PIV data acquisition and processing was performed with *DaVis* from *LaVision.* The pulse delay Δt between the particle illumination was chosen between 3 and 6 microseconds for the boundary layer investigations and between 10 and 5 microseconds in the slower wake.

The image acquisition rates for the boundary layer investigations were $f_{acq} = 500\,\text{Hz}$. The wake experiments were performed at sampling rates of 4,000 Hz in order to resolve shedding frequencies of $f_{shed} = [405, 900]\,\text{Hz}$ (higher at $M_\infty = 0.7$) based on an expected reduced frequency ($St_D = f \cdot D / U_\infty$) of $St_D = 0.21$. Between 8,000 and 10,000 PIV images were recorded in the individual test series according to Table 6.1.

Pre-processing

A pitching motion of the model which was partly stimulated by vortex shedding from the base was corrected in the PIV images using a cross-correlation algorithm in order to ensure a resting wall position for an accurate calculation of near-wall velocity gradients. Two image features (e.g. reflections) were tracked and their shifts relative

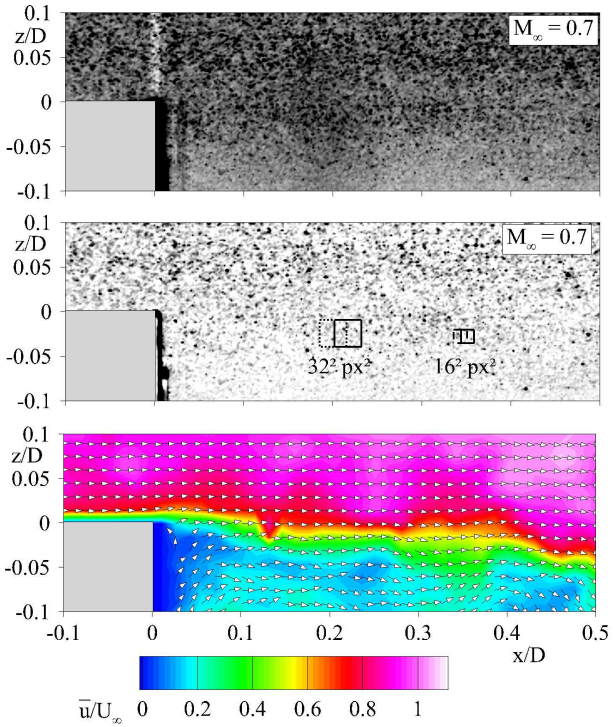

Fig. 6.10.: *Top:* clipping of an inverted raw PIV image at $M_\infty = 0.7$ in the vicinity of the base; *Middle:* intensity-filtered and shift corrected image for further processing; *Bottom:* instantaneous and post-processed vector field in the vicinity of the base (every second vector is shown).

to the first image of the series were calculated. The shifted image was interpolated on a regular grid for further processing. Fig. 6.9 displays the raw and the shift-corrected model motion amplitudes for 500 images.
An initial filtering of the PIV recordings was performed in order to avoid potential spurious vectors due to low signal-noise-ratios. A sliding average was calculated in each PIV image within windows of size $10^2\,\mathrm{px}^2$ that overlapped by 1 px. The average values were subtracted from the raw image at the corresponding positions. The particle image size was not affected by this procedure.

Main PIV evaluation

The evaluation of the boundary layer data was performed using a multi-pass sum-of-correlation scheme with a decreasing interrogation window size from 32^2 px^2 to 6^2 px^2. The window overlap was 50 %. The major interest of these investigations were not the flow statistics but the topology of the boundary layer. The sum-of-correlation scheme offered a high spatial resolution but annihilated the temporal information. A spatial resolution of 420×65 vectors or 3.3 vectors/ mm was reached by means of this procedure. The evaluation in the wake was performed by means of a hybrid approach. An initial average flow field was calculated over 500 images by means of sum-of-correlation with a decreasing interrogation window size ($32^2 \rightarrow 16^2$ px^2). This vector field was used as a starting solution for the calculation of the instantaneous vector fields by means of a multi-pass cross-correlation scheme. The interrogation window size decreased from 32^2 px^2 to 16^2 px^2. The final correlation pass was carried out twice. The window overlap was 50 %. The spatial resolution of the merged data from both ROIs was 160×80 vectors or 1.4 vectors/ mm.

Post-processing

A strong vector-post processing (outliers between 5-10 %, higher at $M_\infty = 0.7$) was applied to the instantaneous wake vector fields in order to exclude all outliers which could affect the statistics. The resulting vector gaps were filled up by interpolation in order to ensure a gap-less time series data. The fill-up was done by means of the *Matlab*™ surface interpolation scheme. Figure 6.10 shows a closeup of an inverted raw PIV recording (*top*), the same filtered and shift-corrected image (*middle*) and the corresponding instantaneous velocity field (*bottom*) at $M_\infty = 0.7$ as a prove of the image processing. The number of seeding particles seemed to be reduced from step one to step two as a consequence of display effects.
The wake flow dynamics were characterized by means of a frequency analysis. The time-resolved vector data was converted into the frequency domain by FFT at each vector position. The Welch windowing was applied for amplitude enhancement, see Welch (1967). The size of one Welch window was 1 s (i.e. 4000 samples) and the overlap was 75 %.

PSP measurements

Data acquisition

The drift of the flow temperature was the major challenge that must be handled for accurate iPSP measurements. The precise knowledge of the model temperature was mandatory due to the strong temperature dependence of pc-PSP. Figure 6.11 shows an example of the variation of the model temperature (*blue*) and the static base pressure (*black*) during a wind tunnel run.

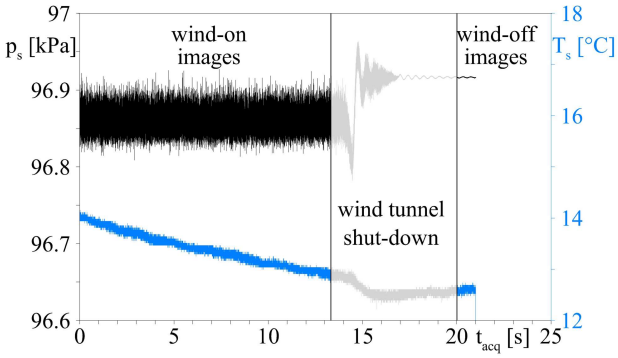

Fig. 6.11.: Typical behavior of the static base pressure (*black*) and the model temperature (*blue*) during a wind tunnel run; The image acquisition sequences for capturing the wind-on and wind-off images are included.

The iPSP intensity image and sensor data acquisition was started after the wind tunnel has reached steady conditions. All data were recorded as a continuous time series. The wind-on/wind-off data extraction from the time series is exemplary sketched in Figure 6.11. All individual components already worked in loop- or continuous mode in order to ensure balanced operating conditions.
All sensor signals were recorded with a *DEWE-50-PCI* parallel scanning device. The sampling rates were 10,000 Hz and 1,000 Hz for the pressure and the temperature sensors, respectively. The temperature measurements were conducted by means of a 4-wire RTD setup. The accuracy was $\Delta T \leq 0.1\,\mathrm{K}$. The uncertainty during the pressure scanning was $\Delta p \leq 10\,\mathrm{Pa}$.
A dark current compensation of the camera was made prior of each test in order to avoid a potential drift of the sensor noise. Dark intensity images were additionally taken after the final wind-off image. They were used to correct both, the wind-on and the wind-off images. The dark frame correction was mainly done in order to compensate a potential characteristic pattern of the CMOS sensor. There was no significant background light. Hence no classic dark-frame correction was needed.
The iPSP sample rates were varied according to the free-stream velocity in order to resolve the same reduced frequencies as in the PIV investigations and to check the performance of the iPSP system at various acquisition frequencies. The sample rates were chosen with $f_{\mathrm{s,iPSP}} = [1; 2; 4]\,\mathrm{kHz}$ according to Table 6.1. It was necessary to crop the frame size at higher frame rates in order to keep the proposed image acquisition procedure.

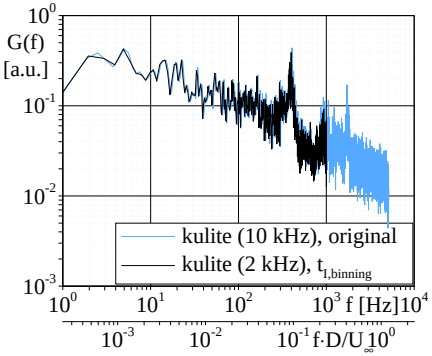

Fig. 6.12.: Comparison of the power spectral density $G(f)$ from a raw pressure transducer signal (*blue*) and from an iPSP-adapted transducer signal (*black*).

Data conditioning

The raw signal of the pressure transducers (10 kHz) was artificially binned according to the corresponding iPSP integration times in order to compare signals with the same resolution in time. The transducer samples that were recorded during the integration time of the camera were averaged. Figure 6.12 compares the power spectral density G of a raw (*blue*) and a binned pressure transducer signal (*black*). The noise from the raw signal was slightly reduced as a consequence of the binning whereas all characteristic features were kept.

Main PSP evaluation

About 1,000 wind-off images, 1,000 dark images and 16,000 – 24,000 wind-on intensity images were available for the final data evaluation in *IRES*. The data evaluation of 16,000 PSP signal images took about 2 h on 12 parallel CPUs.
The in-situ correction was applied automatically to the results of the base measurements. A fit function was created for each instantaneous pressure mapping that linked the pressure values from the raw PSP results with the desired surface pressures at the positions of the four transducers. The fit function was applied to the entire pressure map. The wake results were corrected by means of an average fit function that was derived from the base data. This became necessary because the sting support incorporated no pressure transducer for in-situ correction. Each instantaneous pressure mapping was projected on a specific structured grid with resolutions of 41×220 surface elements (sting mesh) and 173×50 surface elements (base mesh) according to Fig. 6.13.

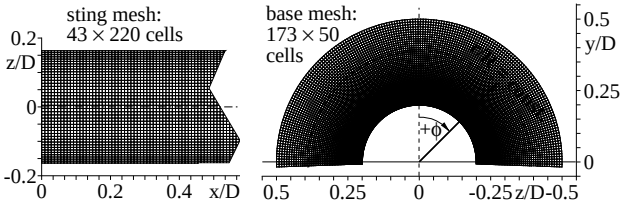

Fig. 6.13.: Data projection grids for the iPSP measurements showing the mesh for the wake result (*left*) with a resolution of 41×220 cells and the mesh for the base results (*right*) with 173×50 structured surface elements.

Post-processing

All subsequent data processing was performed on the grid. The pressure data was converted into the frequency domain by FFT in order to identify characteristic frequencies in the time-signal. The power spectral density $G(f)$ of the pressure signals from the transducers and from iPSP were computed by using the Welch algorithm in order to enhance the spectral amplitudes (similar to the PIV data processing). The cut-off frequencies which define the corresponding frequency resolutions are given by $f_c = 0.5 \cdot f_s$. They were $f_c = [512; 1{,}024; 2{,}048]$ Hz for the corresponding sampling frequencies $f_s = [1{,}000; 2{,}000; 4{,}000]$ Hz according to Table 6.1. The length of a Welch window was 1 s (i.e. 1,000 samples for a sampling rate of 1 kHz). The window overlap was 75 %.
The convention:

$$\sigma^2 = \int_0^\infty f \cdot G(f) d[log(f)] = c_{p,rms}^2 \tag{6.4.1}$$

proposed by Owen (1958) was used for the display and the discussion of the pressure spectra. The notation describes the total energy of a peculiar frequency band. It artificially amplifies small characteristic pressure fluctuations in the spectra which essentially determine characteristic buffet loads. The power spectrum is normalized with the local frequency and the pressure fluctuation (squared RMS value). The spectra can be plotted in linear-logarithmic scales as a consequence from this consideration.
The integrated values of the pressure fluctuation coefficient $c_{p,rms}$ were computed by:

$$c_{p,rms} = \sqrt{\overline{p'^2}}/q_\infty \tag{6.4.2}$$

Here, p' is the pressure fluctuation and q_∞ is the dynamic pressure. One scientific goal was the identification of characteristic base pressure modes that have a dominant radial distribution. This analysis was possible as a consequence of the structured data projection grids. The pressure data were extracted at a constant radius r/R from the base grid

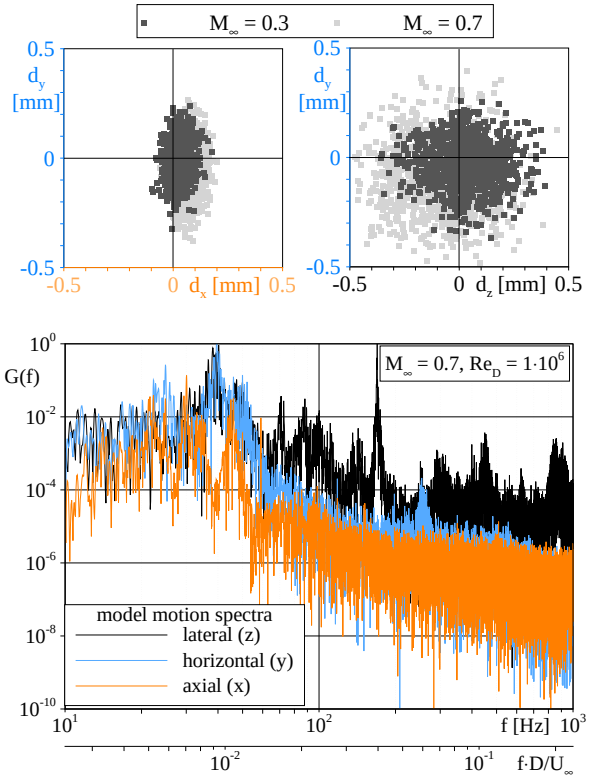

Fig. 6.14.: Model characteristics in the axial (*orange*), the horizontal (*blue*) and the lateral (*black*) direction. *Top*: Model vibration amplitudes at $M_\infty = [0.3; 0.7]$; *Bottom*: characteristic model shaking spectra at $M_\infty = 0.7$.

or at a certain constant position z/D from the wake grid. These pressure signals were analyzed using the FFT. The spatial frequencies were converted into physical dimensions by means of the grid spacing factor that was 1.05 cells/$^\circ$ or 2 cells/mm, respectively, in order to identify dominant spatial wavelength that characterize the extension of coherent pressure modes.

6.5. Model characteristics

The vibration of the model and the model's resonance spectrum were investigated during two wind tunnel runs at $M_\infty = [0.3; 0.7]$ test conditions. A registration marker on

the surface was tracked with a sample rate of 2 kHz in order to resolve the model motion. The data was acquired using the experimental setups from the iPSP measurements. The model motion amplitudes and characteristic spectra in the axial flow direction (x), in the horizontal plane (y, yawing) and in the lateral plane (z, pitching) are summarized in Fig. 6.14. The motion amplitudes are about 0.5 mm at its maximum. This corresponds to a shift of about 5 px in the intensity images in combination with the optical magnification. The power spectra $G(f)$ in all three dimensions revealed dominant peaks around the models resonance frequency at $f = 39.2\,\mathrm{Hz}$. It was also shown that the amplitudes of the lateral motion are approximately two orders of magnitude higher compared to the remaining spectra. In this case, the measurement sequence was performed with setup 2 (camera attached to the wind tunnel wall). The spectrum of the model was obviously superimposed by the vibration of the wind tunnel. Hence, characteristic frequencies around $f = [39.2, 170]\,\mathrm{Hz}$, which were generated by the model setup, and frequencies around $f = [20, 100]\,\mathrm{Hz}$, which caused by the wind tunnel itself, must not be interpreted as dominant flow frequencies in the latter discussion of the results.

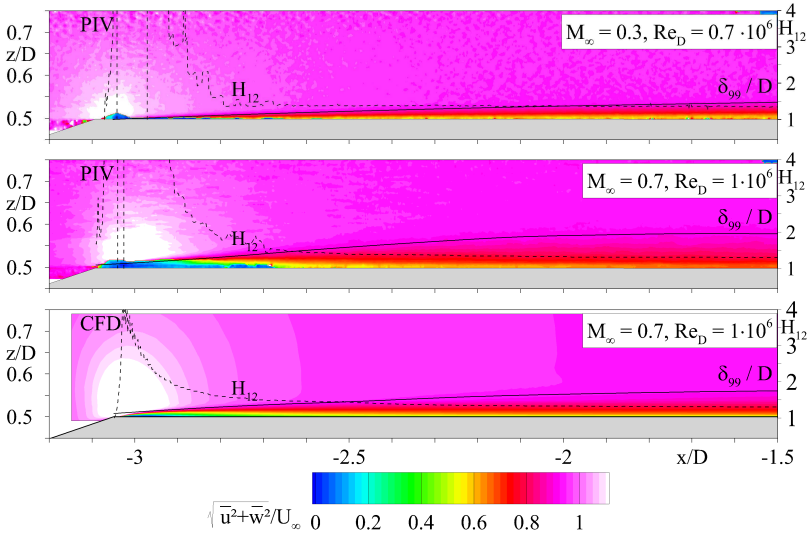

Fig. 6.15.: Boundary layer topology in the experimental (*top* and *middle*) and in the numerical data (*bottom*); the absolute mean velocity is color-coded; the development of the boundary layer height δ_{99}/D and the form factor H_{12} is highlighted by the *solid* and *dashed* slopes, respectively.

6.6. PIV Results

6.6.1. Boundary layer topology

The topology of the boundary layer is shown color-coded in Figure 6.15. The normalized absolute velocity fields from the ensemble-averaged TR-PIV data are displayed. A comparison was made with the two-dimensional numerical simulations at $M_\infty = 0.7$. The boundary layer height δ_{99} grows up to 3.8 mm for $M_\infty = 0.3$ and up to 5.6 mm for $M_\infty = 0.7$ at the position $x/D = -1.5$. The empirical boundary layer shape factor H_{12} reflects the topology of the boundary layer profile. It is calculated from the ratio between the displacement thickness δ^* and the momentum thickness Θ. A laminar, a turbulent and a separated boundary layer is present for $H_{12} \approx [2.6; 1.3; \geq 4]$, respectively. The numerical results predicted a flow separation in the vicinity of the junction between the nose cone and the cylindrical part of the model as indicated by the shape factor. A laser light reflection partially impeded the evaluation of the experimental results at this posi-

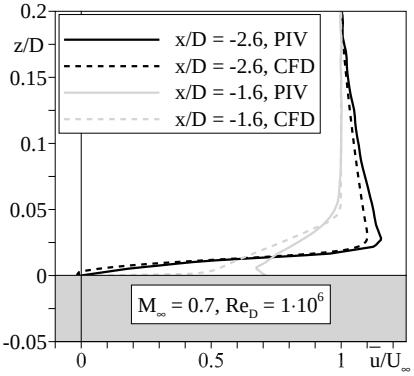

Fig. 6.16.: Comparison of the boundary layer profiles at $x/D = -2.6$ (*black*) and $x/D = -1.6$ (*gray*) between experimental (*solid*) and numerical data (*dashed*) for the Mach number $M_\infty = 0.7$.

tion. Unfortunately, the reflection extended over 20 mm so that the expected separation bubble could not be resolved in the experiments. The slope of the shape factor revealed that the boundary layer is turbulent from $x/D \approx -2.5$ in both, the experimental and the numerical data.
A comparison of the experimental and numerical boundary layer profiles at $x/D = -2.6$ (*black*) and $x/D = -1.6$ (*gray*) is displayed in Fig. 6.16. The profiles from the experimental data were averaged over 6 interrogation windows in the axial direction ($6 \cdot 0.0984$ mm) for smoothing. The very good agreement of the profile shapes validated the conclusions of the turbulent boundary layer state and the general topology. The entire boundary layer height was resolved within 12 px in the experiments. The optical magnification of the experimental setup as well as the lack of tracer particles in the near-wall region impeded the PIV evaluation down to the wall. The investigation of the near-wall region down to the viscous sub layer requires a higher optical magnification of about $10 - 20 : 1$, a higher seeding density and a more sophisticated data evaluation technique as reported in Kähler et al. (2012b).

6.6.2. Wake flow topology

The normalized velocity magnitude in the wake is shown color-coded for both Mach numbers in Fig. 6.17 in comparison to the 2D-RANS simulations at $M_\infty = 0.7$. A distinct recirculation vortex with a clear reattachment location established in the wake. A secondary counter-rotating vortex was clearly resolved in the corner between the base

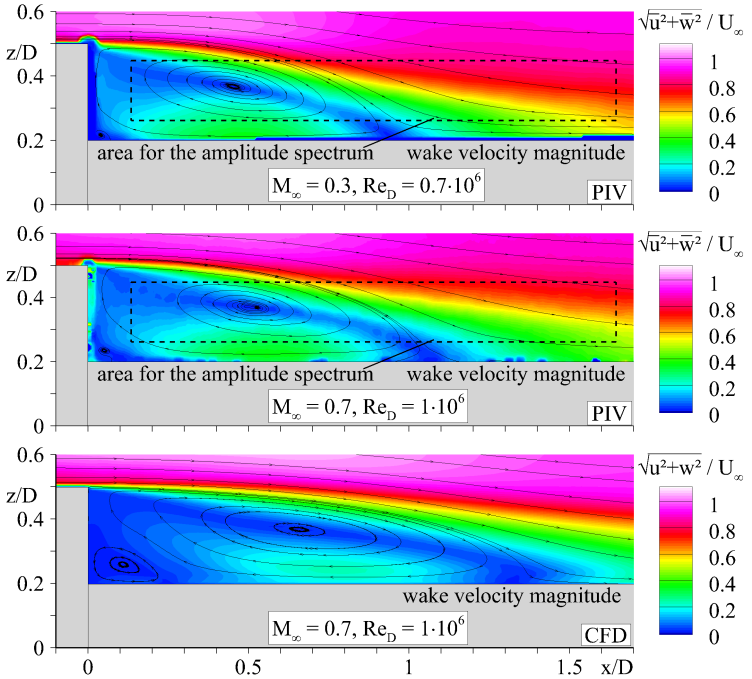

Fig. 6.17.: Normalized wake velocity magnitude from PIV at $M_\infty = 0.3$ (*top*), $M_\infty = 0.7$ (*middle*) and from 2D-RANS simulation at $M_\infty = 0.7$ conditions (*bottom*).

and the sting support by means of the RANS simulation as indicated by the stream lines. This vortex was also confirmed in the PIV results but the spatial resolution of the vector field is too low to characterize its extension precisely.

The criteria for the estimation of the reattachment lengths was $u_{ax} = 0$. Hence, the reattachment lengths were estimated with $l_r \approx (0.98 \pm 0.01)\, x/D$ and $l_r \approx (1.13 \pm 0.01)\, x/D$ at $M_\infty = 0.3$ and $M_\infty = 0.7$, respectively. The uncertainty was given from the resolution of the vector field. The size of the recirculation area is over-predicted by about 15 % in the RANS simulations. Here, reattachment occurs at $l_r \approx (1.332 \pm 0.001)\, x/D$. This discrepancy is mainly caused by a mismatch of the turbulence production and dissipation terms between the experiments and the simulations. The mismatch assumption was also confirmed by the topology of the turbulent kinetic energies ($k = 0.5 \cdot (\overline{u'^2} + \overline{w'^2})$) as shown in Fig. 6.18. The maximum values of k differ by a factor of 1.5 between the simulations and the experiments (note the scaling of the color bars in Fig. 6.18). Nev-

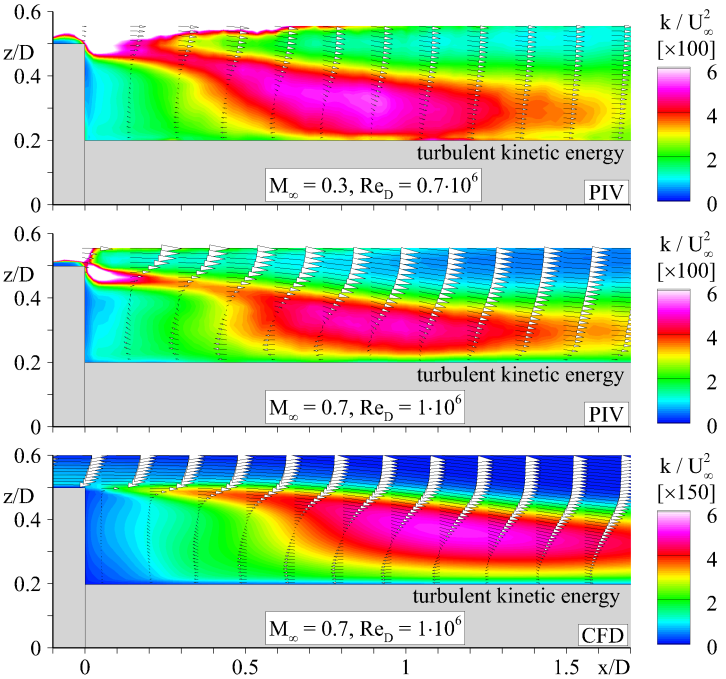

Fig. 6.18.: Normalized turbulent kinetic energy from PIV at $M_\infty = 0.3$ (*top*), $M_\infty = 0.7$ (*middle*) and from 2D-RANS simulation at $M_\infty = 0.7$ conditions (*bottom*).

ertheless, the topology of the wake flow and the absolute values of the wake velocity magnitude compared well with each other. The thickness of the shear layer decreased with increasing Mach number. An overall broadening of the shear layer towards the reattachment location indicated enormous unsteady fluctuations in this region and a strong momentum transfer between the outer free stream flow and the recirculation area caused by vortex shedding. The amplification of k in the vicinity of the shear layer separation point at the base was introduced artificially. It was the consequence of spurious vectors which were caused by an instationary oil droplet at this position.

6.6.3. Coherent wake dynamics

The velocity perturbation $u_i' = u_i(t) - \overline{u_i}$ was computed for every instantaneous vector field. It is a characteristic measure for shedding vortices. The amplitude spectrum of the

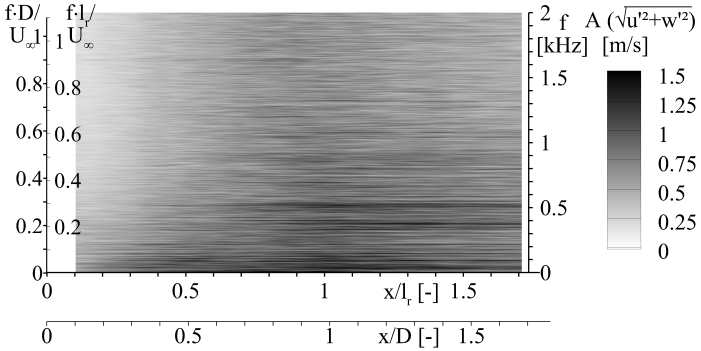

Fig. 6.19.: Local amplitude spectrum of the velocity perturbation magnitude with respect to the axial wake position at $M_\infty = 0.3$.

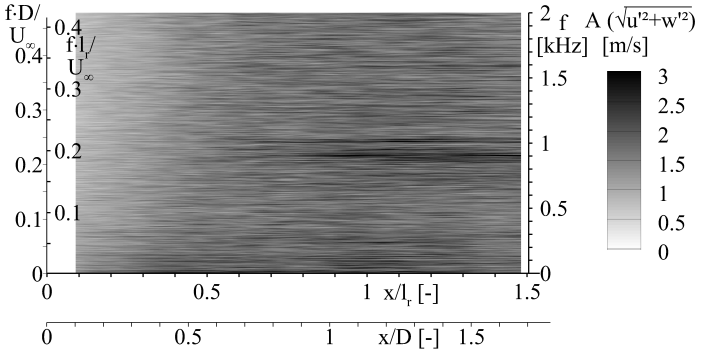

Fig. 6.20.: Local amplitude spectrum of the velocity perturbation magnitude with respect to the axial wake position at $M_\infty = 0.7$.

velocity perturbation magnitude was calculated at each individual vector location within the dashed box in the wake region that was highlighted in the previous figures. The results were averaged vertically in order to increase the SNR. The local amplitude spectra with respect to the axial position in the wake are displayed in the Figures 6.19 and 6.20 for $M_\infty = 0.3$ and $M_\infty = 0.7$, respectively. Both spectra reveal two major characteristic features: on the one hand, a region of low dynamic range appears in the vicinity of the base up to $x/l_r \approx 0.5$. Apparently, no coherent structures of a distinct frequency were resolved with PIV in this area. A formation of certain dominant frequencies is evident

beyond $x/l_r > 0.5$. The peak locations in the spectra are located around 400-500 Hz at $M_\infty = 0.3$ and around 900-1000 Hz for $M_\infty = 0.7$. These peaks partially correspond to the expected frequencies of dominant vortex shedding at a reduced frequency around $f \cdot D/U_\infty = 0.21$.

6.6.4. Summary of the PIV experiments

The results of the PIV measurements revealed the following perceptions:

- The state of the boundary layer is fully turbulent when it separates from the base.
- The agreement of the flow topology and the velocity magnitude between the experimental results and the 2D/3D-RANS calculations was very good. There was a discrepancy between the turbulence production terms in the Reynolds-stress turbulence model and the turbulence level in the wind tunnel that had a significant effect on the wake reattachment position. This location was over-predicted by about 15 % in the numerical results.
- The strongest unsteady effects were identified at about 80-90 % upstream of the reattachment position as examined from the topology of the turbulent kinetic energy.
- The presence of expected dominant shedding frequencies around 400 Hz at $M_\infty = 0.3$ and around 900 at $M_\infty = 0.7$ was confirmed by the PIV measurements. Nevertheless, the amplitudes were very noisy and only accounted for very strong fluctuations.

The PSP measurements should preferentially help to resolve the flow dynamics which are expected to have a larger dynamic range as indicated by means of the PIV results.

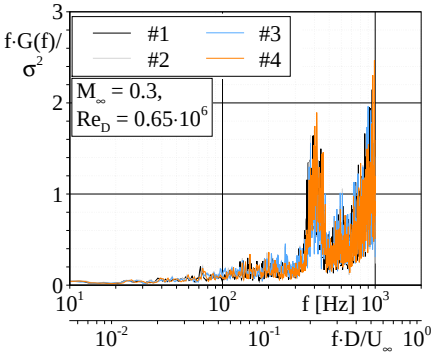

Fig. 6.21.: Comparison of the base buffet spectra $f \cdot G(f)/\sigma^2$ of the four active pressure transducers inside the base located at $r/R = [0.45; 0.52; 0.85; 0.95]$.

6.7. PSP results

6.7.1. Comparison: iPSP vs. pressure transducer

A comparison between the buffet spectra from the conventional pressure transducers and the results of the iPSP measurements was initially made in order to ensure that frequencies which were resolved with iPSP reliably represent the flow characteristics. Figure 6.21 shows the similarity of all four pressure transducers. The 3rd sensor located at $r/R = 0.52$ was used as a reference for the iPSP results in the following discussions. The static base pressures at the reference transducer during a wind tunnel run were $p_s = (158.283 \pm 0.538)$ kPa at $M_\infty = 0.3$ and $p_s = (101.721 \pm 0.784)$ kPa at $M_\infty = 0.7$. These pressure fluctuations led to intensity changes of 0.2-0.4 % in the iPSP images.
Figure 6.22 shows a comparison of the base buffet spectra from the pressure transducers (*dashed*) and the spectra from the iPSP signals (*solid*) at both test Mach numbers. The iPSP data was extracted from the base grid in the vicinity of the reference pressure transducer for this comparison. The spectra at different iPSP sample rates are shown color-coded in the figures. The good agreement between the spectra in both, the amplitude and the position of characteristic frequencies, showed that iPSP was capable to resolve the flow phenomena precisely. A dominant peak established around $f \approx 405$ Hz and a second, wider one around $f \approx 870$ Hz for $M_\infty = 0.3$. The first peak confirmed the expected frequency of characteristic vortex shedding at a reduced frequency of $f \cdot D/U_\infty = 0.21$. The wider peak ought to represent its higher harmonic, as already measured in Scharnowski and Kähler (2011). At $M_\infty = 0.7$, dominant peaks

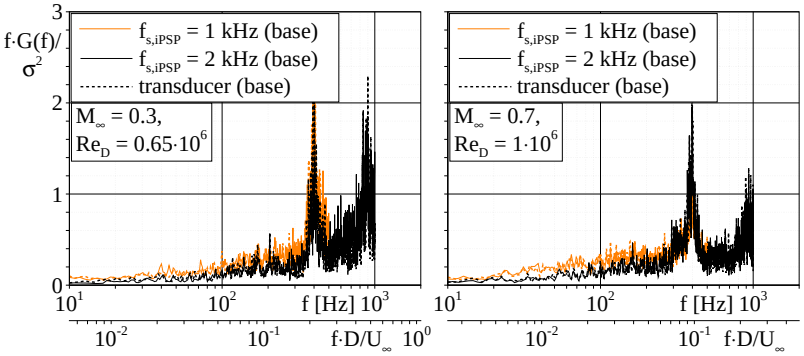

Fig. 6.22.: Comparison between the base buffet spectra from the iPSP signals (*solid*) and from the pressure transducers (*dashed*); the iPSP sample rates were $f_{s,iPSP} = 1\,\text{kHz}$ (*black*) and $f_{s,iPSP} = 2\,\text{kHz}$ (*orange*); *Left:* $M_\infty = 0.3$; *Right:* $M_\infty = 0.7$.

formed around $f \approx 400\,\text{Hz}$ and around $f \approx 900\,\text{Hz}$. The peak around $f \approx 900\,\text{Hz}$ corresponded to the expected frequency of characteristic vortex shedding. The peak around $f \approx 400\,\text{Hz}$ reflected one harmonic of the wind tunnel perturbation that was discussed earlier. The dominant amplitudes are 10-15 % lower at $M_\infty = 0.7$. They might be amplified by the higher turbulence level and the perturbations of the hydraulic system at the lower test Mach number.

6.7.2. Base flow topology

Mean pressure distribution

The ensemble-averaged base pressure distributions are shown in the Figures 6.23 and 6.24 for $M_\infty = 0.3$ and $M_\infty = 0.7$, respectively. The view from the rear is presented in polar coordinates whereas $\Phi = 0^\circ$ represents the positive $y-$axis in the global coordinate system. The gray filled areas cover screws and the pressure transducers. No iPSP signal was available at these positions. A fairly constant static pressure distribution developed at the base as it was expected from the RANS simulations. The pressure minimum is located at about 20 % of the base height. A pressure change towards the sting support ($r/R = 0.4$) is caused by the secondary vortex rotating in the junction between the sting and the model base. Its asymmetric distribution, especially at $M_\infty = 0.7$, indicated a potential oblique oncoming flow. This might be caused by a slight

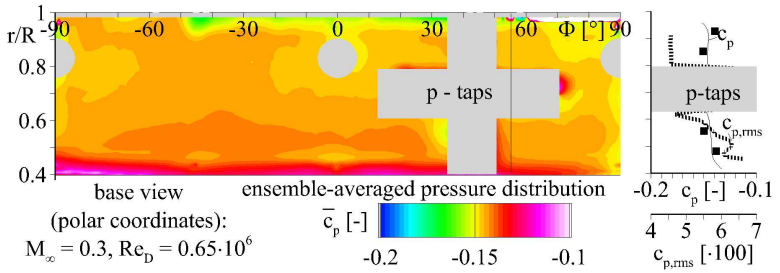

Fig. 6.23.: *Left:* ensemble-averaged base pressure distribution at $M_\infty = 0.3$ in polar coordinates $(\Phi, r/R)$; *Right:* line plots of c_p and $c_{p,rms}$ extracted at $\Phi = 55°$ in comparison with the pressure transducer results (*symbols*).

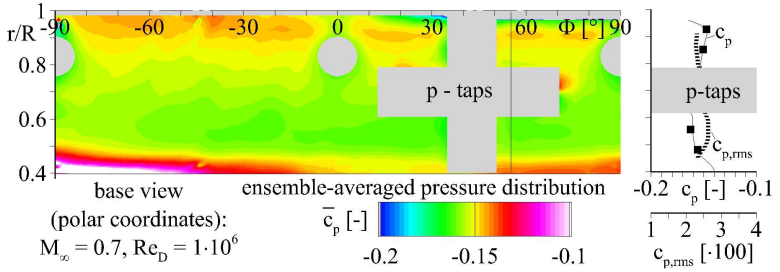

Fig. 6.24.: *Left:* ensemble-averaged base pressure distribution at $M_\infty = 0.7$ in polar coordinates $(\Phi, r/R)$; *Right:* line plots of c_p and $c_{p,rms}$ extracted at $\Phi = 55°$ in comparison with the pressure transducer results (*symbols*).

sting bending as a consequence of strong aerodynamic forces. Unfortunately, the four static installation pressure ports on the cylindrical part of the model indicated no noticeable pressure difference.

A quantitative comparison between the pressure transducer values and iPSP is done on the right-hand side of each figure. The pressure coefficient c_p and the pressure fluctuations $c_{p,rms}$ were compared. The line plots represent the iPSP data and the symbols show the transducer data. The iPSP data was extracted at $\Phi = 55°$. The values of $c_{p,rms}$ are nearly doubled in case of the low Mach number compared to the transonic one. This was expected as a consequence of the higher wind tunnel turbulence level at $M_\infty = 0.3$. The highest fluctuations occur in the vicinity of the pressure minimum. The measurement uncertainty was assessed by means of all four pressure transducers which were

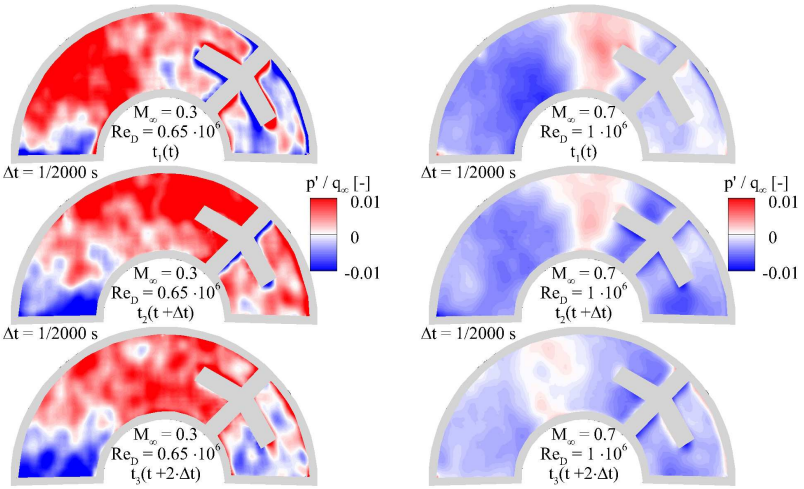

Fig. 6.25.: Normalized base pressure fluctuations p'/q_∞ at three consecutive time steps ($\Delta t = 5 \cdot 10^{-4}$ s) for $M_\infty = 0.3$ (*left*) and for $M_\infty = 0.7$ (*right*).

used for the in-situ correction. The deviations between the raw and the in-situ corrected results were examined during the *IRES* evaluation. They were at $8-10\,\%$ -lower at $M_\infty = 0.7$ due to a stronger pressure gradient. These deviations were slightly higher but still in good agreement with the expectations made by the temperature distribution from CFD. Paint contamination and aging played an additional role and increased the uncertainty. The final deviations between the transducers and the corrected iPSP signals were $\Delta c_p = 0.015$ for $M_\infty = 0.3$ and $\Delta c_p = 0.009$ at $M_\infty = 0.7$. The uncertainty was higher for $M_\infty = 0.3$ as a consequence of the higher static pressure in the test section, the lower pressure fluctuations and the higher turbulence level.

Pressure fluctuations

An impression of the time-dependent topology of the base pressure fluctuation at three consecutive time steps can be received by means of Fig. 6.25. The starting time step was chosen randomly. As already mentioned, the fluctuation amplitudes are higher for $M_\infty = 0.3$. The distribution of the pressure fluctuation events appeared staggered at the lower Mach number. Their distributions seemed much smoother at $M_\infty = 0.7$. The occurrence of high ($p' > 0$) and low ($p' < 0$) pressure fluctuation events was statistically investigated. Each instantaneous pressure mapping was segmented into

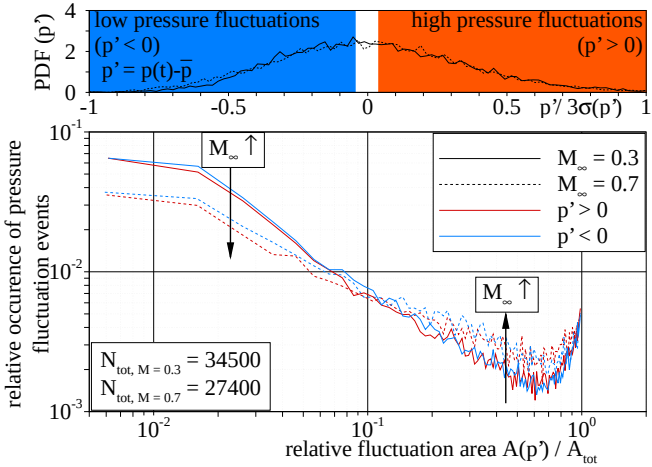

Fig. 6.26.: Statistical evaluation of the coincidence between the size of low ($p' < 0$, *blue*) and high ($p' > 0$, red) pressure fluctuation events and their relative number of occurrence.

areas of low and high pressure fluctuations. Therefore, the individual probability-density functions (PDF) of the pressure signals were normalized with the 3σ quantiles ($3\sigma = [1.61; 2.35]$ kPa) for $M_\infty = 0.3$ and $M_\infty = 0.7$, respectively. The normalized PDFs are displayed on top of Figure 6.26 for both test Mach numbers. The segmentation boundaries for the pressure mappings were chosen according to the color-shaded regions in these PDFs. An algorithm was used that binarized the segmented pressure mappings and extracted the area information of the detected events. The area of the individual event $A(p')$ was normalized with the base area that was covered with iPSP A_{tot}. The relative fluctuation area is plotted on the abscissa in the lower plot of Figure 6.26. The number of occurrence of the high and low pressure events was normalized by the total number of detected events for each Mach number. Their values are plotted along the ordinate. The plot was cropped at $A(p')/A_{\text{tot}} < 6 \cdot 10^{-3}$ due to a large number of smaller events which were introduced into the results by the size of the spatial filter. The results confirm the visual impression that more smaller pressure events occurred at $M_\infty = 0.3$ whereas large-size pressure fluctuations dominated at $M_\infty = 0.7$. It is expected that these characteristics were not a Reynolds number effect because of the similarity of the test Reynolds numbers. It might be caused by the flow quality at low subsonic conditions as previously mentioned.

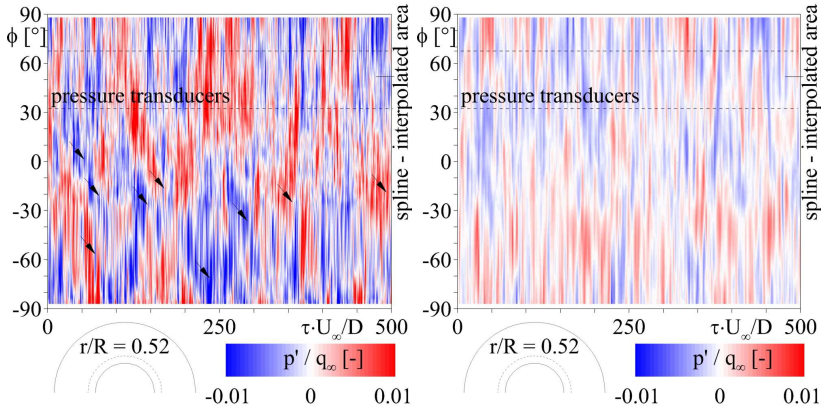

Fig. 6.27.: Space-time correlation plot of the normalized pressure fluctuation p'/q_∞ at $M_\infty = 0.3$ (*left*) and $M_\infty = 0.7$ (*right*) extracted from the base at $r/R = 0.52$ for 500 reduced time-steps $\tau \cdot U_\infty/D$; the black arrows indicate pattern convection with a reduced convection rate of $f_c \cdot U_\infty/D = 0.079$.

Coherent pattern convection

The pressure fluctuation signal was extracted from the base at the radius where the reference pressure transducer was located ($r/R = 0.52$) in order to identify dominant pattern convection rates. Figure 6.27 shows the corresponding space-time correlation at 200 reduced time-steps $\tau \cdot U_\infty/D$ for both test Mach numbers. The signal was interpolated at the positions of the pressure transducers (within the *dashed* boundaries) using a cubic spline due to the absence of iPSP information at this position. The visual identification of pattern convections was possible for $M_\infty = 0.3$ by means of this plot due to sufficiently high sample rates. The estimated reduced convection rates were $f_c \cdot U_\infty/D \approx 0.079 \pm 0.01$, as indicated by the black arrows. This corresponds to radial convection rates of $\omega = 2\pi f_c \approx 950\,\text{rad/s}$ or about 150 Hz. A peak at 150 Hz was also present in the base buffet spectra that were discussed earlier. Unfortunately, this frequency collided with a characteristic frequency from the experimental setup. In the case of $M_\infty = 0.7$, the sample rate was too low for an estimation of convection rates by this analysis.

The estimated pattern convection rates were confirmed by means of a two-point correlation, compare Hudy et al. (2007). Therefore, the time domain of the signal at each radial position Φ from Figure 6.27 was cross-correlated with the signal at $\Phi = 0°$. The signal had to be super-sampled by a factor of 5 for this analysis in order to avoid peak-locking. Coherent convection rates can be identified if there is a certain correlation

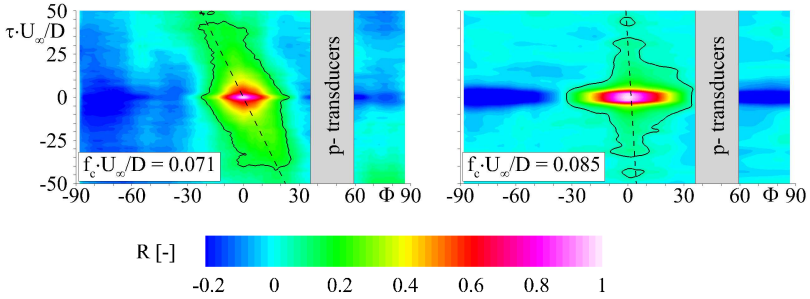

Fig. 6.28.: Contour map of the two-point cross-correlation between all base pressure fluctuation signals along $r/R = 0.52$ and the reference signal at $\Phi = 0^\circ$ at $M_\infty = 0.3$ (*left*) and $M_\infty = 0.7$ (*right*); the pattern convection $f_c \cdot U_\infty/D$ is estimated from the inclination of the correlation peak (*dashed*); the segmentation threshold was 0.1 (*black*).

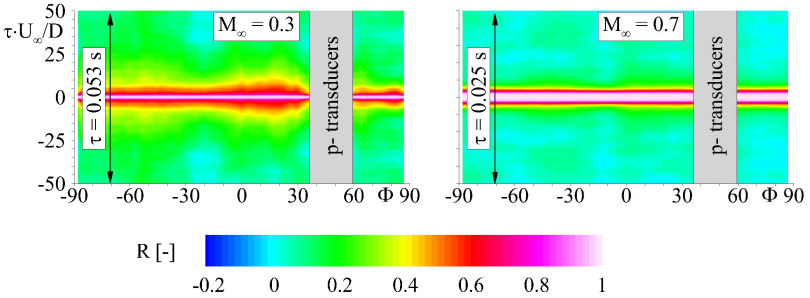

Fig. 6.29.: Contour map of the auto-correlation coefficient R for all base pressure fluctuation signals along $r/R = 0.52$ at $M_\infty = 0.3$ (*left*) and $M_\infty = 0.7$ (*right*).

between the reference signal and the remaining ones. The cross-correlation result is shown in Figure 6.28 for both Mach numbers at 100 reduced time steps $\tau \cdot U_\infty/D$. Both plots show a distinct correlation between the reference signal and the signals in the immediate neighborhood. The convection rate is characterized by the inclination of the correlation peak, according to Hudy et al. (2007). The correlation map was segmented with *Matlab*™ using thresholds between 0.1 and 0.3, as indicated by the black boundary. An elliptical fit was applied to the segmented correlation map in order to estimate the peak orientation.

Coherent pattern convection rates of $f_c \cdot U_\infty/D = [0.071; 0.085] \pm 0.02$ were estimated from this investigation at $M_\infty = 0.3$ and $M_\infty = 0.7$, respectively. The uncertainty was

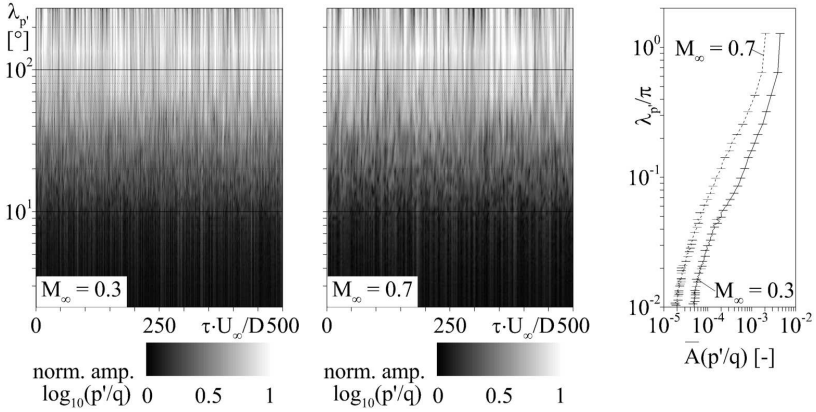

Fig. 6.30.: Spatial wavelength spectra ($\lambda_{p'} \propto 1/f$) of base pressure modes for $M_\infty = 0.3$ (*left*) and $M_\infty = 0.7$ (*middle*); the signal was extracted at $r/R = 0.52$ for 500 reduced time-steps $\tau \cdot U_\infty/D$; *Right:* time-averaged wavelength spectra and the standard deviations.

given by the corresponding results with different segmentation thresholds. The values for $M_\infty = 0.3$ are in good agreement and confirm the pattern convection rates as they were visually detected before.
Mabey (1972) proposed the auto-correlation of characteristic signals for the identification of dominant time scales in the flow. The evaluation was performed in a similar manner than the one from above. The super-sampled time signals of the pressure fluctuations were self-correlated at each position Φ. The auto-correlation maps are presented in Figure 6.29 for both Mach numbers. A homogeneous distribution of the time scales in the separated base flow is expected if there are no triggered scales in the flow. The actual distribution is homogeneous over a wide radial range. Around $\Phi = 0°$ (the direction of the horizontal y - axis) the peak is spreading slightly for $M_\infty = 0.3$. This indicates a small variation in the dominant time scales. It might be caused by interferences between the model and the vertical wind tunnel wall as a consequence of the rectangular (non-symmetric) cross-section.

Coherent pattern wavelength

Finally, the pressure fluctuation signal from Figure 6.27 was analyzed in order to identify coherent pattern wavelengths. Large-eddy simulations that were performed by project partners indicated an instantaneous mode-like 60° distribution of base pressure

fluctuations, compare Statnikov et al. (2012). The space domain of each instantaneous pressure fluctuations signal was converted by means of FFT. The spatial wavelength of a pressure mode $\lambda_{p'}$ is proportional to its inverted spatial frequency. The spatial wavelengths of the corresponding signals are presented in Figure 6.30 for both Mach numbers at 500 reduced time steps. The right-hand-side shows an averaged wavelength spectrum and the corresponding standard deviations.
Structures with large spatial wavelengths dominate the spectra for both Mach numbers. The formation of pressure modes with a preferred 60°-distribution could not be confirmed by this analysis. However, a mode-like appearance of p' is somehow present. It can be concluded from both, Figure 6.27 and Figure 6.30, that the strongest pressure fluctuations modes seemed to have dominant wavelengths in the range of $100^\circ \leq \lambda_{p'} \leq 200^\circ$.

6.7.3. Wake flow topology

The comparison between the pressure transducers and iPSP from the previous section showed that iPSP is capable to resolve small pressure fluctuations with high frequencies precisely and reliably. This benchmark was shown in advance because the iPSP wake data (discussed in the following) could not be corrected with pressure transducer signals due to their absence within the rear sting support.

Mean pressure distribution

Figures 6.31 and 6.32 show a contour map of the ensemble-averaged wake pressure distribution at $M_\infty = 0.3$ and $M_\infty = 0.7$ acquired with 2 kHz and averaged from 16384 wind-on samples. The line plots of c_p and $c_{p,rms}$ in the upper part were extracted at $\Phi = -200^\circ$ (black trace in the surface pressure plot). The axial coordinate was normalized with the reattachment length from PIV which were $l_r = [0.98; 1.13]\,x/D$ at $M_\infty = [0.3; 0.7]$. The regular dot structure in the pressure map (especially at $M_\infty = 0.3$) originated from the registration markers.
The pressure difference Δc_p as well as the absolute pressure fluctuation coefficient $c_{p,rms}$ is nearly doubled for $M_\infty = 0.3$ compared to the transonic test case. This might be the consequence of the high turbulence level and the amplification of perturbations as already assumed in the base flow results. The line plots of c_p and $c_{p,rms}$ are compared with data from literature in the case of $M_\infty = 0.7$, compare Deprés et al. (2004). Deprés et al. (2004) acquired their data on a comparable model by means of unsteady pressure transducers at $M_\infty = 0.85$. Their model was fixed in the test section using a strut. Hence, it could be equipped with a cylindrical nozzle of length $1.2D$ instead of a sting support. The good agreement in both, c_p and $c_{p,rms}$, validated the presented iPSP results and the data handling in absence of pressure transducers for an in-situ correction.

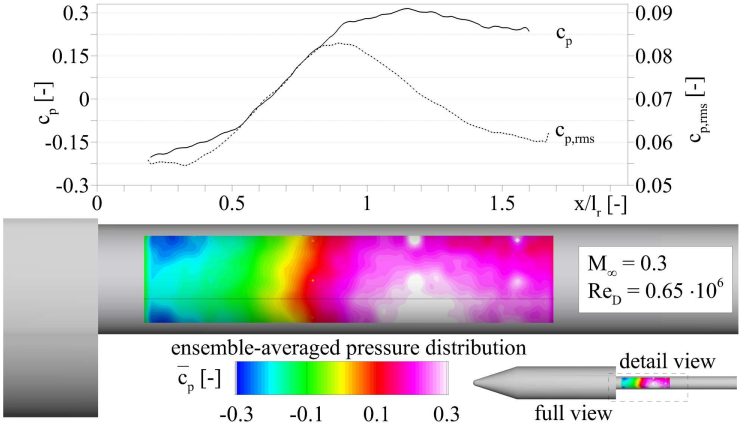

Fig. 6.31.: Contour plot of the ensemble-averaged wake surface-pressure distribution $\overline{c}_p$ at $M_\infty = 0.3$ and line plots of c_p and $c_{p,rms}$ extracted at $\Phi = -200^\circ$ (*black* trace).

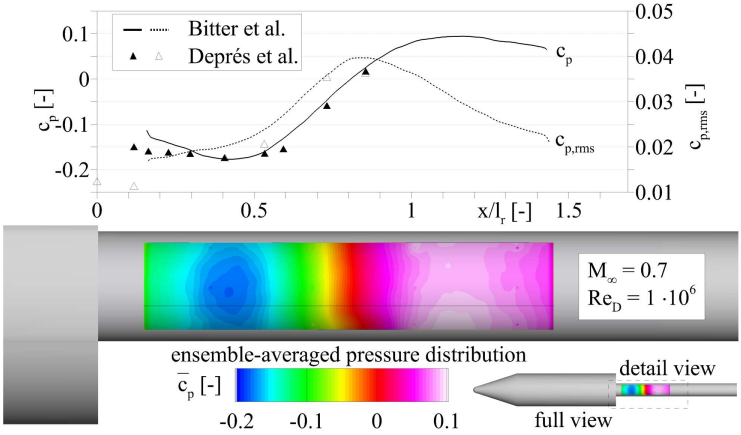

Fig. 6.32.: Contour plot of the ensemble-averaged wake surface-pressure distribution $\overline{c}_p$ at $M_\infty = 0.7$ and line plots of c_p and $c_{p,rms}$ extracted at $\Phi = -200^\circ$ (*black* trace); comparison with data from Deprés et al. (2004) (*triangles*).

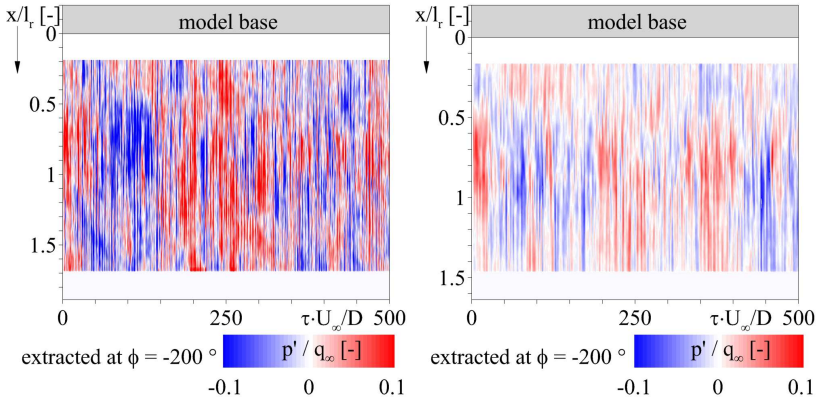

Fig. 6.33.: Space-time correlation plot of the normalized pressure fluctuation p'/q_∞ at $M_\infty = 0.3$ (*left*) and $M_\infty = 0.7$ (*right*) extracted from the wake at $\Phi = -200°$ for 500 reduced time-steps $\tau \cdot U_\infty/D$.

The pressure distribution at $M_\infty = 0.7$ exhibited the clear formation of a vortex core around $x/l_r \approx 0.4$ as indicated by the pressure minimum. It was examined by other authors that the location of the highest pressure fluctuations $c_{p,rms}$ is located about 25 % upstream of the mean reattachment length, compare Hudy et al. (2007) or Deck et al. (2007). These result were confirmed by the iPSP results. The maximum wake pressure $c_{p,max}$ was located about 10 % downstream of the reattachment position. Since the topology of the pressure distribution established as expected in the averaged results from $M_\infty = 0.7$, the wake flow seemed somehow triggered and not yet fully developed at $M_\infty = 0.3$. The major indicator for this assumption was the formation of locally predefined low pressure regions in the topology at the lower Mach number. These low pressure regions were noticeable even in the ensemble-averaged results, as indicated by the deep blue areas in the pressure map of $M_\infty = 0.3$. The flow triggering might also be the consequence of the flow quality in the wind tunnel at this minimum operational Mach number.

Spectral analysis

The space-time correlation of the pressure fluctuation signal is shown analogous to the base flow results in Figure 6.33 for 500 reduced time steps. The instantaneous pressure fluctuation signals were extracted in the axial direction at the same positions of the line plots in the previous images. The pressure fluctuations were normalized using the dy-

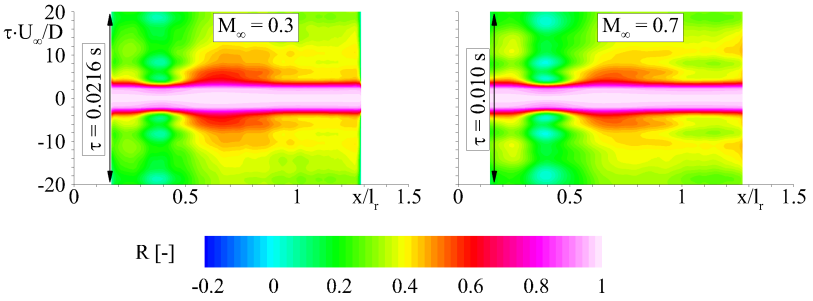

Fig. 6.34.: Contour map of the auto-correlation coefficient R for all wake pressure fluctuation signals along $\Phi = -200°$ at $M_\infty = 0.3$ (*left*) and $M_\infty = 0.7$ (*right*).

namic pressure q_∞. It was shown that the relative pressure fluctuation amplitudes are stronger at $M_\infty = 0.3$. The flow is dominated by large-scaled coherent events which appear intermittently. The large fluctuations seemed to extend over the entire near-wake. The dynamic range of the events seemed to reach from fairly low frequencies, as indicated by the strong coherent packages, up to large frequencies, as indicated by the smaller amplitudes.

The time-scales were analyzed in a similar manner as for the base-flow results by means of a signal auto-correlation. The time domain of the super-sampled pressure fluctuation signals (super-sampling factor: 5) were self-correlated at each axial wake position. The results are presented in Figure 6.34 for 40 reduced time steps. A slight peak-locking as a consequence of the chosen sampling rates was still noticeable in the plots. The absolute length of the signal cut-out was $\tau = [0.022; 0.010]$ s (lower at $M_\infty = 0.7$). The time scales in the wake vary with their axial position. It was shown that the time scales in the center of the vortex core at $x/l_r \approx 0.4$ correlate less compared to the reattachment position. It is assumed that weak short-duration pressure fluctuations are present in this area. Large-scale fluctuations should be too inert to follow the flow gradients into this domain. The largest coherent time scales appeared upstream of the reattachment position at the maximum of $c_{p,rms}$. It is assumed that the dominant wake buffeting somehow originates from the coherent structures in this area. The characteristic change of the time-scale pattern was already measured in the separation behind a fence at $Re = 7{,}900$ by Hudy et al. (2007).

The local buffet spectra along the wake's main axis was derived from the surface pressure fluctuations in a similar manner than it was already shown for the PIV investigations. The time domain of the pressure fluctuation signal was extracted at $\Phi = -200°$ and converted into the frequency domain by FFT. The results are presented in the Figures 6.35 and 6.36 for $M_\infty = 0.3$ and $M_\infty = 0.7$, respectively.

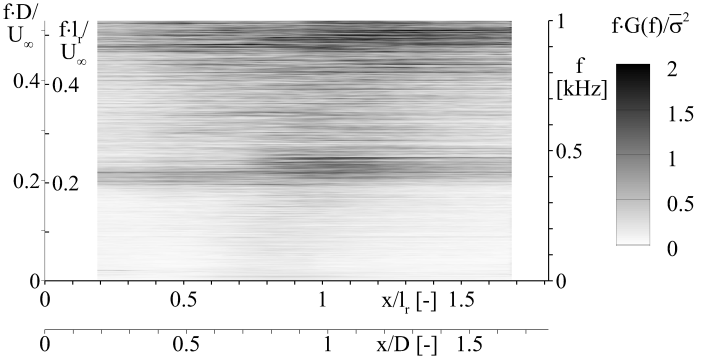

Fig. 6.35.: Local buffet spectrum of the pressure fluctuations with respect to the axial wake position at $M_\infty = 0.3$; dominant vortex shedding occurs around $f_{\text{shed}} \approx 0.4\,\text{kHz}$.

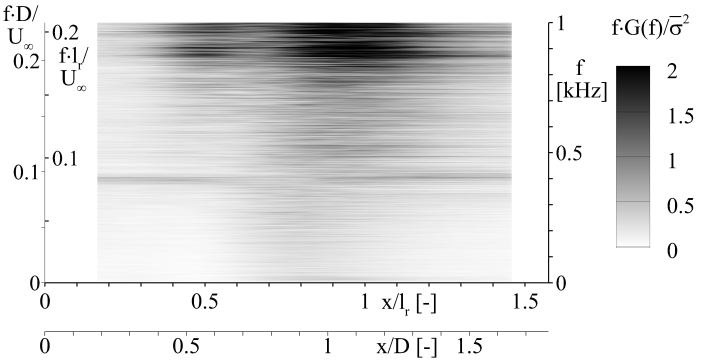

Fig. 6.36.: Local buffet spectrum of the pressure fluctuations with respect to the axial wake position at $M_\infty = 0.7$; dominant vortex shedding occurs around $f_{\text{shed}} \approx 0.9\,\text{kHz}$.

It is evident from both spectra that the wake is characterized by pressure fluctuations of a large dynamic range and not only by the dominant vortex shedding, as it was assumed from the PIV results. The dominant vortex shedding with expected reduced frequencies of $f \cdot U_\infty / D \approx 0.21$ was already confirmed by Deprés et al. (2004) and Deck et al. (2007) for their generic spacecraft configuration at $M_\infty = 0.85$. This dynamic behavior were also confirmed in these results from both plots. There are no sharp peaks but a

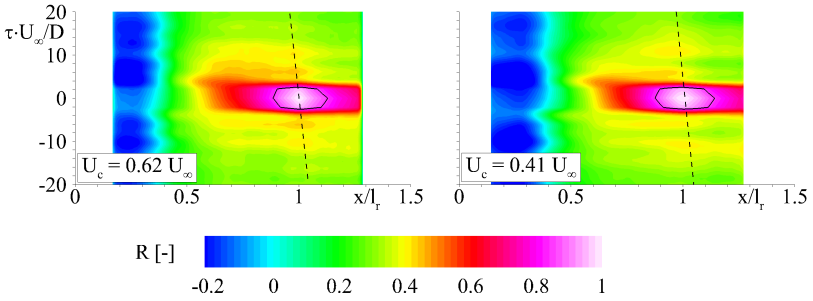

Fig. 6.37.: Contour map of the two-point cross-correlation between all wake pressure fluctuation signals along $\Phi = -200°$ and the reference signal at the reattachment position at $x/l_r = 1$ for $M_\infty = 0.3$ (*left*) and $M_\infty = 0.7$ (*right*); the pattern convection $f_c \cdot U_\infty/D$ is estimated from the inclination *dashed*); the segmentation threshold was 0.1 (*black*).

clear indication of events occurring with a reduced frequency around $f \cdot U_\infty/D \approx 0.21$. The total buffet energy of each frequency band is about 2 times higher compared to the results from Deprés et al. (2004) and Deck et al. (2007). The pressure fluctuation $c_{p,rms}$ was lower in the results presented here. Hence, the buffet spectra were reduced as a consequence of the notation from Owen (1958) in this case.
The dominant vortex shedding spreads out over the entire wake nearly independent from the axial position. A region of high dynamic range is located around the position of maximum $c_{p,rms}$ at $x/D \approx 0.9$ as already assumed from the previous auto-correlation plots. This domain of high dynamics originates from the large-scale shear layer structures which clash on the sting and decays into smaller structures. The vicinity of the vortex core at $x/D \approx 0.4$ is obviously dominated by weaker eddys as also assumed from the previous auto-correlation. The amplitudes of low-frequency events, which can be produced by larger flow scales, seemed reduced in this domain. This confirmed the assumption that large-scale structures are too inert and get broken up before they reach the vortex core. The 400 Hz wind tunnel perturbation in case of $M_\infty = 0.7$ was also resolved in the spectra.

Pattern propagation

The convection of disturbances was extensively studied for backward-facing step flows, compare e.g. Kiya and Sasaki (1985); Lee and Sung (2001) or Hudy et al. (2003). It was examined by nearly all authors that there exists no general law for potential dis-

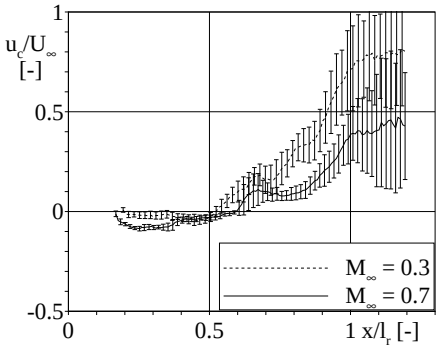

Fig. 6.38.: Evolution of the relative pattern propagation velocity u_c/U_∞ along the axial wake position; the propagation is separated in up- and downstream convection at $x/l_r = 0.55$.

turbance convection rates. Kiya and Sasaki (1985) examined that the flow in the recirculation area is dominated by the motion of large-scaled hair-pin-like vortices and low-frequency fluctuations. This motion separates into upstream and downstream convections at a certain position - not necessarily at $x/l_r = 1$. This "breathing" of the wake recirculation bubble is one of the dominant modes, as examined by Deprés et al. (2004). Hudy et al. (2003) or Deck et al. (2007) found up- and downstream propagating disturbances with characteristic convection velocities of $u_c/U_\infty = -0.26$ and $u_c/U_\infty = 0.6$, respectively. Both authors examined a separation position for up- and downstream propagation at $x/l_r = 0.5 - 0.7$.

The propagation of coherent pattern in the wake was studied by means of a two-point cross-correlation analysis, similar to the one that was presented for the base flow. The time domain of the space-time-correlation presented earlier in Figure 6.33 was cross-correlated with a reference signal at each wake position x/l_r. An exemplary cross-correlation between all axial pressure fluctuation signals and the reference signal at the position of the reattachment is presented in Fig. 6.37 for 40 reduced time steps. The length of the presented signal was $\tau = [0.022; 0.010]$ s (lower at $M_\infty = 0.7$). The pressure fluctuation signal was also super-sampled by a factor of 5 as for the previous investigations. The inclination of the correlation peak was extracted from the two-dimensional correlation plane while the reference signal was shifted between $x/l_r = 0.2 - 1.2$. This analysis was performed for various segmentation thresholds between 0.1 and 0.3. The results are presented in Figure 6.38 for $M_\infty = 0.3$ (*dashed*) and $M_\infty = 0.7$ (*solid*). The standard deviations represent the fluctuations that originated from the change of the segmentation threshold. The results confirmed that the propagation of disturbances is

separated into up- and downstream convections. The location for this separation was estimated to be $x/l_r \approx 0.5 - 0.6$. Prior to this position, coherent pattern convecting upstream in the direction of the base. The highest estimated upstream convection velocities were found with $u_c/U_\infty = [-0.03; -0.12]$ at $M_\infty = [0.3; 0.7]$. The maximum propagation velocity of downstream disturbances was found to be $u_c/U_\infty = [0.72; 0.48]$ at $x/l_r \approx 1.2$ for both test Mach numbers. Obviously, the convection of disturbances is faster at $M_\infty = 0.3$. The reason for this might be the presence of more small coherent pressure events in comparison with large-scaled structures, as indicated in the base flow topology for $M_\infty = 0.3$. These smaller events suffer from lower inertial effects and hence could reach higher convection rates. It is also evident from the results that the uncertainty in the estimated convection velocities is fairly high, especially downstream of the reattachment position. This is mainly caused by the high unsteadiness as a consequence of the reattaching shear layer. The "breathing" of the recirculation area additionally affects the results. Moreover, a higher sampling rate is recommended for prospective experiments in order to resolve the pattern convection more precisely.

Flow field topology: experiment vs. RANS

Finally, Figure 6.39 shows a comparison of the near-wake flow topologies as a result from the experimental and the numerical investigations presented in this thesis. The ensemble-averaged data of the PIV and iPSP measurements is shown color-coded in the case of the experimental results (*top*). The iPSP results were partly rotated for display purposes in this figure. The bottom plot represents the results of the 3D-RANS simulations. There was an offset of $\Delta c_p = 0.047$ between the numerical and the experimental results at the position of the base pressure sensor located at $r/R = 0.57$. This offset was subtracted from the entire numerical pressure coefficient map for display purposes. Hence, both the experimental and the numerical results correlate very well with each other in terms of their absolute values. The position of the wake vortex core and the mean reattachment length differ between $\Delta x/l_{c_{p,min}} \approx 0.26$ and $\Delta x/l_r \approx 0.07$, respectively. This discrepancy is mainly caused by a mismatch between the turbulence production term μ_t in the turbulence model and the turbulence level Tu in the experimental results.

One of the side goals of the project was the generation of a reliable experimental data base that can be used for the further development and validation of turbulence models for steady or unsteady simulations. The data gathered within the scope of this project exhibits a high spatial resolution which is suited for the validation of numerical methods. The comparison with established measurement techniques on the one side as well as the good agreement with data from the literature on the other side validated the quality of the experimental data set.

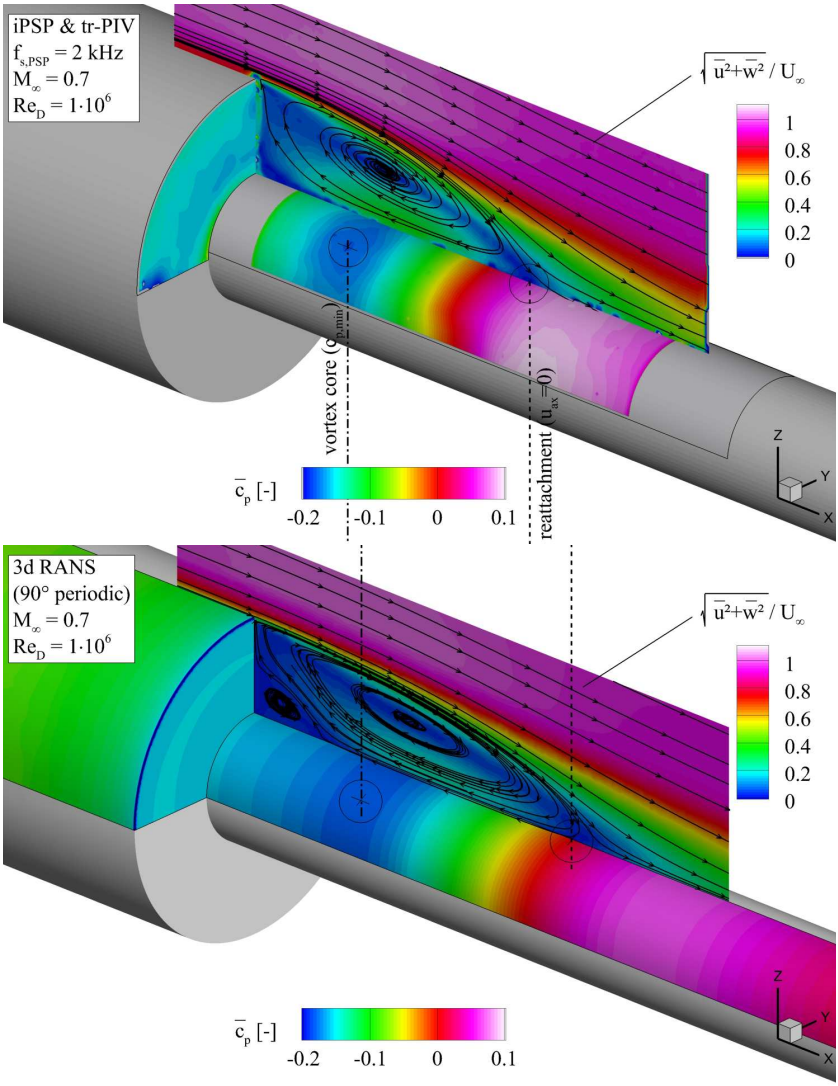

Fig. 6.39.: Flow field behind the generic spacecraft model; (*Top:*) experimental data gathered with time-resolved optical velocity and pressure measurement techniques; (*Bottom:*) results from a 3D-RANS simulation on a 90° portion of the model at $M_\infty = 0.7$ test conditions.

6.8. Conclusions and perspectives

The results of transient PIV and iPSP measurements in the near wake behind a generic spacecraft configuration were discussed within this chapter. The experiments were carried out in the trisonic wind tunnel facility at sub- and transonic Mach numbers $M_\infty = [0.3; 0.7]$. Regarding to the scientific key questions the following conclusions were drawn for the interesting test case of the project ($M_\infty = 0.7$):

1. *How is the topology of the wake?*
   The topology of the wake velocity field and the wake pressure distribution was investigated by means of PIV and iPSP. The ensemble-averaged flow fields at $M_\infty = 0.7$ developed as it was expected from numerical RANS simulations. It was found that the reattachment of the wake occurred at $x/D = 1.13$. The reattachment position was in good agreement with experimental and numerical data from Deprés et al. (2004) and Deck et al. (2007). The dominant recirculation area and the secondary counter-rotating vortex in the junction between the base and the support sting were clearly resolved with PIV.

2. *How is the dynamic and the strength of the coherent wake structures in the shear layer? Are these structures characterized by a certain frequency?*
   The results confirmed that the shear layer is dominated by large-scaled coherent structures combined with strong unsteady fluctuations. The dynamics of the large-scaled structure were confirmed by means of PIV and iPSP whereas the dynamic range of the unsteady fluctuations was just resolved with iPSP. The large structures separated from the base shoulder with reduced frequencies around $f \cdot U_\infty/D \approx 0.21$ and organized in a shear layer. The shear layer suddenly expanded at $x/D \approx 0.5$ as a consequence of a sudden change of the dominant time scales. The highest unsteadiness $c_{p,rms}$ occurred about 10-15 % upstream of the reattachment location. At this position, the strongest buffet loads were introduced into the structure (which was rigid at this part of the project). The actual dominant buffet frequency was about 905 Hz.
   The presented results confirmed the expected velocities for the propagation of disturbances along the wake's main axis, as proposed by Hudy et al. (2003) or Deck et al. (2007). A separation in up- and downstream propagating disturbances was found at $x/l_r = 0.6$. Their maximum relative convection velocities were $u_c/U_\infty = [-0.26; 0.45]$.

3. *Does the boundary layer/wake interaction result in a coherent mode pattern on the base?*
   It was confirmed by means of iPSP that there existed a certain mode-like distribution of base pressure fluctuations. The presence of pressure modes with a preferred 60°-distribution which was predicted by means of transient numerical

simulations was not confirmed. However, a mode-like distribution with spatial wavelengths of $\lambda_{p'} = 100 - 200^\circ$ was found at the base from the iPSP data.

4. *Is this mode pattern somehow time-dependent?*
   It was shown that the base flow was also dominated by the dominant vortex shedding frequency. The mode pattern propagated with reduced convection rates around $f_c \cdot U_\infty / D = 0.085 \pm 0.02$ (or about 350 Hz). An alternation of the propagation direction was not found.

Perspectives

The performance of the steady and the transient PSP system at UniBwM was benchmarked and the results were validated within the scope of this thesis. Prospective work has to be done in reducing the temperature dependence of pc-PSP in order to increase the measurement accuracy of iPSP. The performance of iPSP should be checked at higher frequencies in order to resolve potential higher harmonics of the dominant frequencies and in order to increase the accuracy of the two-point correlation analysis.
The flow quality of the trisonic wind tunnel is very good at transonic and supersonic conditions. It is suggested that the quality must be slightly improved at low subsonic conditions in order to reduce the amplification of perturbations as a consequence of the large turbulence level. The reduction of the dominant 400 Hz disturbance that originates from the hydraulic control system should be investigated.

7. Bibliography

ABE S, OKAMOTO K AND MADARAME H (2004). *The development of PIV-PSP hybrid system using pressure sensitive particles*. Meas. Sci. Technol., 15(6):1153.

ADRIAN R (1986). *Multi-point optical measurements of simultaneous vectors in unsteady flow - a review*. Int. J. Heat Fluid Fl., 7(2):127 – 145.

ARDASHEVA M, NEVSKY L AND PERVUSHIN G (1982). *Method of pressure distribution visualization with organic luminophores*. III the USSR School on the Methods of Aerophysical Investigations, Novosibirsk, UdSSR, 103–107 (in Russian).

ASAI K, AMAO Y, IIJIMA Y, OKURA I AND NISHIDE H (2002). *Novel pressure-sensitive paint for cryogenic and unsteady wind-tunnel testing*. J. Thermophys. Heat Transf., 16(1):109–115.

ASAI K, IIJIMA Y, KANDA H AND KUNIMATSU T (1998). *Novel pressure-sensitive coating based on anodic porous alumina*. 30th Fluid Dynamics Conference, Okayama, Japan.

ASAI K, KANDA H, CUNNINGHAM C, ERAUSQUIN R AND SULLIVAN J (1997). *Surface pressure measurement in a cryogenic wind tunnel by using luminescent coating*. 17th ICIASF, Monterey, Pacific Grove, CA, USA.

ASAI K, NAKAKITA K, KAMEDA M AND TEDUKA K (2001). *Recent topics in fast-responding pressure-sensitive paint technology at National Aerospace Laboratory*. 19th ICIASF, Cleveland, Ohio, USA.

ASHDOWN I (1994). *Radiosity: A Programmer's Perspective*. John Wiley & Sons, New York, NY.

AZAD P, GOCKEL T AND DILLMANN R (2009). *Computer Vision - Das Praxisbuch* 2. Elektor-Verlag, Aachen.

BARON A, DANIELSON J, GOUTERMAN M, WAN JR, CALLIS J AND MCLACHLAN B (1993). *Sub-millisecond response times of oxygen-quenched luminescent coatings*. Rev. Sci. Instrum., 64(12):3394–3402.

BELL J AND MCLACHLAN B (1996). *Image registration for pressure-sensitive paint applications*. Exp. Fluids, 22(1):78–86.

BELL J, SCHAIRER E, HAND L AND MEHTA R (2001). *Surface pressure measurements using luminescent coatings*. Ann. Rev. Fluid Mech., 33(1):155–206.

BITTER M, HARA T, HAIN R, YORITA D, ASAI K AND KÄHLER C (2012). *Characterization of pressure dynamics in an axisymmetric separating/ reattaching flow using fast-responding pressure-sensitive paint*. Exp. Fluids, 53(6):1737–1749.

BITTER M AND KÄHLER C (2011). *Optische Bestimmung von Oberflächendruck- & Temperaturverteilungen am NACA Profil im Unter- und Transschall*. 19. Lasermethoden in der Strömungsmesstechnik, Ilmenau, Germany.

BITTER M, KLEIN C AND KÄHLER C (2009). *PSP und µPSP Untersuchungen zur Freistrahl / Wand-Interaktion im Unter- und Überschall*. 17. Lasermethoden in der Strömungsmesstechnik, Erlangen, Germany.

BITTER M, SCHARNOWSKI S, HAIN R AND KÄHLER C (2011). *High-repetition-rate PIV investigations on a generic rocket model in sub- and supersonic flows*. Exp. Fluids, 50(4):1019–1030.

COHEN M, GREENBERG D, IMMEL D AND BROCK P (1986). *An efficient radiosity approach for realistic image synthesis*. IEEE Comput. Graph. Appl., 6(3):26–35.

COHEN M AND WALLACE J (1995). *Radiosity and realistic image synthesis* 2. Academic Press Professional, Boston, San Diego, New York.

DAVID C AND RADULOVIC S (2005). *Prediction of buffet loads on the Ariane 5 afterbody*. 6th International Symposium on Launcher Technologies, Munich, Germany.

DAVIS A, BEDWELL D, DUNLEAVY M AND BROWNOJOHN N (1995). *Pressure sensitive paint measurements using a phosphorescence lifetime method*. 7th International Symposium on Flow Visualization, Seattle, Washington, USA.

DECK S, THEPOT R AND THORIGNY P (2007). *Zonal detached eddy simulation of flow induced unsteady side-loads over launcher configurations*. 2nd EUCASS, Brussels, Belgium.

DEPRÉS D, DUSSAUGE J AND REIJASSE P (2004). *Analysis of unsteadiness in afterbody transonic flows*. AIAA J., 42(12):2541–2550.

DONOVAN J, MORRIS M, PAL A, BENNE M AND CRITES R (1993). *Data analysis techniques for pressure- and temperature-sensitive paint*. 31st AIAA Aerospace Sciences Meeting and Exhibit, AIAA 1993-176-380, Reno, Nevada, USA.

EATON JK (1980). *Turbulent flow reattachment: an experimental study of the flow and structure behind a backward-facing step.*, PhD thesis, Stanford University.

ENGLER R, HARTMANN K AND SCHULZE B (1991). *Aerodynamic assessment of an optical pressure measurement system OPMS by comparison with conventional pres-*

sure measurements in a high speed wind-tunnel. 14th ICIASF, Rockville, Maryland, USA.

ENGLER R, MÉRIENNE MC, KLEIN C AND LE SANT Y (2002). *Application of PSP in low speed flows*. Aerosp. Sci. Technol., 6(5):313–322.

ESA/CNES/ARIANESPACE (2013). URL `http://spaceinimages.esa.int`.

FLOTTMANN D, FORST D AND ROSSWAG H (2004). *Chemie für Ingenieure - Grundlagen und Praxisbeispiele* 2. Springer-Verlag Berlin, Heidelberg, New York.

FUJII S, NUMATA D, NAGAI H AND ASAI K (2013). *Development of ultrafast-response anodized-aluminum pressure-sensitive paints*. 51st AIAA Aerospace Sciences Meeting, AIAA 2013-0485, Grapevine, Texas, USA.

GONGORA-OROZCO N, ZARE-BEHTASH H AND KONTIS K (2009). *Effects of filters on the performance and characteristics of pressure-sensitive paints*. Meas. Sci. Technol., 20:077004.

GORAL C, TORRANCE K, GREENBERG D AND BATTAILE B (1984). *Modeling the interaction of light between diffuse surfaces*. SIGGRAPH Comput. Graph., 18(3):213–222.

GREGORY J, ASAI K, KAMEDA M, LIU T AND SULLIVAN J (2008). *A review of pressure-sensitive paint for high-speed and unsteady aerodynamics*. P. I. Mech. Eng. G - J. Aer., 222(2):249–290.

GREGORY J, SULLIVAN J, RAMAN G AND RAGHU S (2007). *Characterization of the microfluidic oscillator*. AIAA J., 45(3):568–576.

GÜLHAN A, (2008). *RESPACE - Key Technologies for Reusable Space Systems* 98. Springer-Verlag, Berlin, Heidelberg, New York.

HENCKELS A, GÜLHAN A AND NEEB D (2007). *An experimental study on the base flow/ plume interaction of booster configurations*. 1st CEAS European Air and Space Conference, Berlin, Germany.

HERRIN J AND DUTTON J (1994). *Supersonic base flow experiments in the near wake of a cylindrical afterbody*. AIAA J., 32(1):77–83.

HRADIL J, DAVIS C, MONGEY K, MCDONAGH C AND MACCRAITH B (2002). *Temperature-corrected pressure-sensitive paint measurements using a single camera and a dual-lifetime approach*. Meas. Sci. Technol., 13(10):1552.

HUDY L, NAGUIB A AND HUMPHREYS W (2003). *Wall-pressure-array measurements beneath a separating/reattaching flow region*. Phys. Fluids, 15(3):706–717.

HUDY L, NAGUIB A AND HUMPHREYS W (2007). *Stochastic estimation of a separated-flow field using wall-pressure-array measurements*. Phys. Fluids, 19(2):024103.

ISS INC (2013). URL `www.psp-tsp.com/index.php?id=117`.

KÄHLER C, SAMMLER B AND KOMPENHANS J (2002). *Generation and control of particle size distributions for optical velocity measurement techniques in fluid mechanics*. Exp. Fluids, 33(1):736–742.

KÄHLER C, SCHARNOWSKI S AND CIERPKA C (2012a). *On the resolution limit of digital particle image velocimetry*. Exp. Fluids, 52(6):1629–1639.

KÄHLER C, SCHARNOWSKI S AND CIERPKA C (2012b). *On the uncertainty of digital PIV and PTV near walls*. Exp. Fluids, 52(6):1641–1656.

KAMEDA M, TABEI T, NAKAKITA K, SAKAUE H AND ASAI K (2005). *Image measurements of unsteady pressure fluctuation by a pressure-sensitive coating on porous anodized aluminum*. Meas. Sci. Technol., 16(12):2517–2524.

KAUTSKY H AND HIRSCH A (1935). *Nachweis geringster Sauerstoffmengen durch Phosphoreszenztilgung*. Zeitschrift für anorganische und allgemeine Chemie, 222(2):126–134.

KAVANDI J, CALLIS J, GOUTERMAN M, KHALIL G, WRIGHT D, GREEN E, BURNS D AND MCLACHLAN B (1990). *Luminescent barometry in wind tunnels*. Rev. Sci. Instrum., 61(11):3340.

KEANE R AND ADRIAN R (1992). *Theory of cross-correlation analysis of PIV images*. Appl. Sci. Res., 49(3):191–215.

KHALIL G, COSTIN C, CRAFTON J, JONES G, GRENOBLE S, GOUTERMAN M, CALLIS J AND DALTON L (2004). *Dual-luminophor pressure-sensitive paint: I. ratio of reference to sensor giving a small temperature dependency*. Sensor. Actuat. B-Chem., 97(1):13–21.

KIYA M AND SASAKI K (1985). *Structure of large-scale vortices and unsteady reverse flow in the reattaching zone of a turbulent separation bubble*. J. Fluid Mech., 154:463–491.

KUZUB J, MEBARKI Y AND WHITEHEAD A (2011). *Improved pressure sensitive paint measurement using natural feature tracking and piecewise linear resection*. CRV '11, St. Johns, Newfoundland Canada, 48–55.

LE SANT Y (2001). *Overview of the self-illumination effect applied to pressure sensitive paint applications*. 19th ICIASF, Cleveland, Ohio, USA.

LE SANT Y, DELEGLISE B AND MEBARKI Y (1997). *An automatic image alignment method applied to pressure sensitive paint measurements*. 17th ICIASF, Monterey, CA, USA.

LE SANT Y, MERIENNE MC AND DURAND A (2005). *Image processing tools used for PSP and model deformation measurements*. 35th AIAA Fluid Dynamics Conference and Exhibit, AIAA 2005-5007, Toronto, Ontario, CA.

LEE I AND SUNG H (2001). *Characteristics of wall pressure fluctuations in separated flows over a backward-facing step: Part I. Time-mean statistics and cross-spectral analyses*. Exp. Fluids, 30(3):262–272.

LIU T, CATTAFESTA L, RADEZTSKY R AND BURNER A (2000). *Photogrammetry applied to wind tunnel testing*. AIAA J., 38(6):964–971.

LIU T AND SULLIVAN J (2005). *Pressure and Temperature Sensitive Paints* 1. Springer-Verlag, Berlin, Heidelberg, New York.

LÜDEKE H, CALVO J AND FILIMON A (2006). *Fluid structure interaction at the ariane-5 nozzle section by advanced turbulence models*. ECCOMAS CFD, Egmond aan Zee, The Netherlands.

MABEY D (1972). *Analysis and correlation of data on pressure fluctuations in separated flow*. AIAA J. Aircraft, 9(9):642–645.

MEINHART C, WERELEY S AND SANTIAGO J (2000). *A PIV Algorithm for Estimating Time-Averaged Velocity Fields*. J. Fluids Eng., 122(2):285–289.

MITSUO K, ASAI K, TAKAHASHI A AND MIZUSHIMA H (2006). *Advanced lifetime PSP imaging system for pressure and temperature field measurement*. Meas. Sci. Technol., 17(6):1282–1291.

MOON A, POLAND D AND SCHERAGA H (1965). *Thermodynamic data from fluorescence spectra. I. The system phenol-acetate*[1]. J. Phys. Chem., 69(9):2960–2966.

MOSHAROV V, RADCHENKO V AND FONOV S (1997). *Luminescent pressure sensors in aerodynamic experiments*. Books and technical publications. Central Aerohydrodynamic Institute - TsAGI, Zhukovsky.

MÉRIENNE MC, LE SANT Y, ANCELLE J AND SOULEVANT D (2004). *Unsteady pressure measurement instrumentation using anodized-aluminum PSP applied in a transonic wind tunnel*. Meas. Sci. Technol., 15(12):2349–2360.

OWEN T (1958). *Techniques of pressure-fluctuation measurements employed in the RAE low-speed wind-tunnels*, NATO.

PARKER C (1968). *Photoluminescence of Solutions* 1. Elsevier Publishing Co., Amsterdam, London, New York.

PERVUSHIN G AND NEVSKY L (1981). *Composition for indicating coating*. Patent: USSR SU 1065452 A.

PETERSON J AND FITZGERALD R (1980). *New technique of surface flow visualization based on oxygen quenching of fluorescence*. Rev. Sci. Instrum., 51(5):670 –671.

PFEFFER H (1996). *Towards reusable launchers - a widening perspective*, Tech. Report, European Space Agency (ESA).

PHONG B (1975). *Illumination for computer generated pictures*. Commun. ACM, 18(6):311–317.

RAFFEL M, WILLERT C, WERELEY S AND KOMPENHANS J (2007). *Particle image velocimetry: a practical guide*. Springer-Verlag, Berlin, Heidelberg, New York.

RAGNI D, SCHRIJER F, VAN OUDHEUSDEN B AND SCARANO F (2011). *Particle tracer response across shocks measured by PIV*. Exp. Fluids, 50(1):53–64.

RUYTEN W (1997). *Self-illumination calibration technique for luminescent paint measurements*. Rev. Sci. Instrum., 68(9):3452–3457.

RUYTEN W (2004). *Optimization of three-gated lifetime pressure and temperature-sensitive paint measurements*. 24th AIAA Aerodynamic Measurements Technology and Ground Testing Conference, AIAA 2004-2190, Portland, Oregon, USA.

SAKAUE H, TABEI T AND KAMEDA M (2006). *Hydrophobic monolayer coating on anodized aluminum pressure-sensitive paint*. Sensor. Actuat. B-Chem., 119(2):504–511.

SCHARNOWSKI S, HAIN R AND KÄHLER C (2012). *Reynolds stress estimation up to single-pixel resolution using PIV-measurements*. Exp. Fluids, 52(4):985–1002.

SCHARNOWSKI S AND KÄHLER C (2011). *Investigation of the wake dynamics of a generic space launcher at Ma = 0.7 by using high-repetition rate PIV*. 4th EUCASS, Saint Petersburg, Russia.

SCHRIJER F, SCIACCHITANO A, SCARANO F, HANNEMANN K, PALLEGOIX JF, MASELAND J AND SCHWANE R (2011). *Experimental investigation of base flow buffeting on the ariane 5 launcher using high speed PIV*. 7th European Symposium on Aerothermodynamics for Space Vehicles, Brugge, Belgium.

SCROGGIN A, SLAMOVICH E, CRAFTON J, LACHENDRO N AND SULLIVAN J (1999). *Porous polymer / ceramic composites for luminescence-based temperature and pressure measurement*. Materials Research Society Symposium, San Francisco, CA, USA.

SFB/TR 40 (2013). URL `www.sfbtr40.de`.

SHANMUGASUNDARAM R AND SAMAREH-ABOLHASSANI J (1995). *Modified scatter data interpolation used to correct pressure sensitive paint images*. 30th AIAA Thermophysics Conference, AIAA-95-2041, San Diego, CA, USA.

SINGH M, NAUGHTON J, YAMASHITA T, NAGAI H AND ASAI K (2011). *Surface pressure and flow field behind an oscillating fence submerged in turbulent boundary layer*. Exp. Fluids, 50(3):701–714.

SMITH S AND BRADY J (1997). *SUSAN- a new approach to low level image processing*. Int. J. Comput. Vision, 23(1):45–78.

STATNIKOV V, GLATZER C, MEISS JH, MEINKE M AND SCHRÖDER W (2012). REIJASSE P, KNIGHT D, IVANOV M AND LIPATOV I, eds. *Progress in flight physics* 5 Numerical Investigation of the Near Wake of Generic Space Launcher Systems at Transonic and Supersonic Flows.

STERN O AND VOLMER M (1919). *Über die Abklingungszeit der Fluoreszenz*. Phys. Z., 20:183–188.

STICH M AND WOLFBEIS O (2008). *Standardization and Quality Assurance in Fluorescence Measurements* 5 Fluorescence Sensing and Imaging Using Pressure-Sensitive Paints and Temperature-Sensitive Paints, 429–461. Springer-Verlag Berlin, Heidelberg, New York.

SUGIMOTO T, KITASHIMA S, NUMATA D, NAGAI H AND ASAI K (2012). *Characterization of frequency response of pressure-sensitive paints*. 50th AIAA Aerospace Sciences Meeting, AIAA 2012-1185, Nashville, Tennessee, USA.

SUNG H, PARK SH AND KIM M (2005). *Accuracy of correlation-based image registration for pressure-sensitive paint*. Exp. Fluids, 39(3):630–635.

TSAI R (1986). *An efficient and accurate camera calibration technique for 3d machine vision*. Conference on Computer Vision and Pattern Recognition, Miami Beach, FL, USA.

VAN OUDHEUSDEN B AND SCARANO F (2008). SCHRÖDER A AND WILLERT C, eds. *Topics in Applied Physics* PIV Investigation of Supersonic Base-Flow-Plume Interaction, 465–474. Springer-Verlag, Berlin, Heidelberg, New York.

VENKATAKRISHNAN L (2004). *Comparative study of different pressure-sensitive-paint image registration techniques*. AIAA J., 42(11):2311–2319.

WEISS PE, DECK S, ROBINET JC AND SAGAUT P (2009). *On the dynamics of axisymmetric turbulent separating/reattaching flows*. Phys. Fluids, 21(7):075103.

WELCH P (1967). *The use of fast fourier transform for the estimation of power spectra: A method based on time averaging over short, modified periodograms*. IEEE Trans. Audio Electroacoustics, 15(2):70–73.

WOODMANSEE M AND DUTTON J (1998). *Treating temperature-sensitivity effects of pressure-sensitive paint measurements*. Exp. Fluids, 24(2):163–174.

8. List of symbols

index	meaning
∞	conditions at infinity
clean	clean reference surface
cont.	contaminated surface
ref,0	reference conditions
won	wind-on conditions
wof	wind-off conditions

greek symbol	meaning [unit]
α	angle of attack [°]
γ	contact angle [°]
Φ	polar angle [°]
τ	retarded time [s]
τ_f	fluorescence life time [s]
τ_{diff}	diffusion time [s]
λ	wavelength (with respect to light) [nm]
λ_s	spatial wavelength [°]

abbreviation	meaning
BRDF	bidirectional reflectance distribution function
CCD	charge-coupled device
CFD	computational fluid dynamic

continued

abbreviation	meaning
CFL	Courant-Friedrichs-Lewy number
CMOS	complementary metal oxide semiconductor
DLR	German aerospace lab (Deutsches Zentrum für Luft- und Raumfahrt e.V.)
iPSP	instationary/ fast-responding pressure-sensitive paint (the measurement technique)
IRES	Intensity Reduction & Evaluation Software
JAXA	Japan Aerospace Exploration Agency
LED	light-emitting diode
LES	large eddy simulation
LSB	laminar separation bubble
NACA	National Advisory Committee for Aeronautics
NASA	American aerospace agency (National Aeronautics and Space Administration)
ONERA	French aerospace lab (Office National d'Etudes et Recherches Aérospatiales)
pc-PSP	pressure-sensitive coating on a polymer/ceramic base layer
PDF	probability-density function
PIV	particle-image velocimetry
PSP	pressure-sensitive paint
PtTFPP	platinum-tetrakis(pentafluorophenyl)porphyrin
RANS	Reynolds-Averaged Navier-Stokes
ROI	region of interest
RTD	resistant thermoelectric device
RMS	root-mean-square
SI	self-illumination
SNR	signal-to-noise ratio
tr-PIV	time-resolved particle-image velocimetry

continued

abbreviation	meaning
TRR40	joint research project of the German research foundation (Sonderforschungsbereich TransRegio 40 der Deutschen Forschungsgemeinschaft)
TsAGI	Russian Central Aerohydrodynamic Institute
TWM	trisonic wind tunnel Munich
UniBwM	Department of Fluid Mechanics and Aerodynamics at the Bundeswehr University Munich
uv	ultra-violet (with respect to wavelengths)

latin symbol	meaning [unit]
A, B, C	paint calibration coefficients [1]
c	chord length [a.u.]
c_p	pressure coefficient [1]
$c_\mathrm{p,rms}$	pressure fluctuation coefficient [1]
$\Delta c_\mathrm{p,rms}$	absolute PSP measurement uncertainty [1]
c_r	reflectance coefficient [1]
d_poly	PSP layer thickness [μm]
d, D	diameter [a.u.]
e_i	specific uncertainty portion [%]
E_est	expected relative iPSP measurement uncertainty [%]
E_real	effective relative iPSP measurement uncertainty [%]
f	frequency [Hz]
f_c	cut-off frequency [Hz]
f_s	sampling frequency [Hz]
F	focal length [mm]
H_{12}	boundary layer shape factor [1]
I	intensity [cts]
$I_0/I, I_\mathrm{ref}/I$	Stern-Volmer intensity ratio [1]

continued

latin symbol	meaning [unit]
k	turbulent kinetic energy [m^2/s^2]
l_r	reattachment length [a.u.]
M	optical magnification [1]
M_∞	free stream Mach number [1]
n, N	number of specific samples [1]
OD	optical density [1]
p	pressure [Pa]
p'	pressure fluctuation [Pa]
q_∞	free-stream dynamic pressure [Pa]
r, R	radius [a.u.]
Re_c	Reynolds number w.r.t characteristic length c [1]
St_D	reduced frequency $f \cdot U_\infty / D$, Strouhal number [1]
t	time [s]
Δt	pulse delay [s]
t_p	pulse duration [s]
T	temperature [°C]
Tu	wind tunnel turbulence level [%]
$\mathbf{U}$	velocity vector with components u; v; w [m/s]

A. Self-illumination validation

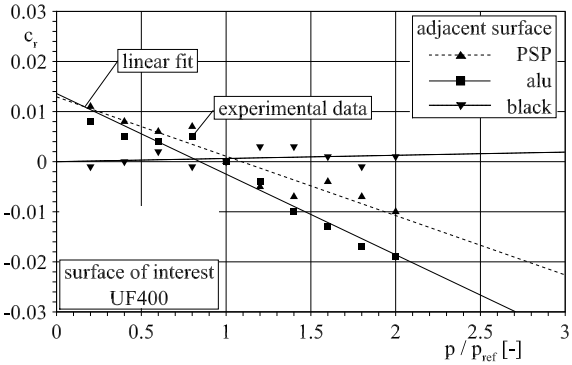

Fig. A.1.: Pressure dependency of the absorption coefficient c_r for the three adjacent configurations (*symbols*) of the UF400-coated base plate; linear fit lines of the empirical absorption coefficients are included.

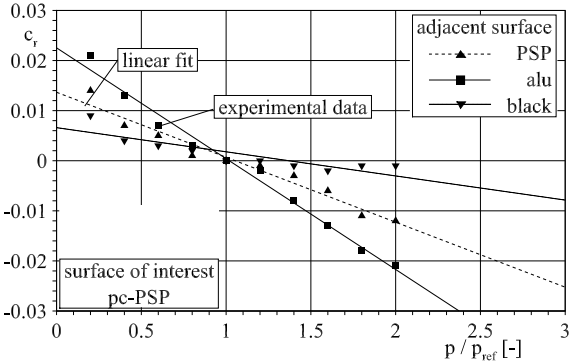

Fig. A.2.: Pressure dependency of the absorption coefficient c_r for the three adjacent configurations (*symbols*) of the pc-PSP-coated base plate; linear fit lines of the empirical absorption coefficients are included.

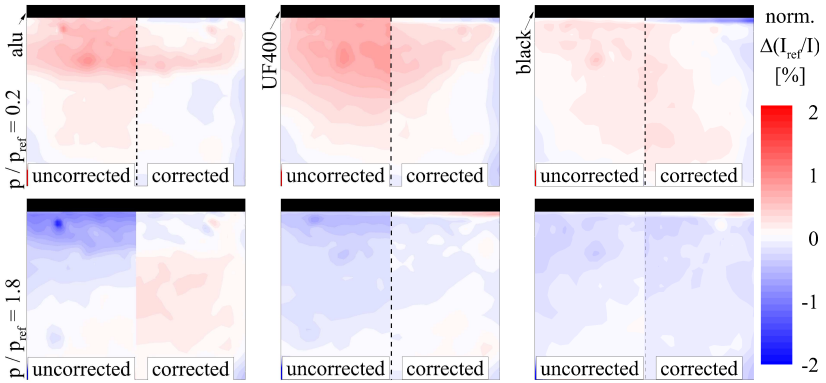

Fig. A.3.: Comparison of the intensity change in the vicinity of a rectangular corner due to self-illumination; *Left sample half:* measured self-illumination effect; *Right sample half:* radiosity-corrected SI-effect; *Adjacent surfaces* (from left to right): frosted aluminum, UF400, absorber paint; pressure ratios: $p/p_{\mathrm{ref}} = 1-80\,\%$ (*top*) and $p/p_{\mathrm{ref}} = 1+80\,\%$ (*bottom*).

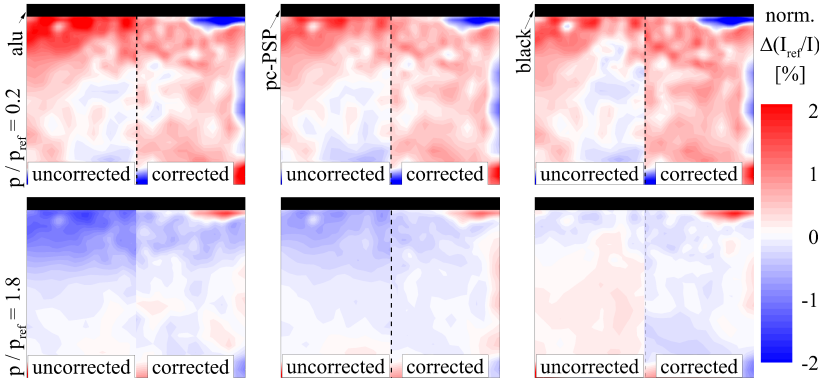

Fig. A.4.: Comparison of the intensity change in the vicinity of a rectangular corner due to self-illumination; *Left sample half:* measured self-illumination effect; *Right sample half:* radiosity-corrected SI-effect; *Adjacent surfaces* (from left to right): frosted aluminum, pc-PSP, absorber paint; pressure ratios: $p/p_{\mathrm{ref}} = 1-80\,\%$ (*top*) and $p/p_{\mathrm{ref}} = 1+80\,\%$ (*bottom*).

B. IRES

Folder structure and input files

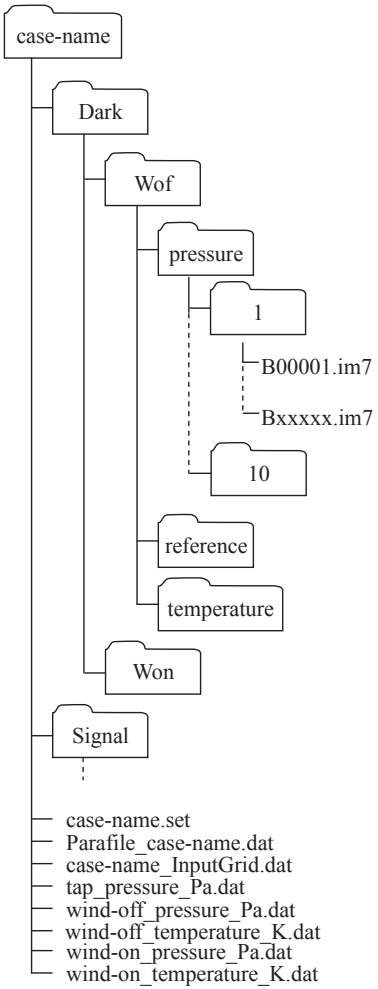

Fig. B.1.: Mandatory folder and file structure for a successful data evaluation with *IRES*.

The parameter file

********** global: case name **********
case-name
–> *the name of the recent case*
********** global: data path **********
E:/case-name/
–> *the global data path for the case name (just for orientation; won't be used in IRES)*
********** calibration: name **********
PCPSP_Phantom_2kHz_21-May-2012
–> *the a-priori calibration out of a calibration chamber from the paint that was used during the experiments*
********** calibration: normalization temperature [°C] **********
25.000000
–> *the reference temperature for the normalization of the Stern-Volmer plot during the calibration*
********** calibration: normalization pressure [mbar] **********
1000.000000
–> *the reference pressure for the normalization of the Stern-Volmer plot during the calibration*
********** calibration paint: [PSP] or [TSP] **********
PSP
–> *which paint was used: defines the law/coefficients that will be used for the evaluation of the intensity ratio*
********** calibration: paint type [uni] or [binary] **********
uni
–> *type of paint: defines, which sub-routines for image extraction and ratio creation are active*
********** calibration: paint response [steady] or [unsteady] **********
unsteady
–> *historical parameter from previous IRES versions: no use in latest version 3.1*

********** correction: pressure in-situ-flag [on] or [off] **********
off
–> flag de-/activates the in-situ pressure correction of the raw pressure values by means of the "tap_pressures_Pa.dat"-file
********** correction: temperature [Tsensor] or [IR] or [TSP] or [CFD] **********
Tsensor
–> defines, which temperature correction method is applied (so far ONLY Tsensor is validated in IRES V3.1)
********** evaluation: DLT method [poly] or [linear] or [advanced] **********
advanced
–> defines, which camera calibration algorithm is used; poly (not yet implemented) for planar problems; linear - DLT-algorithm with no lens distortion corrections for NON-PLANAR problems needs 6 or more registration markers; advanced - advanced polynomial approach with lens distortion correction for NON-PLANAR problems needs 8 or more registration markers
********** evaluation: final resection [2d] or [3d] or [both] **********
3d
–> defines the output format of calculation result: 2d - image format, 3d - tecplot format on grid
********** filter: intensity images [susan] or [median] or [wiener] or [off] **********
off
–> defines the initial filtering of the intensity images by using the SUSAN filter (for details about this filter algorithm see Smith and Brady (1997)), a standard median or a wiener filter
********** filter: intensity images filter size median/wiener:[size size] or susan: [size threshold] **********
0.000000 0.000000
–> for the median and the wiener filter the flag defines the spatial filter size in two dimensions. For the SUSAN filter it defines the filter size and the local intensity weighting factor for filtering
********** filter: intensity ratio [susan] or [median] or [wiener] or [off] **********
susan
–> see intensity image filter

********** filter: intensity ratio filter size median/wiener:[size size] or susan: [size threshold] **********
2.000000 2.000000
–> see intensity image filter size
********** filter: final [susan] or [median] or [wiener] or [off] **********
susan
–> see intensity image filter
********** filter: final filter size median/wiener:[size size] or susan: [size threshold] **********
5.000000 0.08
–> see intensity image filter size
********** grid: final mesh type for export [coarse] or [fine] **********
coarse
–> historical parameter from previous IRES versions: no use in latest version 3.1
********** grid: grid rotation [on] or [off] **********
no
–> activates grid rotation for display purposes in the 3d tecplot grid file; if activated the angles alpha, and/or beta and/or gamma (see below) must be set
********** grid: input grid type: triangle [tri] or quadrilateral [quad] **********
quad
–> required for correct data import, export and filtering - HOMOGEN surface discretization ONLY
********** image: acquisition frequency [Hz] **********
2000.000000
******** image: camera type: pco2000 [1] or pco4000 [2] or sensicam [3] or Phantom [4] or Dalsa Genie [5] or other [6] ***
4
–> the pixel size of the sensor might vary with the camera model; the value will be used for the estimation of the camera position in the camera calibration algorithm
********** image: dynamic [min max] **********
10 2000
–> global preset of the min/max intensities in the images for all input GUIs - no EXACT values required

********** image: frame order [0 1] [1 0] - pressure monitor == 0 ** reference monitor == 1**********
0 0
–> historical parameter from previous IRES versions: no use in latest version 3.1
********** image: integration time [ms] **********
0.499000
–> historical parameter from previous IRES versions: no use in latest version 3.1
********** image: number of dark wind-off images **********
500
–> number of dark wind-off images
********** image: number of dark wind-on images **********
500
–> number of dark wind-on images
********** image: number of signal wind-off images **********
1000
–> number of signal wind-off images
********** image: number of signal wind-on images **********
10240
–> number of signal wind-on images
********** image: zero padding :BXXXXX.IM7 [sum(X)] **********
5
–> defines the number of the digits in the filename; filename has to start with "B"
********** windtunnel: angle of attack alpha [°] **********
0.000000
–> see grid rotation above
********** windtunnel: angle of sideslip beta [°] **********
0.000000
–> see grid rotation above

********** windtunnel: angle of roll gamma [°] **********
0.000000
–> *see grid rotation above*
********** windtunnel: dynamic pressure [Pa] **********
10752
–> *dynamic pressure (Pa) during the experiments, usually constant*
********** windtunnel: mach number **********
0.31
–> *wind tunnel Mach number, usually constant*
********** windtunnel: velocity [m/s] **********
104.9065
–> *wind tunnel velocity (m/s), usually constant*

Photogrammetry relations

The photogrammetry relations describe the conversion of the transformation coefficients L into intrinsic (Equ. B.0.1) and extrinsic camera parameter (Equ. B.0.2), compare Azad et al. (2009). Intrinsic camera parameter such as the focal length, the principle point or lens distortions describe parameter which are directly linked to the imaging optics. The extrinsic parameter describe the absolute position and orientation of the camera. The parameter are subsequently used in pseudo-code algorithms in order to clarify the image alignment in *IRES*.

$$
\begin{aligned}
L &:= \sqrt{L_9^2 + L_{10}^2 + L_{11}^2} \\
c_x &= \frac{L_1 L_9 + L_2 L_{10} + L_3 L_{11}}{L^2} \\
c_y &= \frac{L_5 L_9 + L_6 L_{10} + L_7 L_{11}}{L^2} \\
f_x &= \sqrt{\frac{L_1^2 + L_2^2 + L_3^2}{L^2} - c_x^2} \\
f_y &= \sqrt{\frac{L_5^2 + L_6^2 + L_7^2}{L^2} - c_y^2}
\end{aligned}
\tag{B.0.1}
$$

$$
r_{31} = \frac{L_9}{L};\ r_{32} = \frac{L_{10}}{L};\ r_{33} = \frac{L_{11}}{L}
$$

$$
r_{11} = \frac{\frac{L_1}{L} - c_x r_{31}}{f_x};\ r_{12} = \frac{\frac{L_2}{L} - c_x r_{32}}{f_x};\ r_{13} = \frac{\frac{L_3}{L} - c_x r_{33}}{f_x}
$$

$$
r_{21} = \frac{\frac{L_5}{L} - c_y r_{31}}{f_y};\ r_{22} = \frac{\frac{L_6}{L} - c_y r_{32}}{f_y};\ r_{23} = \frac{\frac{L_7}{L} - c_y r_{33}}{f_y}
$$

$$
\begin{aligned}
R_c &= \begin{pmatrix} r_{11} & r_{12} & r_{13} \\ r_{21} & r_{22} & r_{23} \\ r_{31} & r_{32} & r_{33} \end{pmatrix} \\
\mathbf{t} &= R_c \begin{pmatrix} L_1 & L_2 & L_3 \\ L_5 & L_6 & L_7 \\ L_9 & L_{10} & L_{11} \end{pmatrix}^{-1} \begin{pmatrix} L_4 \\ L_8 \\ 1 \end{pmatrix}
\end{aligned}
\tag{B.0.2}
$$

Equ. B.0.3 describes the iterative calculation of the dewarped image $I(u,v)$ by means of the lens distortions κ and the distorted image $I(u_\mathrm{d},v_\mathrm{d})$. The relations are essential in order to project images from one optical system into another.

$$\begin{pmatrix} (u_1-c_\mathrm{x})\,r_1^2 & (u_1-c_\mathrm{x})\,r_1^4 & 2x_{\mathrm{n},1}y_{\mathrm{n},1}\,f_\mathrm{x} & \left(r_1^2+2x_{\mathrm{n},1}^2\right)f_\mathrm{x} \\ (v_1-c_\mathrm{y})\,r_1^2 & (v_1-c_\mathrm{y})\,r_1^4 & \left(r_1^2+2y_{\mathrm{n},1}^2\right)f_\mathrm{y} & 2x_{\mathrm{n},1}y_{\mathrm{n},1}\,f_\mathrm{y} \\ \vdots & \vdots & \vdots & \vdots \\ (u_n-c_\mathrm{x})\,r_n^2 & (u_n-c_\mathrm{x})\,r_n^4 & 2x_{\mathrm{n,n}}y_{\mathrm{n,n}}\,f_\mathrm{x} & \left(r_n^2+2x_{\mathrm{n,n}}^2\right)f_\mathrm{x} \\ (v_n-c_\mathrm{y})\,r_n^2 & (v_n-c_\mathrm{y})\,r_n^4 & \left(r_n^2+2y_{\mathrm{n,n}}^2\right)f_\mathrm{y} & 2x_{\mathrm{n,n}}y_{\mathrm{n,n}}\,f_\mathrm{y} \end{pmatrix} \begin{pmatrix} \kappa_1 \\ \kappa_2 \\ \kappa_3 \\ \kappa_4 \end{pmatrix} =$$

$$= \begin{pmatrix} u_{\mathrm{d},1}-u_1 \\ v_{\mathrm{d},1}-v_1 \\ \vdots \\ u_{\mathrm{d,n}}-u_\mathrm{n} \\ v_{\mathrm{d,n}}-v_\mathrm{n} \end{pmatrix} \quad \text{(B.0.3)}$$

Pseudo codes for the image alignment and the camera calibration

The pseudo codes were adapted from Azad et al. (2009). They appear in the order of their implementation in *IRES*. Algorithm 1 describes the camera calibration by means of the marker correspondences. The intensity images can be affected by optical aberrations or lens distortions. In order to compensate these distortions, Alg. 2 is required. Alg. 3 shows the creation of the real world coordinates for the working grid from the red_{wof} reference points. The remaining algorithms 4 and 5 are used for the invert the previous algorithms.

Algorithm 1: CalibrateCameraParameter: marker positions $P(x,y,z)$, $P(u_\text{d},v_\text{d}) \rightarrow$ intrinsic / extrinsic camera calibration

Data: marker positions in the real-world coordinate system: $P(x,y,z)$ and in the image plane $P'(u_\text{d},v_\text{d})$

Result: camera calibration parameter (c_x, c_y, f_x, f_y, R_c, $\mathbf{t}$, d_1, d_2, d_3, d_4)

1 initialize lens distortions: $d_1 = d_2 = d_3 = d_4 := 0$

2 **while** $k > thresh$ **do**

3 dewarp $P'(u_\text{d},v_\text{d}) \rightarrow P'(u,v)$ using Algorithm 2

4 solve Equ. 4.2.1 for coefficients $L_1 \ldots L_{11}$ using $n \geq 6$ markers

5 calculate intrinsic camera parameter c_x,c_y,f_x,f_y with Equ. B.0.1

6 calculate extrinsic camera parameter R_c, $\mathbf{t}$ with Equ. B.0.2

7 $$\begin{pmatrix} u \cdot s_\text{c} \\ v \cdot s_\text{c} \\ s_\text{c} \end{pmatrix} := \underbrace{\begin{pmatrix} f_\text{x} & 0 & c_\text{x} \\ 0 & f_\text{y} & c_\text{y} \\ 0 & 0 & 1 \end{pmatrix}}_{\text{calibration matrix}} (R_\text{c} \,|\, \mathbf{t})$$

8 calculate lens distortions $d_1 \ldots d_4$ with u, v and u_d, v_d from Equ. B.0.3

9 **end**

Algorithm 2: DewarpImage: $P'(u_\mathrm{d},v_\mathrm{d}) \rightarrow P'(u,v)$

Data: distorted points in the camera system $P'(u_\mathrm{d},v_\mathrm{d})$
Result: undistorted points in the camera system $P'(u,v)$

foreach u, v **do**

$$\begin{pmatrix} x_\mathrm{d} \\ y_\mathrm{d} \end{pmatrix} := \begin{pmatrix} \frac{u_\mathrm{d}-c_\mathrm{x}}{f_\mathrm{x}} \\ \frac{v_\mathrm{d}-c_\mathrm{y}}{f_\mathrm{y}} \end{pmatrix}$$

$$\begin{pmatrix} x_\mathrm{n} \\ y_\mathrm{n} \end{pmatrix} := \begin{pmatrix} x_\mathrm{d} \\ y_\mathrm{d} \end{pmatrix}$$

$$r := \sqrt{x_\mathrm{n}^2+y_\mathrm{n}^2}$$

while $k > thresh$ **do**

$$\begin{pmatrix} x'_\mathrm{n} \\ y'_\mathrm{n} \end{pmatrix} := \frac{1}{1+d_1r^2+d_2r^4}\left[\begin{pmatrix} x_\mathrm{d} \\ y_\mathrm{d} \end{pmatrix} - \begin{pmatrix} d_3(2x_\mathrm{n}y_\mathrm{n})+d_4(r^2+2x_\mathrm{n}^2) \\ d_3(r^2+2y_\mathrm{n}^2)+d_4(2x_\mathrm{n}y_\mathrm{n}) \end{pmatrix}\right]$$

$$\begin{pmatrix} x_\mathrm{n} \\ y_\mathrm{n} \end{pmatrix} := \begin{pmatrix} x'_\mathrm{n} \\ y'_\mathrm{n} \end{pmatrix}$$

$$r := \sqrt{x_\mathrm{n}^2+y_\mathrm{n}^2}$$

end

$$\begin{pmatrix} u \\ v \end{pmatrix} := \begin{pmatrix} f_\mathrm{x}x'_\mathrm{n}+c_\mathrm{x} \\ f_\mathrm{y}y'_\mathrm{n}+c_\mathrm{y} \end{pmatrix}$$

Algorithm 3: ComputeRealWorldCoordinatesFromCamera: $P'(u_\mathrm{d},v_\mathrm{d},s_\mathrm{c}) \rightarrow P(x,y,z)$

Data: Points P' in the distorted red$_\mathrm{wof}$ $P'(u_\mathrm{d},v_\mathrm{d},s)$
Result: Points in real world coordinates $P(x,y,z)$

foreach P' **do**

dewarp $P'(u_\mathrm{d},v_\mathrm{d}) \rightarrow P'(u,v)$ using Algorithm 2

$$\begin{pmatrix} x_\mathrm{c} \\ y_\mathrm{c} \\ z_\mathrm{c} \end{pmatrix} := s_\mathrm{c}\begin{pmatrix} \frac{u-c_\mathrm{x}}{f_\mathrm{x}} \\ \frac{v-c_\mathrm{y}}{f_\mathrm{y}} \\ 1 \end{pmatrix}$$

$$\begin{pmatrix} x \\ y \\ z \end{pmatrix} := R_\mathrm{c}^T\begin{pmatrix} x_\mathrm{c} \\ y_\mathrm{c} \\ z_\mathrm{c} \end{pmatrix} - R_\mathrm{c}^T \cdot \mathbf{t}$$

Algorithm 4: ComputeCameraCoordinatesFromRealWorld: $P(x,y,z) \rightarrow P'(u_\mathrm{d},v_\mathrm{d})$

Data: Points P in real world coordinates $P(x,y,z)$
Result: Distorted points in the camera coordinate system $P'(u_\mathrm{d},v_\mathrm{d})$

1 **foreach** P **do**

2 $\begin{pmatrix} x_\mathrm{c} \\ y_\mathrm{c} \\ z_\mathrm{c} \end{pmatrix} := R_\mathrm{c} \begin{pmatrix} x_\mathrm{c} \\ y_\mathrm{c} \\ z_\mathrm{c} \end{pmatrix} + \mathbf{t}$

3 $\begin{pmatrix} u \\ v \end{pmatrix} := \begin{pmatrix} c_\mathrm{x} \\ c_\mathrm{y} \end{pmatrix} + \frac{1}{z_\mathrm{c}} \begin{pmatrix} f_\mathrm{x} x_\mathrm{c} \\ f_\mathrm{y} y_\mathrm{c} \end{pmatrix}$

4 distort $P'(u,v) \rightarrow P'(u_\mathrm{d},v_\mathrm{d})$ using Algorithm 5

Algorithm 5: DistortImage: $P'(u,v) \rightarrow P'(u_\mathrm{d},v_\mathrm{d})$

Data: undistorted points in the camera system $P(u,v)$
Result: distorted points in the camera system $P'(u_\mathrm{d},v_\mathrm{d})$

1 **foreach** P' **do**

2 $\begin{pmatrix} x_\mathrm{n} \\ y_\mathrm{n} \end{pmatrix} := \begin{pmatrix} \frac{u-c_\mathrm{x}}{f_\mathrm{x}} \\ \frac{v-c_\mathrm{y}}{f_\mathrm{y}} \end{pmatrix}$

3 $r := \sqrt{x_\mathrm{n}^2 + y_\mathrm{n}^2}$

4 $\begin{pmatrix} x_\mathrm{d} \\ y_\mathrm{d} \end{pmatrix} := \left(1 + d_1 r^2 + d_2 r^4\right) \begin{pmatrix} x_\mathrm{n} \\ y_\mathrm{n} \end{pmatrix} + \begin{pmatrix} d_3(2x_\mathrm{n}y_\mathrm{n}) + d_4(r^2 + 2x_\mathrm{n}^2) \\ d_3(r^2 + 2y_\mathrm{n}^2) + d_4(2x_\mathrm{n}y_\mathrm{n}) \end{pmatrix}$

5 $\begin{pmatrix} u_\mathrm{d} \\ v_\mathrm{d} \end{pmatrix} := \begin{pmatrix} f_\mathrm{x} x_\mathrm{d} + c_\mathrm{x} \\ f_\mathrm{y} y_\mathrm{d} + c_\mathrm{y} \end{pmatrix}$